Accelerated Monte Carlo based Quantitative SPECT Reconstruction

By
Shaoying Liu, M.Sc, B.Sc

A Thesis
Submitted to the School of Graduate Studies
in Partial Fulfillment of the Requirements
for the Degree
Doctor of Philosophy

McMaster University

December 16, 2009

DOCTOR OF PHILOSOPHY (2009)
Electrical and Computer Engineering
McMaster University
Hamilton, Ontario

TITLE: Accelerated Monte Carlo based Quantitative SPECT Reconstruction
AUTHOR: Shaoying Liu, M.Sc (Tsinghua University), B.Sc (Fuzhou University)
SUPERVISOR: Dr. Troy H. Farncombe
NUMBER OF PAGES: xi,214

Acknowledgement

This thesis would not have been accomplished without the funds provided by numerous organizations. I would like to acknowledge the financial support provided by National Institutes of Health. Another source of funding I have received is from the Ontario Institute of Cancer Research under the 1 mm Challenge. I thank both of them for the financial assistance for this thesis research. I am also grateful to the research groups of Dr. Michael Stabin at Vanderbilt University and Dr. Michael King at University of Massachusetts for the experimental data and the advice for my research, and the research group of Dr. Michael Ljungberg at Lund University for the SIMIND Monte Carlo simulation program.

I am extremely grateful to my primary supervisor, Dr. Troy Farncombe, who has directed, advised and supported my research work. His good advice, support and friendship has been invaluable on both an academic and a personal level, for which I am extremely thankful. I would like to also express my thanks to my second supervisor, Dr. Aleksandar Jeremic, for the support and assistance since the start of my doctoral work in 2005.

I wish to gratefully acknowledge the advice and encouragement from other two professors in my committees, Dr. Hubert deBruin and Dr. Colin Webber. Thanks to Dr. Tim Davidson, Dr. Shahram Shirani, Dr. Michael Noseworthy, and Dr. Gerald Moran, who have supported me during my Ph. D. comprehensive exam. I wish to thank Cheryl Gies, who is the Graduate Administrative Assistant in Electrical & Computer Engineering Department. She has always tried her best to help me and support my studies ever since I applied to McMaster University.

Finally, I am very grateful to my parents, Qinsheng Liu and Ruixing Zheng for all the support they have given me in my life. I would like to thank my husband, Xiaoli Zhang for his support and all the help over the years leading to the completion of this degree. My thanks to my beloved son, Brian Zhang; his birth is the happiest thing in my life. I am sorry that I had to leave him so often when he was so young. He provides me the best way to relax during thesis writing.

And thanks to you all who read and criticize my thesis!

Contents

List of Figures

List of Tables

Chapter 1

Preface

In radionuclide therapy, radionuclide products labeled with certain agents are introduced into the human body. The targeting drugs will attach the cancer cells and β particles are emitted from the radionuclide, depositing energies onto the cancer cells to kill them. However, the problem is: 1) How does the radionuclide distribute itself when it is injected into the human body? 2) What is the amount of energy deposited to a specific organ? The expected amount of activity should be very accurate because too high a dose is going to kill the healthy cells around the tumor, and too low a dose is not enough to kill the cancer cells. In this research, quantitative single photon emission computed tomography (SPECT) technique is introduced. It uses a rotating gamma camera designed to collect the γ photons emitted from the distributed radionuclide. Image reconstruction techniques are applied onto the projection images to recover the radioactivity distribution and estimate activity amount to certain organs.

When the γ rays emit from the human body, they may interact with body tissue and result in photon scatter or the absorption. This will reduce the resultant signal intensity, which is called attenuation. The attenuation and scatter will result in a reduction of image quality and accuracy of the estimated activity. In SPECT, a collimator is placed in front of the gamma camera to limit the detected photons along with certain directions. However, a collimator will introduce collimator response, which includes geometric response, septal penetration and collimator scattering. Collimator response reduces the spatial resolution of the projection images resulting in incorrect estimation of the organ boundary and activity. Therefore, these image degradation factors should be compensated for during the image reconstruction processor. Monte Carlo (MC) simulation, a very accurate nuclear medicine simulation tool is used to compensate for theses factors. The most significant drawback of MC is its low detection efficiency, therefore, the simulation speed is very slow. Variance reduction techniques (VRT's) have been developed to accelerate MC before it is incorporated into the image reconstruction.

This thesis aims at increasing the speed of MC simulation using variance reduction methods, and applying the accelerated MC methods to compensate for image degradation factors in the image reconstruction for both single isotope imaging and dual isotope imaging. Three VRT methods (convolution based forced detection, multiple projection sampling convolution based forced detection, convolution based forced detection incorporating collimator response sampling) are going to be developed in this thesis.

The accelerated Monte Carlo method is then incorporated into image reconstruction in order to provide accurate compensation of image degradation factors. This technique has further been applied to the problem of dual isotope imaging, in which the projection images may be contaminated by the crosstalk photons from one isotope to the other. Therefore, the crosstalk photons should be compensated in simultaneous dual isotope reconstruction.

For the following chapters, radionuclide therapy and reconstruction techniques are going to be introduced first, with the introduction of Monte Carlo. The fourth chapter will introduce three different variance reduction techniques as developed in this work. The fifth focuses on the image reconstruction incorporating accelerated Monte Carlo simulation, and the sixth chapter is the simultaneous dual isotope reconstruction while the crosstalk photons are compensated. The conclusion and future work is presented in the last chapter. Following are the frequently used abbreviations in this thesis.

Table 1.1: Frequently used abbreviations in this thesis.

CFD	convolution-based forced detection
CFD-MC	convolution-based forced detection Monte Carlo
CV	coefficient of variation
CPM	counts per minute
CPS	counts per second
CR	Collimator response
CST	cumulative septal thickness
EGS	electron gamma shower
ETRAN	electron transport
FBP	filter back-projection
FD	forced detection
FP	forced path
FWHM	full width at half maximum
FWTM	full width at tenth maximum
GEANT	geometry and tracking
GR	geometric response
HEGP	high energy general purpose
ITS	integrated tiger series
LEHR	low energy high resolution
LUT_{CR}	collimator response lookup table
LUT_{PL}	path-length lookup table
MC	Monte Carlo
MCAT	mathematic cardiac-torso
MCNP	Monte Carlo N-particle transport
MEGP	medium energy general purpose
ML-EM	maximum likelihood expectation maximization
MOBY	mouse phantom
MP-CFD	multiple projection sampling convolution-based forced detection
MRI	magnetic resonance imaging
NCAT	nurbs-based cardiac-torso
NMSE	normalized mean square error
OS-EM	ordered subset expectation maximization
PDF	probability density function
PET	positron emission tomography
PMT	photomultiplier tube
PSF	point spread function
RT	ray tracing
RT-CFD	ray tracing CFD
RT-MC	ray tracing model based Monte Carlo
SNR	signal to noise ratio
SP	septal penetration
SPECT	single photon emission computed tomography
TAC	Time activity curves
VRT	variance reduction technique

Chapter 2

Introduction to Nuclear Medicine and Image Reconstruction

2.1 Nuclear Imaging

Nuclear medicine uses radioactive isotopes in the diagnosis and treatment of disease. Two of the main uses of nuclear medicine are: i) radionuclide therapy, and ii) nuclear imaging. Radionuclide therapy uses high energy particles emitted from radionuclides to deposit lethal amounts of energy locally to cancer cells. In contrast, nuclear imaging is normally used for disease diagnosis. When γ photons are emitted from the radionuclides administered to the body, projection images are obtained by collecting the photons using imaging scanners, such as single photon emission computed tomography (SPECT) or positron emission tomography (PET).

2.1.1 Nuclear Imaging

Nuclear imaging is a noninvasive method which is able to help physicians diagnose various conditions. A series of images is acquired to study the constant (static imaging) or changing (dynamic imaging) activity distribution of one (single-isotope) or more radioactive materials (dual-isotope). The radioactive material used in the imaging scans is called a *radiopharmaceutical* or *radio-tracer*. The radiopharmaceutical is introduced into the human body by way of injection, ingestion or inhalation. As the radionuclide undergoes radioactive decay, it then emits energy in the form of γ rays or positrons (followed by annihilation and emitted γ rays). A detection device (called gamma camera) is rotated around the body to detect the γ photons thereby generating projection images at different angular views over 180° or 360°. The projection images are further reconstructed by computer algorithms, called image reconstruction, to recover the 3D radionuclide activity distribution within the patient. Once the 3D radio-tracer distribution is determined, the radiation dose absorbed by the different regions in the body can be calculated.

2.1.2 Radionuclides

Various factors exist for selecting the most appropriate radionuclides in nuclear medicine; these include: 1) The spatial and temporal distribution of the radiotracer should reflect the particular function or metabolism of the organ of interest. 2) Radionuclides should have short half-lives so that the photons are emitted as soon as possible. Short half-lives permit rapid scanning procedures, and also reduce the patient radiation exposure. The energy of photons should be low to ensure optimal imaging can be performed [1]. 3) Photons must have sufficient energy to penetrate body tissue with minimal attenuation.

Common radionuclides used in nuclear imaging include, among others, the radioisotopes of Iodine (^{131}I, ^{123}I), Gallium (^{67}Ga), Thallium (^{201}Tl), Technetium (^{99m}Tc), Oxygen (^{15}O), Carbon (^{11}C), Fluorine (^{18}F) and Nitrogen (^{13}N). Their physical characteristics vary and therefore the selection of a particular radionuclide depends on the diagnosis and the therapy for a certain disease. Their chemical characteristics are determined by the selection of target drugs. The radionuclide should be combined with the candidate molecules, and the product is administered [2]. Single photon emitters are usually produced by radionuclide generators, while positron emitters are usually produced by cyclotrons. The commonly used single photon emitters and positron emitters used in nuclear medicine are shown in Table 2.1.

Table 2.1: Commonly used single photon emitter and positron emitters.

Element	Radionuclide	Half-life	Energy γ (keV)	Energy β (keV)	Primary use
Gallium	^{67}Ga	78.3 hours	91, 185, 300	-	imaging
Yttrium	^{90}Y	64.1 hours	-	2280	therapy
Technetium	^{99m}Tc	6.02 hours	140	-	imaging
Indium	^{111}In	2.8 days	171,245	-	imaging
Iodine	^{131}I	8.0 days	364.5	606	imaging and therapy
Thallium	^{201}Tl	73.1 hours	68-82	-	imaging
Strontium	^{89}Sr	50.5 days	-	1463	therapy
Carbon	^{11}C	20.3 minutes	511	-	imaging
Nitrogen	^{13}N	10.0 minutes	511	-	imaging
Oxygen	^{15}O	2.0 minutes	511	-	imaging
Fluorine	^{18}F	110 minutes	511	-	imaging
Rubidium	^{82}Rb	1.27 minutes	511	-	imaging

Commonly used radiopharmaceuticals in nuclear medicine are listed in Table 2.2 [3]. Different radiopharmaceuticals are used for different diseases. The most often used radionuclide is ^{99m}Tc (in SPECT), and ^{18}F (in PET). The primary energy of ^{99m}Tc photons is $140keV$, which is the optimal energy for detection with NaI(Tl) scintillation crystals as used in the Anger camera. The half-life of ^{99m}Tc is 6 hours. The short half-life and low photon energy make it possible for a patient to absorb low doses even with a relatively large amount of administrated radionuclide. ^{99m}Tc is produced from a ^{99}Mo generator prior to use. Therefore, an outside source can be used to produce and deliver it, making its cost relatively low. ^{18}F is a frequently used isotope in PET imaging. The production of most PET imaging agents requires a cyclotron. Few hospitals have their own cyclotron to ensure the supply, but rather rely on ^{18}F's 2-hour half-life in order to allow shipment of ^{18}F labeled radiopharmaceuticals, regionally.

Single photon emitters are used in SPECT imaging and positron emitters for PET scanning. SPECT tracers are usually longer lasting than PET tracers due to their longer half-lives, and do not require an onsite cyclotron to produce and so are usually less expensive than PET tracers. While many similarities exist [4, 5] between PET and SPECT, the focus will be on SPECT imaging in this work.

2.1.3 Clinical Application of Nuclear Imaging

In clinical practice, nuclear imaging is used for myocardial perfusion imaging, brain imaging, bone imaging, renal imaging among other applications.

Myocardial Perfusion Imaging

Myocardial perfusion imaging is a method used to determine myocardial blood flow by means of the distribution of radio-labeled perfusion agents. It is used for diagnosis and localization of ischemic heart disease, which is caused by inadequate blood supply to the heart [6]. Frequently used radiopharmaceuticals in imaging are ^{99m}Tc labeled sestamibi or ^{201}Tl labeled thallous chloride [7–9].

A low dose of radioactive tracer is injected into the patients' body and circulates in the bloodstream. A small amount of this tracer is taken up by the heart myocardium. The radiopharmaceutical stays in the myocardium and emits γ rays which are detected by the gamma camera. The heart rate is raised either by pharmacologic means or through exercise to induce myocardial stress and imaging is performed to acquire images after stress and at rest to reveal the distribution of radiopharmaceutical under different conditions. The relative accumulation of radiopharmaceutical denotes the relative blood flow to different regions of myocardium. The relative perfusion uptake difference of stress and rest stages is studied to evaluate whether the blood supply in the heart is adequate and to localize the defect size [4, 10]. Ischemic heart disease is depicted as an area of abnormal uptake of the radiopharmaceutical [11].

Table 2.2: Commonly used radiopharmaceuticals and their applications in nuclear medicine [3].

Application Area	Pharmaceutical	Purpose
Central Nervous System	$^{123}I - Isopropyl - p - iodoamphetamine(IMP)$	Cerebral perfusion and metabolism (decreased uptake in infarcted tissue)
	$^{99m}Tc - Hexamethylpropylene$ Amine Oxime (HMPAO)	Cerebral perfusion
	^{99m}Tc-Ethyl Cyteinate Dimer (ECD)	Cerebral perfusion
	$^{18}F - Fluorodeoxyglucose(FDG)$	Glucose metabolism
Thyroid	$^{123}I - SodiumIodide$	Thyroid uptake
	^{99m}Tc pertechnetate	Thyroid size
Respiratory	^{133}Xe and ^{127}Xe gas	Detection of airway obstructions
	^{99m}Tc DTPA aerosol	Ventilation
	^{99m}Tc macroaggregated albumin (MAA)	Lung perfusion
Heptobiliary	^{99m}Tc albumin colloid ^{67}Ga gallium citrate	Tumour detection Detection of abscesses and tumors
	^{99m}Tc-IDA derivatives (HIDA, PIPIDA, etc)	Gallbladder imaging
Renal	^{99m}Tc-Mercaptoacetyl-glycylglycylglycine (MAG3)	Renal plasma flow
	^{99m}Tc-DTPA	Glomerular filtration
Skeletal	^{99m}Tc-phosphate	Bone blood flow and bone formation rate
Myocardial	^{99m}Tc-Sestamibi	Blood perfusion
	^{99m}Tc-Teboroxime	Perfusion
	^{201}Tl-Thallous Chloride	Perfusion

Brain Imaging

Brain Imaging is another application of nuclear medicine. The metabolism of different brain tissues varies with the type of radiopharmaceutical and the type of tissue. Normally, higher metabolism regions will take up more tracer and the concentration of the tracer shown on the projection image will be high [4]. Using different compounds, nuclear imaging can show blood flow, oxygen and glucose metabolism and drug concentration in the brain thereby aiding in the study of the physiology and neurochemistry.

A very useful radiopharmaceutical is ^{18}F-fluorodeoxyglucose (FDG) used in PET scanning. Glucose is a sugar which brings energy for the brain and other organs. When the brain is working, active regions metabolize more glucose. Images depicting different amounts of radiotracer uptake denote the level of activities for different regions [12, 13]. ^{99m}Tc labeled hexamethylpropylene amine oxime (^{99m}Tc-HMPAO) SPECT scanning is widely used to evaluate regional aberrations in blood flow, and ^{99m}Tc labeled diethylene triamine pentaacetate (^{99m}Tc-DTPA) has been used to image tumors and strokes.

Lung Imaging

Another application of nuclear imaging is lung imaging. This is a test that is commonly used to detect pulmonary embolism. Two types of lung scans, ventilation and perfusion scans are usually done consecutively. During the perfusion scan, the radioactive tracer, commonly ^{99m}Tc macroaggregated albumin (MAA), is injected into the body, circulates in the bloodstream and deposits in the lungs. The projection images can also show areas that receive too much, or not enough blood. In the ventilation scan, a radioactive tracer, such as ^{133}Xe gas or ^{99m}Tc-aerosol is inhaled into the lungs. Lung projection views are acquired and depict areas of gas ventilation.

If the lungs are working normally, the blood flow images in the perfusion scan match the air flow images in the ventilation scan. A mismatch between them might indicate the presence of a pulmonary embolism. Because of the different methods of introducing the radionuclides into the body, ventilation and perfusion scans can be done separately or together. If both scans are done, the test is called a V/Q scan [14, 15].

Bone Imaging

Bone imaging is a test to identify areas of increased or decreased bone metabolism, which will help to evaluate damage to the bones, detect cancer that has spread to bone, or monitor the conditions that can affect the bones. Bone scanning can also help to demonstrate fracture that is difficult to detect by X-rays [4, 16, 17].

Radiotracers such as ^{99m}Tc labeled methylene diphosphonate (MDP) are injected into the bloodstream through a peripheral vein. New bone formation will take up more radio-tracer than other tissues and will appear as brighter regions ("hot spots"). Hot spots might indicate fractures, infections, tumor or other processes that will produce new bone formation. In contrast to high concentration regions, the areas with lower concentration are called "cold spots", and represents poor blood flow of these area, and could correspond to areas of bone destruction [18–20].

Renal Imaging

Renal Imaging is performed to see how well the kidneys are working, or determine whether the kidneys are obstructed, or whether high blood pressure is caused by the kidney. A small amount of radioactive substance such as ^{99m}Tc-DTPA or ^{99m}Tc-MAG3, is introduced into the body via the blood stream. Imaging of the blood flow in the kidney is able to show regions with abnormal kidney function. There are usually two types of kidney scans: kidney perfusion study and function study. The perfusion study is used to evaluate whether there is enough blood flow through the kidneys. The rate at which the kidneys filter a patient's blood is determined by the amount of radiotracer entering and exiting the kidneys to see whether the kidney is able to remove the waste out of the body. A kidney function study is used to measure the time required for the tracer to move through the kidney [4, 21, 22], thereby providing a measure of functional ability.

Other Imaging

Other nuclear imaging includes gastrointestinal (GI) tract imaging and oncology imaging. GI tract imaging includes esophagus, stomach, intestinal tract, pancreas, liver, biliary system and salivary glands imaging. Oncology imaging is used to localize and classify different types of tumors. Since nuclear imaging is useful in displaying physiological function, processes such as the growth of a tumor can often be monitored, even when the tumor cannot be adequately visualized using any of the other modalities [4, 23].

2.2 Equipment Used in Nuclear Imaging

2.2.1 The Gamma Camera

In nuclear medicine, a device called a gamma camera is used to detect the γ rays emitted as a result of radioactive decay. A gamma camera consists of a collimator, scintillation crystal, photomultiplier tube (PMT) array, positioning & summing circuits, pulse height analyzer (PHA), acquisition computer and analyzing computer. SPECT is performed by using gamma cameras, usually one, two, or three detector heads rotating around the patient. The schematic of a gamma camera is shown in Fig. 2.1.

Collimator

When emitted, γ rays will travel in all directions. A ray that originates at the top left side of one object may be detected at the bottom right side of the camera. The resultant image will be meaningless without any limitation of the photon traveling directions.

A collimator is a high density plate with a large number of holes. It is typically made of lead and placed in front of the crystal, and used to filter the stream of rays traveling in the directions along with the collimator holes.

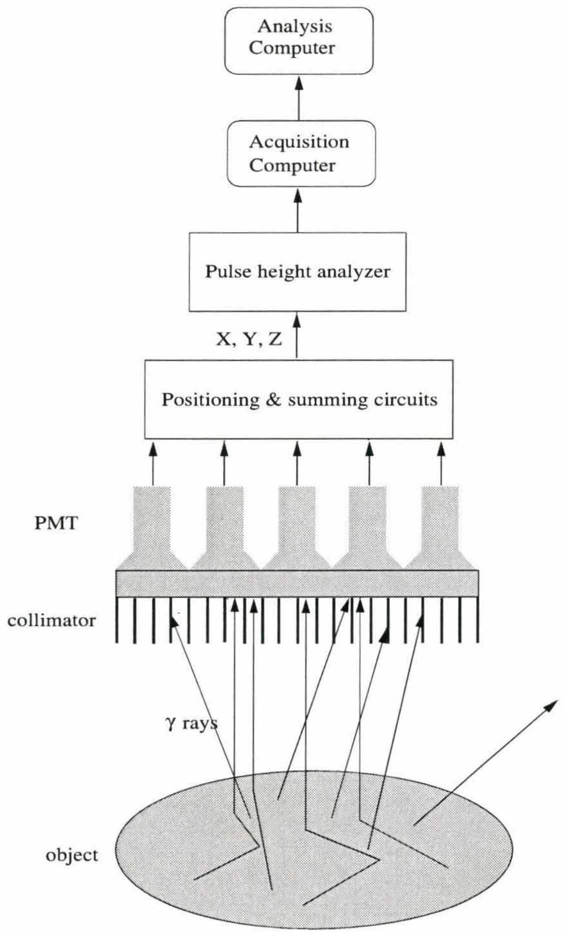

Figure 2.1: Basic components of the SPECT detector. γ rays are emitted from the patient, and those traveling in the direction of collimator holes are collected by the crystal. Visible photons are produced in the crystal and travel into the PMT. Electrons are emitted and the signal is amplified by the PMT. The positioning & summing circuit is used to localize the incident photon event and pulse height analyzer is applied to determine whether the input photon energy matches the energy window. The photon event is collected by the detector and projection image is recorded on the computer.

There are four primary types of collimators based upon the hole orientation: pinhole, parallel hole, diverging and converging hole (Fig. 2.2). Different collimators allow various maximum photon traveling angles to the collimator [2]. The most commonly used collimator is the parallel collimator, which will be discussed in more detail later in this thesis.

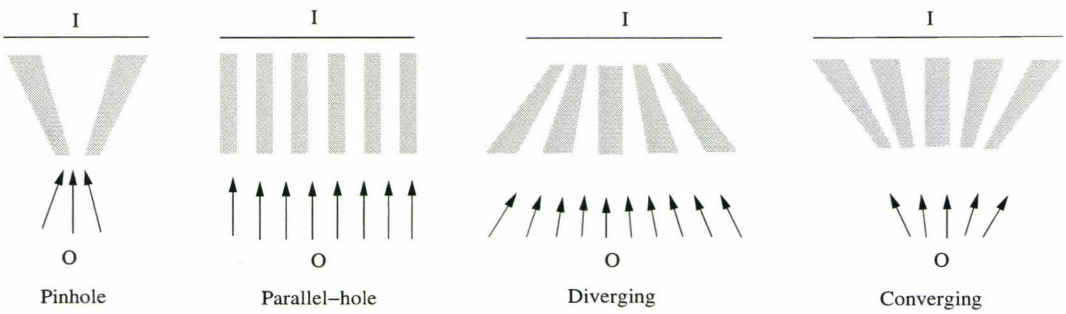

Figure 2.2: Different types of collimators. The object is denoted as O, and the projection view is I.

Fig. 2.3 shows depictions of four commonly used collimator hole patterns : 1) hexagonal holes in a close-packed array. 2) triangular holes in point-to-point array. 3) circular holes in a close-packed array and 4) square holes in a square array [24–26]. The hexagonal hole collimator is the most common collimator pattern used clinically. The white areas in Fig. 2.3 correspond to the collimator holes, which allow γ rays to pass through. The collimator walls (gray areas) between two holes are called septa. Due to the high density of the collimator material (i.e., lead), septa are able to stop most low energy photons, but some high energy photons may penetrate the septa and get detected. This is called septal penetration and will be discussed at greater length in Chapter 3.

A collimator is characterized by parameters such as spatial resolution and detection efficiency [24]. It has been verified by Metz, et al. [26] that the spatially averaged geometric component is effectively independent of hole shape given the collimator length and the ratio of hole area to septal area when the penetration is negligible.

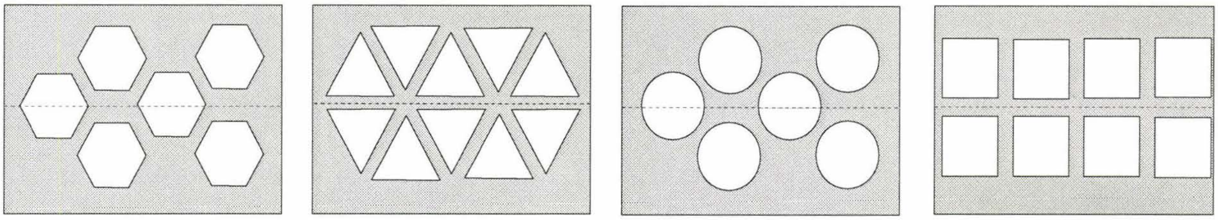

Figure 2.3: Different collimator hole shapes. The white areas denote the collimator holes, and the gray areas are collimator septa. Note each collimator is produced by several "unit" cells.

Photons traveling through the collimator can be divided into three components: 1) geometric photons, which pass through the collimator holes; 2) penetrating photons, which pass through the collimator septa and are detected; 3) scattering photons, which interact with the collimator material and are detected. In order to decrease the effect of the penetrating and scattering photons, the collimator septa are expected to be as thick as possible. However, thick collimator septa reduce the collimator efficiency as the number of detected photons decreases. The size of the collimator hole also affects the collimator efficiency and spatial resolution. A large hole contributes to high detection efficiency but poor spatial resolution, while small holes will achieve the opposite effect. Beck, et al. used a ray-tracing (RT) technique to find the optimal collimator pattern and hole size [27]. Low energy collimators usually have thinner septa and smaller holes, while high energy collimators have thicker septa and bigger holes. Therefore, low energy collimators usually have high resolution but poor detection efficiency, while high energy collimators have poor resolution but high efficiency. A typical low energy high resolution (LEHR) collimator has a hole diameter in the range of 1.5 mm-2.0 mm, septal thickness of about 0.2 mm, and collimator height around 3.5 cm. For a high energy general purpose (HEGP) collimator, the diameter of the hole is about 4 mm, the septa are about 2 mm thick, and the height is about 6.5 cm. The parameters of some commonly used collimators can be seen in Table 2.3.

The collimator spatial resolution, R_c, is defined by the full width at half maximum (FWHM), measured in mm, and is derived from the profile of the point spread function (PSF). A PSF is obtained by taking the projection image of a point source at a certain distance from the detector. Fig. 2.4 shows the PSF for a HEGP collimator when an ^{131}I point source (364.5 keV photons) is placed at a distance of 33 cm away from the collimator face. The central dark region corresponds to the geometric photons, while the six star-like lines are related to septal penetration. The rest of the image includes contributions from the collimator scattered photons. The collimator response will be discussed in more detail in Chapter 3.

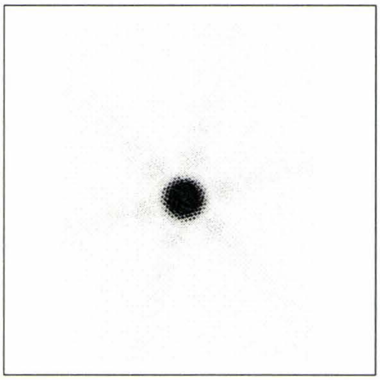

Figure 2.4: Point spread function of HEGP collimator when an ^{131}I point source is placed 33 cm away from the detector. The center dark region is the geometric component, the star-like region corresponds to septal penetrating photons, and the background region is contributed by the collimator scattering photons.

Scintillation Crystal

The scintillator is a monolithic crystal placed behind the collimator, made up of a special material that fluoresces when γ photons are incident. After γ photons travel through the collimator and hit the crystal, they interact with the detector materials by means of Photoelectric Effect or Compton Scattering (Note: the photon interaction types will be introduced in section 1.4.2). The photons are absorbed by the crystal, and a number of electrons and holes are produced. The number of electrons created per unit of energy deposited by the γ photon is called *conversion* *efficiency.* Electrons are ejected from valence bands. When an electron returns to the valence band, a visible light photon is generated. The number of visible light photons is proportional to the incident photon energy.

In order to achieve high detection efficiency, the crystal material must be dense and contain an element of high atomic number. The properties of some scintillator materials used in nuclear medicine are shown in Table 2.4. The most commonly used material in SPECT is Thallium doped Sodium Iodide (NaI(Tl)), which has high efficiency to convert γ rays in the energy range of 50-250 keV to visible light. Usually about one visible light photon is produced for every 23 eV of radiation energy absorbed. NaI(Tl) is most effective when the incident energy is lower than 250 keV, otherwise, the detection efficiency will be reduced as a result of increased Compton Scattering. Therefore, PET imaging, which includes the detection of 511 keV γ photons, requires denser and higher atomic number materials such as Bismuth germanate (BGO) or Lutetium oxyorthosilicate (LSO) to stop the photons (511 keV) [2, 28].

Photomultiplier Tube

The visible light produced in a scintillator crystal is very weak and is difficult to detect. Thus, the crystal is usually used in combination with photomultiplier tubes (PMT's). A PMT is a vacuum tube that consists of a photoemissive cathode (photocathode), a series of electron multipliers (dynodes) and an electron collector (anode), as shown in Fig. 2.5.

Visible light photons travel out of the crystal and strike the photocathode. The photocathode is a photoemissive substance which ejects electrons when visible light photons are absorbed. The number of electrons emitted is proportional to the number of incident photons. Typically, 10 visible light photons will yield 1-3 photoelectrons. A focusing electrode directs the electrons to travel toward the first dynode, which holds a positive voltage (200-400 V) relative to the photocathode. Each of the dynodes maintain a voltage of 50-150 V higher than the previous one.

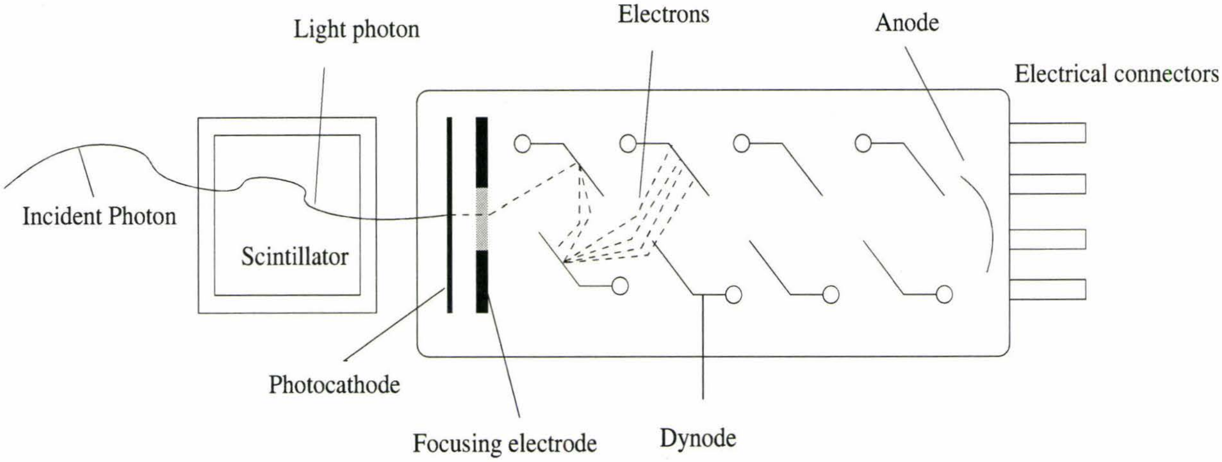

Figure 2.5: Schematic of a scintillator/PMT detector. The primary parts of a PMT are a photocathode, a series of dynodes and an anode. *source: http://en.wikipedia.org/wiki/Photomultiplier_Tube.*

Secondary electrons are emitted from the dynodes and are accelerated toward the next dynode. The multiplication factor of each dynode is between 3-6, therefore, the total multiplication factor of a 10-stage tube is between $3^{10} - 6^{10}$. The final electrons emitted from the last dynode reach the anode and are converted into an electrical current. Therefore, the amplitude of the current is proportional to the number of visible photons striking the photocathode and also is proportional to the incident γ photon energy. [2, 28].

Positioning & Summing Circuit and Pulse Height Analyzer

Between the crystal and PMT's, there is a component called the light guide. When the visible light is emitted from the crystal, the light guide spreads the light out to multiple PMT's, as seen in Fig. 2.6. After the signal is amplified by the PMT's, the location of the original photon events can be determined by means of a positioning circuit. The accuracy to which a detector is able to localize a photon event is known as the intrinsic resolution, R_i.

Table 2.3: Parameters from commonly used collimator for 1 μCi source. FOV = Field of View (mm), CP = Calculated % Penetration, SS = System Sensitivity (counts per minute (cpm)/μCi) ±7%, SR = System Resolution, TH = Type of Hole (mm), HD = Hole Diameter (mm), ST = Septal Thickness (mm) and HL = Hole Length (mm).
(1) Measured with ^{99m}Tc in 20% window
(2) Measured with ^{67}Ga in 20% window
(3) Measured with ^{131}I in 20% window

Description	Application	FOV @ 100mm	CP @ 140keV	SS	SR FWHM (mm) @ 100mm 3/8"; 5/8"	TH	HD	ST	HL
Low Energy General Purpose (LEGP)	General Application	540×400	0.8	320/260$^{(1)}$	9.0; 9.2	hex	1.9	0.2	35
Low Energy High Resolution (LEHR)	Bone Scans	540×400	0.3	180/150$^{(1)}$	7.4, 7.7	hex	1.5	0.2	35
Medium Energy General Purpose (MEGP)	^{67}Ga and ^{111}In studies	540×400	2.0	330/220$^{(2)}$	9.4, 9.6	hex	3.0	1.05	58
High Energy General Purpose (HEGP)	^{131}I	540×400	2.0	340/75$^{(3)}$	10.7, 10.8	hex	4.0	1.8	66

Table 2.4: Commonly used scintillator material in nuclear medicine. Note: BaF_2 has two components, a fast-decaying component and a slow-decaying component.

Material	Density(g/cm^3)	Effective atomic number	Light decay time (ns)	Peak emission (nm)
NaI(Tl)	3.67	50	230	415
BGO	7.13	74	300	480
LSO(Ce)	7.40	66	40	420
BaF_2	4.89	54	0.8, 620	225,310

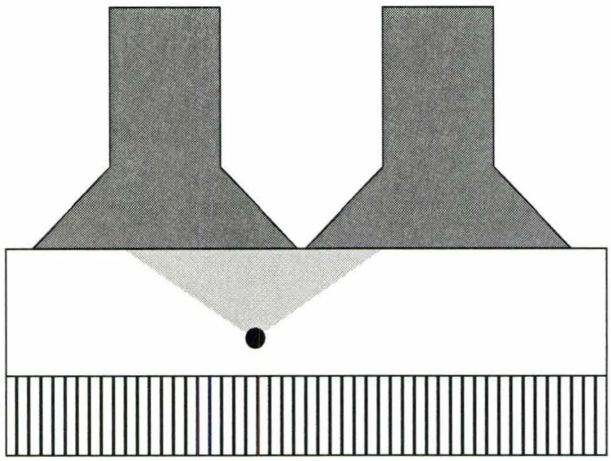

Figure 2.6: Schematic of light guide. The visible light is spread to multiple PMT's.

Fig. 2.7 presents a schematic of the positioning and summing circuit. Each PMT is connected with four output leads through four independent resistors. The resistance values are assigned to be proportional to the location of the PMT relative to the center of the crystal. When γ photons strike the crystal, the output of each PMT is divided into four outputs denoted X_i^+, X_i^-, Y_i^+, Y_i^-, where i is the index of the PMT. The outputs from each PMT are weighted by the appropriate resistance values and further combined with a summing circuit to obtain the overall signals, X^+, X^-, Y^+, Y^- :

$$\begin{aligned} X^- &= \textstyle\sum_{i=1}^{n} X_i^- \\ X^+ &= \textstyle\sum_{i=1}^{n} X_i^+ \\ Y^- &= \textstyle\sum_{i=1}^{n} Y_i^- \\ Y^+ &= \textstyle\sum_{i=1}^{n} Y_i^+ \end{aligned} \tag{2.1}$$

where, n is the number of PMT's. The entire signal, Z, is the sum of the total output of the summing circuits, given by Eq. 2.2:

$$Z = X^- + X^+ + Y^- + Y^+ \tag{2.2}$$

The value of Z is proportional to the number of visible light photons, and is also

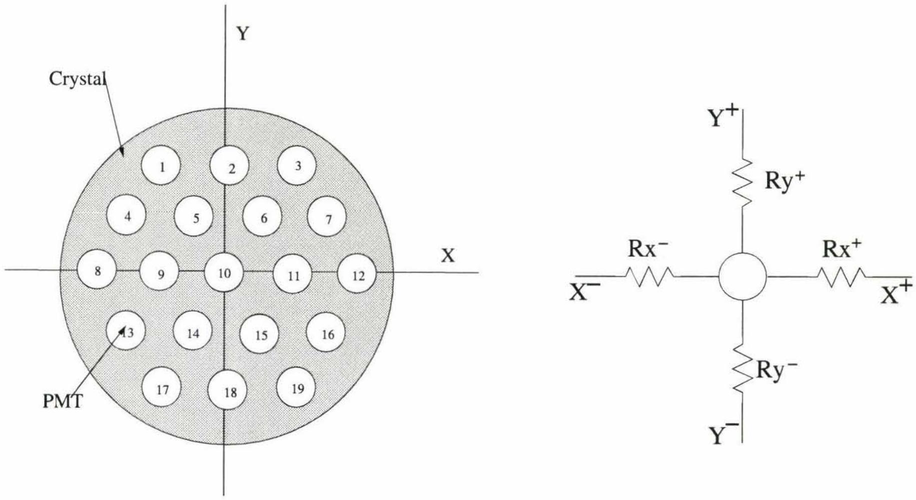

Figure 2.7: Schematic of positioning & summing circuit. Left: Schematic of positioning & summing circuit as the crystal in combination with 19 PMT's. Right: Each PMT connects with a positioning & summing circuit [2].

proportional to the amount of incident γ photon energy. Finally, the location (X, Y) of a photon event can be written as:

$$\begin{aligned} X &= \tfrac{k}{Z}\left(X^{+} - X^{-}\right) \\ Y &= \tfrac{k}{Z}\left(Y^{+} - Y^{-}\right) \end{aligned} \tag{2.3}$$

where, k is a scaling factor determined by the detector size.

When the amount of photon energy is determined, a device called a pulse height analyzer (PHA) is used to compare the detected energy with an amplitude range to see whether or not to accept a photon event. Fig. 2.8 explains how a PHA works. When the amplitude of the output signal is too high or too low, the PHA will reject the photon event. Only those signals with energy between the energy window thresholds are accepted [2, 28].

Acquisition Computer and Analyzing Computer

An acquisition computer is then used to collect the output current/voltage signal and produce projection images. The acquisition parameters such as the number of detector bins, the size of the detector bins, the number of the projection angles,

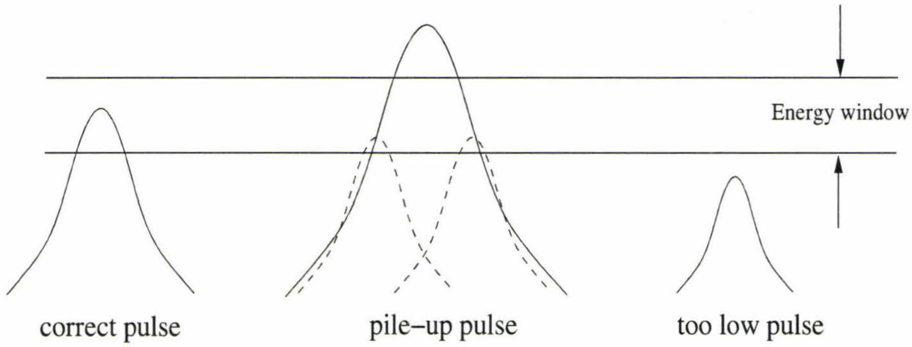

Figure 2.8: Schematic of pulse height analyzer. PHA helps to select the photon events with the energy meet the requirement of the energy window. The left is the accepted correct pulse. The middle is the pulse with too high amplitude because of the overlapping of two pulses, and the right is the pulse related to too low energy.

the scanning time of each projection and the gain of PMT are controlled by the acquisition computer. The analyzing computer is used to reconstruct the acquired images and display them.

Data acquisition types

In nuclear medicine, there are three main data acquisition types: static, dynamic, and gated imaging. The static study is the most common and is performed when the change in tracer distribution is slow compared to the time of imaging. The projection images in a static study represent the time averaged result of the entire projection process. Compared with static imaging, dynamic imaging generates several groups of projection images related to the change of radioactivity distribution over time. Gated imaging is used for acquiring data synchronized with cardiac or breathing rhythm. Projection images denote the organ motion during one cardiac (or breathing) cycle. Each cardiac (or breathing) cycle is short ($\sim$ few seconds), therefore, the projection images in several cycles should be combined to produce an image of acceptable quality. In this thesis, primarily the static imaging method will be discussed.

2.2.2 Single Photon Emission Computed Tomography (SPECT)

Single photon emission computed tomography (SPECT) is a nuclear medicine imaging technique that uses one or more rotating gamma cameras to acquire multiple projection views and combines them in order to obtain a 3D representation of tracer distribution, as seen in Fig. 2.9. When the injected radionuclide emits photons of certain energies, the photons are collected from multiple projection views over 180° or 360°. The advantages of SPECT over planar imaging is the improvement of the contrast between different organs, better spatial information, and as discussed in this work, the ability to obtain more accurate quantitation estimates.

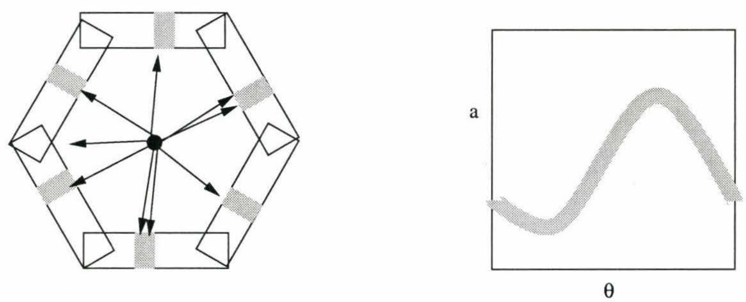

Figure 2.9: A SPECT scanner consists of one or more rotating gamma cameras (left image). θ is the angle of the detector, and a refers to the detector bins. The value of each pixel corresponds to the number of photons collected by the detector (right image). A sinogram image is obtained by acquiring projections of a point source.

2.3 Image Reconstruction

Many clinical applications use the planar images acquired by the gamma camera to diagnose disease. However, it is often better to investigate the interior 3D radioactivity distribution to see the functional information of different organs. An image reconstruction method is applied to the projection views to generate several tomographic images of the patient.

Image reconstruction is an inverse problem used to identify the input radionuclide distribution information from knowledge of projection views acquired at different angles around the body. The mathematical reconstruction method was first developed by Radon in 1917 [29]. In general, there are two types of image reconstruction methods: i) analytical and ii) iterative. Filtered back-projection (FBP) and maximum likelihood expectation maximization (ML-EM) methods are two well-known analytical and iterative methods, respectively. Prior to the discussion of image reconstruction methods, two basic modeling steps used in image reconstruction are introduced: analytical forward projection and simple back-projection.

2.3.1 Analytical Forward Projection

The process of making a 2D projection from a 3D activity distribution is known as forward projection. Analytical forward projection is performed by summing up the photons traveling along the potential path from the object to the gamma camera. It is a simulation of the real acquisition process. The accuracy of the reconstruction result mainly depends upon the accuracy of photon transport modeling in the forward projection process. Fig. 2.10 shows the configuration of a very simple analytical forward projection.

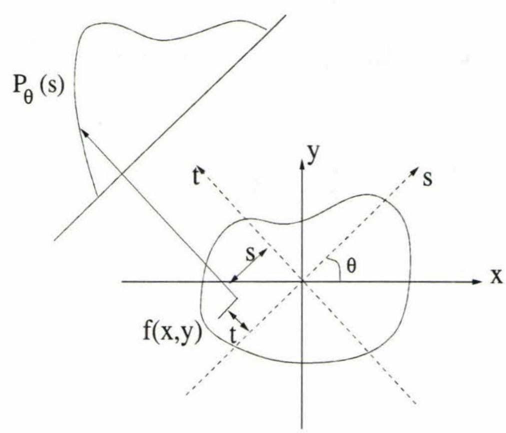

Figure 2.10: Schematic of 2D SPECT image projection using parallel-hole collimator-detector system, assuming infinitely high spatial resolution and no scattering. The projection value $P_\theta(s)$ at angle θ is integral of the $f(x,y)$ that is parallel with t-direction.

The origin is related to the initial unrotated system, which is denoted as (x,y) coordinate. The detector is initially placed along the x-axis direction. When the detector is rotated around this origin, a new coordinate (s, t) is generated at an angle θ with the fixed x-axis. The detector, therefore, is along the s-axis direction. The relationship between the new coordinate (s, t) and the fixed coordinate (x,y) is:

$$\begin{cases} s = x\cos(\theta) + y\sin(\theta) \\ t = -x\sin(\theta) + y\cos(\theta) \end{cases} \tag{2.4}$$

Assuming infinitely high spatial resolution and no photon scattering, the 2D data acquisition can be mathematically formulated as:

$$p_\theta(s) = \int_{D(s)} f(s,t)exp\left(-\int_{d(s)} \mu(s,t')dt'\right)dt \tag{2.5}$$

where, $D(s)$ is a line along the t-direction from point (s, t) in the object to the detector, $d(s)$ is the distance between the integral point (s, t') to the edge of the object along with t-direction, and $\mu(s, t')$ is the attenuation value at point (s, t').

It is proposed that the interior of the object is able to be reconstructed if enough projection views are taken by means of integral transform over straight lines at different angles around the object. Eq. 2.5 can be reduced to the Radon transform when there is no attenuation (i.e., $\mu(s,t) = 0$). Combining Eq. 2.4 and Eq. 2.5 when $\mu(s,t) = 0$, we will get:

$$p_\theta(s) = \int_{D(s)} f(s,t)dt = \int_{-\infty}^{\infty}\int_{-\infty}^{\infty} f(x,y)\delta(x\cos\theta + y\sin\theta - s)dxdy \tag{2.6}$$

The Radon transform was first introduced in 1917 by Johann Radon [29]. Image reconstruction is based upon the inverse Radon transform to recover the interior distribution $f(x,y)$ given the set of projection data, $p_\theta(s)$.

The Radon transform, which is closely related to the Fourier transform, can be described in Eq. 2.7:

$$P_\theta(\nu_s) = \int_{-\infty}^{\infty} p_\theta(s) e^{-j\nu_s s} ds = \int_{-\infty}^{\infty} \int_{-\infty}^{\infty} f(x,y) e^{-j\nu_s(x\cos\theta + y\sin\theta)} dxdy \tag{2.7}$$

let $v_x = v_x \cos\theta, v_y = v_s \sin\theta$, Eq. 2.7 can be written as:

$$P_\theta(\nu_s) = F(\nu_x, \nu_y) = \int_{-\infty}^{\infty} \int_{-\infty}^{\infty} f(x,y) e^{-j(\nu_x x + \nu_y y)} dxdy \tag{2.8}$$

Eq. 2.8 is the Fourier slice theorem, which states that the one-dimensional (1D) Fourier transform (FT) of a parallel projection at angle θ is equal to the line profile of the 2D FT of the object distribution at the same angle, as illustrated in Fig. 2.11. Therefore, it is possible to estimate the object by performing the 2D inverse Fourier transform.

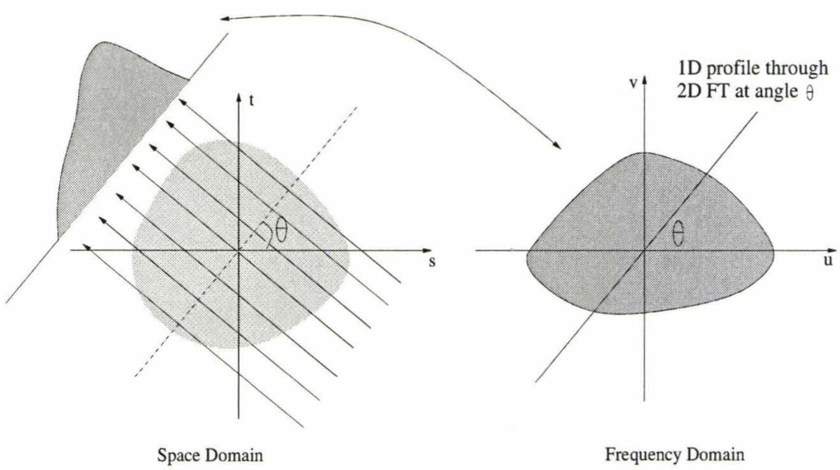

Figure 2.11: Fourier slice theorem. The Fourier transform of the projection at angle θ is equal to the line profile through the 2D FT of the image at angle θ in Fourier domain.

Fig. 2.12 shows a 2D 128×128 Shepp-Logan phantom and its forward projection without attenuation when the gamma camera is rotated around the phantom over 180° and acquires 180 projection views at each 1° using simple analytical projection. Fig. 2.12(b) combines all the 1D projection views together, which is referred to as a sinogram. The calculation of the values on the projection images by analytical forward projection can be seen in Fig. 2.13(a).

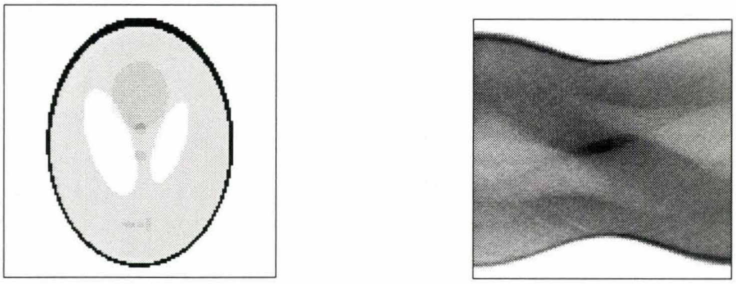

(a) (b)

Figure 2.12: Shepp-Logan phantom (a) and its forward projection (b) over 180°. X-axis denotes the detector angle θ, and y-axis is the value of each projector bin.

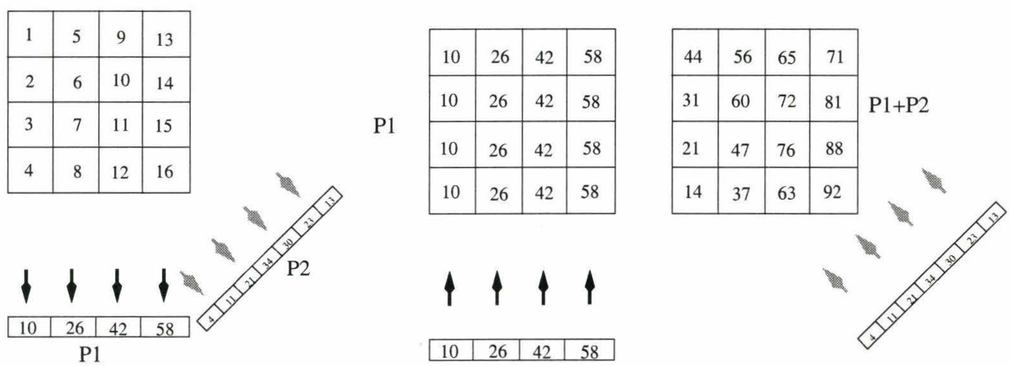

(a) (b)

Figure 2.13: Simple SPECT forward projection and back-projection. a) A gamma camera acquires a set of projection views by taking the integral values along the rays that are perpendicular to the detector. The values shown on the detectors are the cumulative photon numbers from each point in the object along a certain path. b) Simple back-projection takes each value of the projection views and smears it back to the object along the path from which it was originally acquired.

2.3.2 Simple Back-projection

Simple back-projection is used to recover the 3D activity distribution from the set of projection images, as shown in Fig. 2.13(b). The mathematical expression of simple back-projection for N projection profiles can be described by:

$$f'(x,y) = \frac{1}{N}\sum_{i=1}^{N} p(x\cos(\theta_i) + y\sin(\theta_i), \theta_i) \tag{2.9}$$

where p denotes the value of the projection image, θ_i is the i^{th} projection angle and $f'(x,y)$ is the back-projected image. This back-projected image is equal to the true image convolved with the blurring function $1/r$:

$$f'(x,y) = f(x,y) * \frac{1}{r} \tag{2.10}$$

where, r is the distance from the center of the point-source location [2]. This effect is called $\frac{1}{r}$ blurring (Fig. 2.14). Fig. 2.14 presents the simple back-projected result of Shepp-logan phantom. It is noise-free, but very blurred due to the $\frac{1}{r}$ artifact.

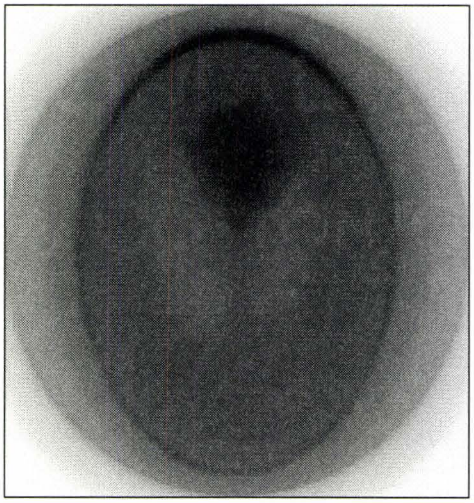

Figure 2.14: Simple back-projection result of Shepp-logan phantom.

2.3.3 Analytical Reconstruction Methods

In SPECT imaging, simple back-projection images are affected by several factors such as the $\frac{1}{r}$ effect, photon attenuation, scattering and collimator-detector response. Analytical reconstruction methods are applied to compensate for some simple factors such as the $\frac{1}{r}$ effect. A very well-known analytical method, filter back-projection (FBP) method, is discussed here.

The objective of FBP is to eliminate the effect of $\frac{1}{r}$ in Eq. 2.10, which corresponds to the low frequency component. In order to suppress the low frequency component, the ramp filter, as shown in Fig. 2.15, is used in FBP. Each projection image is convolved with the FT of the Ramp filter, and the resultant image is used in the subsequent back-projection. The ramp filter is the optimal way of eliminating the $\frac{1}{r}$ blur in the noise-free case. However, real projection images are inevitably contaminated by noise, as a result of the decay process, resulting in a reduction in image quality of the projection images; furthermore, this makes the reconstructed images noisy. Most noise corresponds to high spatial frequencies in the images. The application of the ramp filter increases the high frequency component as a result of suppressing the low frequency component. This results in enhancement of the noise, which degrades the signal to noise ratio (SNR). Therefore, the ramp filter is often multiplied by a low-pass filter resulting in a band-pass filter in order to suppress the high frequencies as well as to eliminate the blurring. Fig. 2.16 shows two well-known filters, Hann filter and Shepp-Logan filter, which are mathematically described as:

$$Hann : H(k) = 0.5|k| \left(1 + \cos \frac{\pi k}{k_{cut-off}}\right) \tag{2.11}$$

$$Shepp - Logan : H(k) = \frac{2k_{cut-off}}{\pi} \sin \frac{|k|\pi}{2k_{cut-off}} \tag{2.12}$$

where, k is frequency, and $k_{cut-off}$ is the cut-off frequency.

Fig. 2.17 shows back-projection results using simple back-projection and different

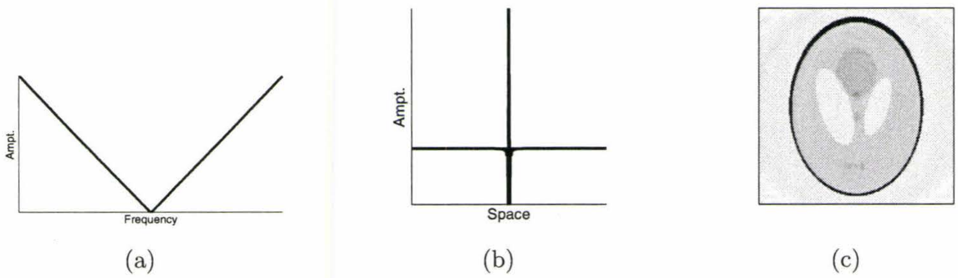

Figure 2.15: Ramp filter. (a) is the filter in 1P frequency domain (k-space), and (b) is the filter illustration in the spatial domain. (c) shows the FBP reconstruction result. The blurring artifact is removed.

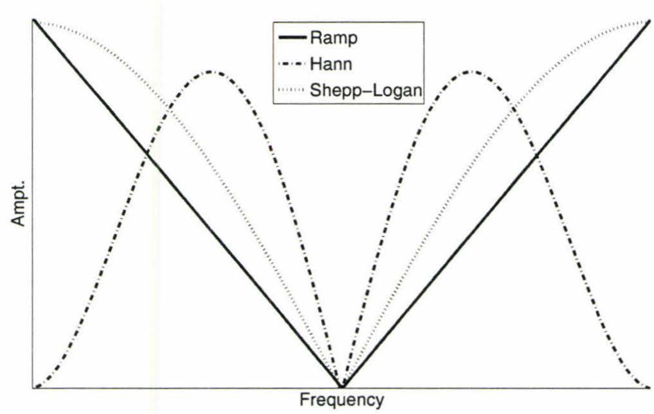

Figure 2.16: Ramp filter and two other well-known filters used in filter back-projection to suppress the amplification of high frequency noise and the edge ringing, $k_{cut-off}$ is chosen to be equal to k_{max}. The center frequency corresponds to 0Hz.

filters for the Shepp-Logan phantom. Compared with simple back-projection, the use of the ramp filter eliminates the $\frac{1}{r}$ blurring, but amplifies the high frequency noise. In Fig. 2.17(c) and Fig. 2.17(d), the cutoff frequency of Hanning and Shepp-Logan filter is chosen as 0.5. It can be seen that the noise is reduced compared with Ramp filter back-projection result. Note that the value of the filtered back-projected image only presents the relative radionuclide concentration of each voxel and does not denote the exact radioactivity value.

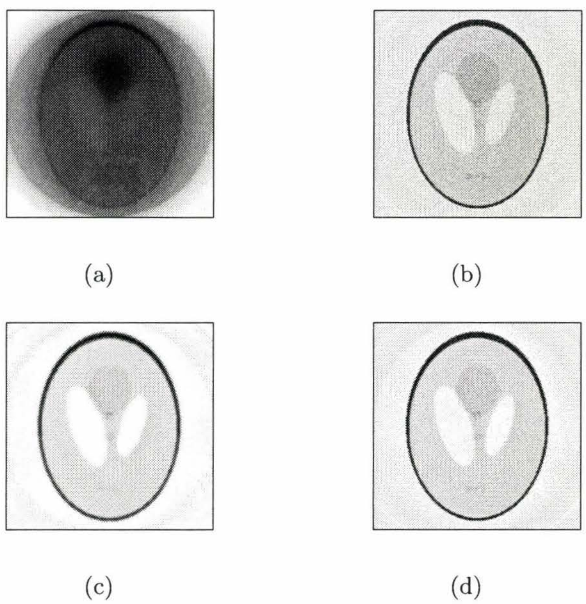

Figure 2.17: Filter back-projection simulation result of Shepp-Logan images. 25% Poisson noise is added into the projection images in Fig. 2.12(b). (a) is the simple back projection result. (b), (c) and (d) are the back projection results using Ramp filter, Hanning filter and Shepp-Logan filter, respectively.

FBP is easy to implement, however, it is difficult to do the correction for attenuation, scatter and other physical factors.

2.3.4 Iterative Reconstruction Methods

The primary advantage of analytical reconstruction methods is fast computation time. However, the reconstruction results show significant inaccuracies because more complex effects such as photon scattering and collimator-detector response are not easy to remove with these methods. Iterative methods are thus introduced that have the ability to more accurately account for these effects. Iterative methods usually start with a uniform object and make several successive iterations to estimate the resultant image by reconstructing the difference between the recorded projections and the forward projections of the estimated object. At each iteration, forward projection provides the estimated projections, which is then compared with the actual measured projections. The difference between the estimated and actual projections is then used to update the estimated object. This process is repeated until the difference between the estimated projections and the actual recorded projections fall below a specified level. The two most important key points of the iterative reconstruction method are: 1) the difference function and 2) the updating function.

The iterative method starts with an initial arbitrary estimate and projects this estimate into projections analogous to those measured by the camera. At this step, physical factors such as attenuation, scatter, and depth-dependent collimator resolution can be included. The projections of the estimated object are then compared with the measured projections by subtracting or dividing the corresponding projections in order to obtain correction factors. If the error factors are below a certain level and do not change in subsequent iterations, or if the maximum number of iterations is achieved, the procedure stops, otherwise, the error factors, in the form of differences or quotients, are back-projected to update the new estimate of the object. With iterative methods, quantitative estimation is possible, because iterative reconstruction compares the values of the estimated images with the actual images which reflect the real activity.

In the radionuclide imaging system, photons are emitted and detected by an external detector. In the mathematical description, the radionuclide image, f, is represented as 1D colomn vector, but in fact it might be a 2D or even 3D matrix in which each point value denotes the radionuclide concentration at this point. Similarly, the recorded radionuclide projection data, p, is also written as a column vector, but it generally is reshaped from a 2D or 3D matrix, where each matrix element, p_i, identifies the number of photon counts collected by a certain detector bin at a given rotation angle.

The probability that a photon emitted from the j^{th} voxel and detected in the i^{th} detector bin can be written as a_{ij}, which includes the factors of the imaging phenomena. Therefore, we can express the behavior of the imaging system using the matrix A coupling with the radionuclide concentration f in the object to simulate the detector measurement:

$$p = Af \tag{2.13}$$

where, p is the recorded radionuclide projection value, A denotes the acquisition process, and f is the voxel value of the radionuclide image.

Ideally, the unknown radionuclide concentration matrix f can be derived mathematically from Eq. 2.13. However, it is impossible to take this direct approach because of several factors.

- The matrix size of A is immense. A typical nuclear medicine study requires at least 60 projection images over 180°. When each projection image is recorded in a 64×64 matrix format, the total number of measured elements in matrix p is $64 \times 64 \times 60 = 245,760$, with the value of each element denoting the number of counts collected by the corresponding detector bin at the specific angular projection. Suppose the size of radionuclide concentration matrix f is $64 \times 64 \times 64 = 262,144$. Therefore, the size of probability matrix A has 262,144 columns and 245,760 rows, or over 64 billion matrix elements. It is impossible to perform any mathematical calculation with so large a matrix.

- In nuclear medicine, the projection images are acquired with a highly collimated detector. The recorded photons at a certain angular position and specific detector bin are emitted from only a few radioactive points but not all the points in the object. It is apparent that the probability matrix A is very sparse and nearly singular.

- The generated projection value p, is noisy and may not be known exactly because of the uncertainty of the photon behavior. Therefore, Eq. 2.13 may not be solved uniquely for different measurements with the same acquisition parameters.

Fortunately, there are a lot of methods used to solve for the radionuclide concentration. One of the most well-known approaches is the maximum likelihood expectation-maximization iterative reconstruction algorithm (ML-EM). Although f in Eq. 2.13 is an unknown factor, we can assume a solution which is the estimate of the true radionuclide distribution. The projection image value p is acquired from vector f, and the probability matrix A, is estimated. Matrix A is normally performed by a series of acquisition routines, which can be simulated by Monte Carlo code.

The measured counts in the SPECT detector are Poisson-distributed. ML-EM is based upon the assumption of the Poisson model random nature of radioactive decay [30]. The iterative update equation of ML-EM method can be written as:

$$f_j^{new} = \frac{f_j^{old}}{\sum_i a_{ij}} \sum_i a_{ij} \frac{p_i}{\sum_k a_{ik} f_k^{old}} \tag{2.14}$$

where, f_j^{new} is the updated voxel value, f_j^{old} is the old voxel value. The flow chart of ML-EM method can be seen in Fig. 2.18.

Fig. 2.19(a) shows the reconstruction result using Shepp-Logan phantom using ML-EM by taking 100 iterations. It can be seen that the blurring artifact is greatly reduced using the iterative method. Fig. 2.20 shows the reconstruction result of the Shepp-Logan projection sinogram with different iteration numbers when 25% noise is added into Fig. 2.12(b). Analytical forward projection using a perfect parallel hole

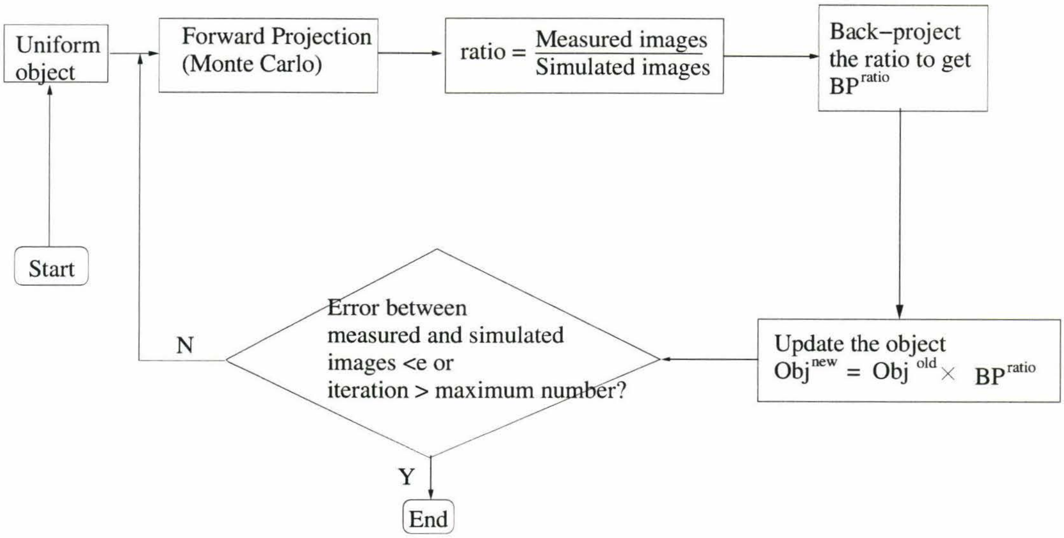

Figure 2.18: The flow chart of ML-EM reconstruction.

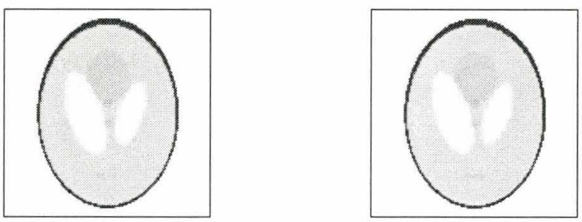

(a) (b)

Figure 2.19: The reconstruction result using ML-EM and OS-EM methods. (a) is the result taking 100 iterations using ML-EM algorithm, and (b) is the result taking 10 iterations using OS-EM algorithm.

collimator is applied in ML-EM reconstruction. The four resultant images shown in Fig. 2.20 used 2, 10, 50, and 100 iterations, respectively. The blurring artifact is reduced when the number of iterations is increased. However, the noise of the resultant images is also increased when the iteration number increases. Therefore, the noise level of the reconstructed images might be increased using iterative methods when the iteration number increases.

ML-EM uses successive estimation of the radionuclide distribution to converge towards the most likely distribution. It is able to provide very accurate reconstruction results, however, its application is limited by convergence speed. It takes

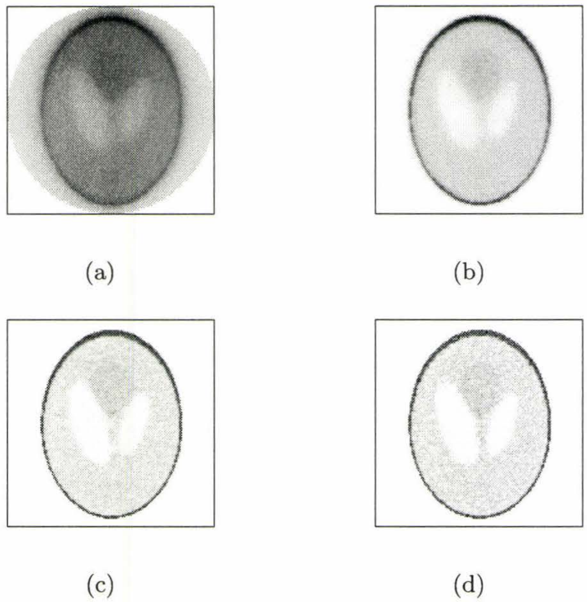

Figure 2.20: The ML-EM reconstruction result with 2 iterations (a), 10 iterations (b), 50 iterations (c), and 100 iterations (d). 25% noise is added in the initial noise-free projection image in Fig. 2.12(b).

about 1 hour to complete 100 iterations for Fig. 2.20(d) when 180 images are projected. A useful acceleration technique, ordered subset expectation maximization (OS-EM) [31], is applied in this study to generate the reconstructed images. In OS-EM, one iteration is divided into several sub-iterations. Only a subset of projections (i.e. four projections) are used at each sub-iteration for updating the estimated image, compared to all the projections in ML-EM. The updated equation of OS-EM is given by:

$$f_j^{new} = \frac{f_j^{old}}{\sum_{i \in S_n} a_{ij}} \sum_{i \in S_n} a_{ij} \frac{p_i}{\sum_k a_{ik} f_k^{old}} \tag{2.15}$$

where, S_n denotes the n^{th} subset. OS-EM yields similar results to ML-EM, as shown in Fig. 2.19(b), but with a significant speed improvement (10 OS-EM iterations vs 100 ML-EM iterations). The processing time of each iteration in OS-EM is similar to each iteration in ML-EM, but the convergence speed of OS-EM is much faster than ML-EM. Therefore, OS-EM roughly increases the speed about n times, where n is the number of subsets.

In Lalush's and Tsui's work [32], it is mentioned that the number of iterations decreases when the number of views per subset decreases. However, the price for the increased speed is an increase in reconstructed image noise because of the bias brought out in each sub-iteration. There is always a tradeoff between the number of angles per subset and the increased speed. It is suggested in their work that at least 4 angles per subset be used in order to avoid significant increases in image noise. In clinical practice, using the fewest subsets in one iteration is preferred to get the best result if the processing time is available.

2.4 Radionuclide Therapy

In radionuclide therapy, patients are given an injection of a radionuclide labeled targeting drug (radiopharmaceutical). The targeting drug locates a tumor, for example, as cancer cells take up much more of the substance than healthy tissues. Radionuclide therapy arises from the tissue absorption of β particles. β particles have very short traveling range (millimeters) in the human body. When the targeting drug labeled with a β-emitting radionuclide concentrates in tumor cells, the emitted β particles deposit a large amount of energy locally thereby killing the cells. An example of radionuclide therapy is the treatment of thyroid cancer. In clinics, radioactive iodine (e.g. ^{131}I), which is absorbed by thyroid tissue, is administered to kill cancer cells.

The key point of radionuclide therapy is the estimation of the optimal radionuclide activity. Accurate estimation is affected by several image degradation factors, which affect the quality of projection images. Optimal radionuclide activity should be estimated in order to avoid too high or too low of an absorbed doese for the best treatment. Nuclear imaging techniques are used to study the structure and the function of the organs of interest. Tomographic reconstructed images are used to visualize the three dimensions of the radio-tracer distribution, and determine the optimal therapeutic radionuclide activity to be introduced into the patient.

2.4.1 Image Degradation Factors

The quality of SPECT projection images is mainly affected by three principal factors: photon scatter, attenuation and collimator-detector response. They will further affect the accuracy of the reconstruction result and the activity estimation.

γ photons may interact with the surrounding materials, and result in the change of photon direction or the loss of photon energy. In nuclear medicine, there are four interaction types that a photon might undergo: Compton scattering, Rayleigh scattering, Photoelectric Effect and Pair Production, as shown in Fig. 2.21.

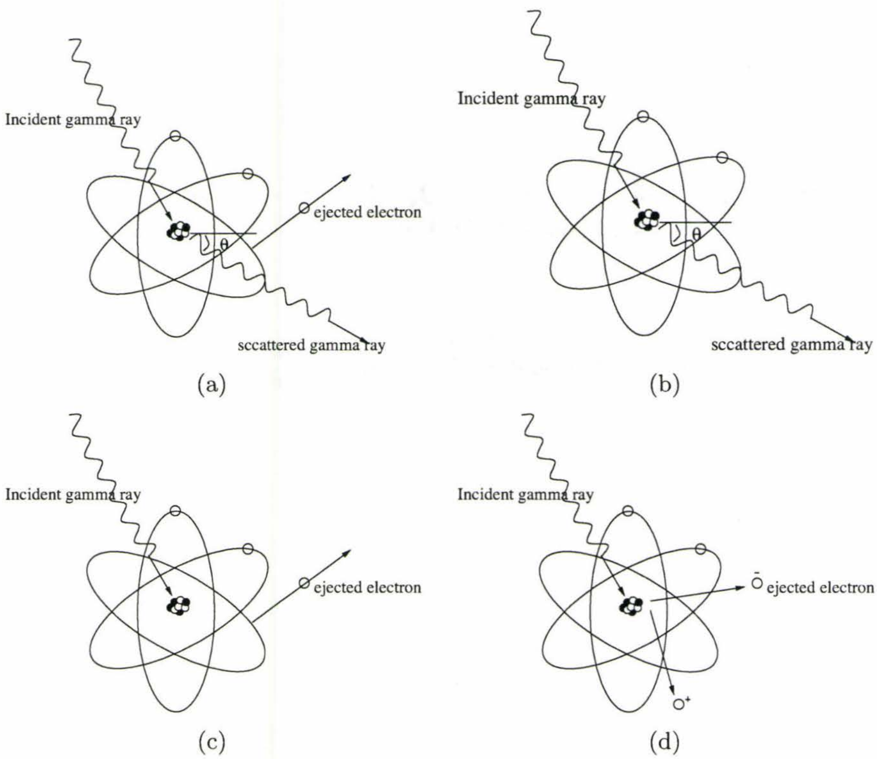

Figure 2.21: Four possible photon interaction types in nuclear medicine: a) Compton Scattering; (b) Rayleigh Scattering; (c) Photoelectric Effect; (d) Pair Production.

Compton scattering is the predominant photon interaction type with soft tissue for radionuclides used in nuclear medicine (80-250 keV). When a γ ray interacts with an electron in matter, the electron is ejected from its orbit, and the γ ray will travel through the material along an altered path with a reduced energy because of the energy carried by the ejected electron (Compton electron). Compton scattering most likely occurs between photons and outer shell electrons. The probability of Compton scattering is proportional to the material density and inversely proportional to the photon energy, but it is independent of the mass number of the material.

Rayleigh scattering is a type of interaction between a photon and an atom. Because of the mass of the atom, elastic scattering occurs when a photon hits the atom. The photon traveling direction changes but with little change in photon energy. Most Rayleigh scattering occurs at low energy (usually less than 50 keV).

Photoelectric Effect is an interaction in which photons are absorbed by the atom, with a subsequent ejection of an electron.

In Pair Production, a photon is absorbed and the energy is transferred to a positron/electron pair. Each particle has a rest mass equivalent to 511 keV energy. Therefore, the minimum energy of the incident photon will be 2×511 keV $= 1022$ keV.

Photon attenuation is the overall probability that a photon will be absorbed by the object or scattered out of the field of view (FOV) and missed by the detector. The probability of photon attenuation depends on the photon energy, the type of material and the thickness of the material that the photons travel through. The effect of attenuation is a reduction in the intensity of the incident flux:

$$I = I_0 \times e^{-\mu_l l} \tag{2.16}$$

where, μ_l is the linear attenuation coefficient in the unit of cm^{-1}, l is the thickness of the material. μ_l is a parameter that depends on the energy of incident photon, the atomic number Z of the absorbing material, and the density of this material. μ_l varies linearly with the material density ρ. In practice, the mass attenuation coefficient, which is independent of the material density, is used. Mass attenuation coefficient μ_m is equal to $\frac{\mu_l}{\rho}$, and can be further broken into four components according to different scattering type:

$$\mu_m = \sigma_{incoh} + \sigma_{coh} + \tau + \kappa \tag{2.17}$$

where σ_{incoh} is the probability of Compton Scattering, σ_{coh} is Rayleigh scattering, τ is from Photoelectric Effect, and κ is due to Pair Production.

Previous attenuation compensation has been performed via either filtering methods or iterative methods using an attenuation map typically acquired using a transmission CT techniques [33–36].

Scatter compensation can be divided into two categories. The first one performs correction on the projection images by calculating the fraction of the scattering photons based on a specific scatter model and removes these from the projection data prior to reconstruction [37–39]. It uses multiple energy windows to estimate the scatter photon fraction [40–42]. As shown in Fig. 2.22 [37], classic examples of this category are Compton window substraction (CW) [43], dual photopeak energy window scatter correction (DPW) [38, 39] and triple energy window scatter compensation (TEW) methods [44]. Here, the very well used TEW method is introduced.

TEW compensation, uses two narrow energy windows adjacent to the primary energy window in order to determine the scattered photon contribution within the photopeak. Three energy windows, W_2, W_{3+4}, and W_5 are selected, as shown in Fig. 2.22. W_2 and W_5 are located on each side of the photopeak window. The width of these three windows are denoted as l_2, l_{3+4}, and l_5, respectively. It is assumed that W_2 and W_5 are comprised only of scatter photons. Based upon the calculation of polygon area, the scatter contribution within W_{3+4} can be obtained by:

$$S_i = \left(\frac{P_{2,i}}{l_2} + \frac{P_{5,i}}{l_5}\right) \cdot \frac{l_3 + l_4}{2} \tag{2.18}$$

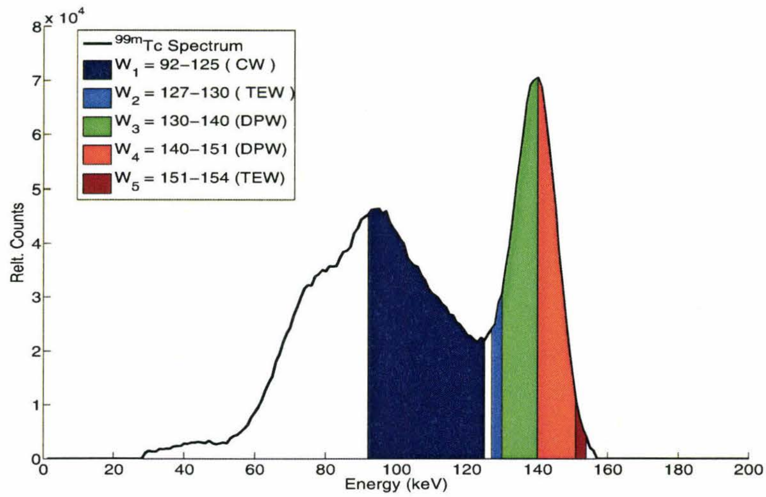

Figure 2.22: Energy spectrum of ^{99m}Tc. There are five energy windows indicated in the spectrum which are used in the scatter compensation. W_1 is used in CW, W_3 and W_4 are used in DPW, and W_2 - W_5 are used in TW.

where P_i is the number of counts collected in the i^{th} pixel of the photopeak, and and S_i is the number of scattering photons.

The updating function in Eq. 2.14 can be written as scatter subtraction function:

$$f_j^{new} = \frac{f_j^{old}}{\sum_i a_{ij}} \sum_i a_{ij} \frac{p_i - S_i}{\sum_k a_{ik} f_k^{old}} \tag{2.19}$$

or scatter modeling function:

$$f_j^{new} = \frac{f_j^{old}}{\sum_i a_{ij}} \sum_i a_{ij} \frac{p_i}{\sum_k a_{ik} f_k^{old} + S_i} \tag{2.20}$$

where the scatter photons are extracted from the real projection images.

CW uses scattering windows W_1 and $W_3 + W_4$, and DPW use windows W_3 and W_4, as shown in Fig. 2.22. For more detail, please refer to references [38, 39, 43].

Another scatter compensation approach models the scatter photons in the observed object during the reconstruction process, examples of which include Monte Carlo simulation or effective scatter source estimation (ESSE) [45]. These methods are typically more accurate than the first category, but their applications are limited by their complexity and required computation speed.

Collimator response (CR) is spatially invariant, but distance dependent. Some restoration filters, such as Metz or Wiener filters, are used in FBP to suppress the effect of collimator response [46–48], however, since CR is a distance varying function, applying either Metz or Wiener filter is not able to accurately account for all the source-detector distances. Other analytical methods have tried to model both shape and distance dependent filters, however, these methods as well are less than ideal [49, 50].

2.4.2 Time Activity Curves

In conventional SPECT imaging, the spatial distribution of the radiopharmaceutical is assumed to be constant. However, the metabolism of the human body will result in change in the radioactivity distribution as a function of time. Dynamic studies of radiotracer uptake and washout are required to evaluate the effect of different radionuclides. Dynamic imaging measures temporal changes in the spatial distribution of the radioisotopes in the body based upon the basic function of the organ to be examined. This is done by taking multiple images over periods of time which may vary from milliseconds to hours. The dynamic imaging projection images are reconstructed by a specific dynamic reconstruction code and the time activity curves (TAC's) for different organs are estimated. TAC's are also used to determine the organ accumulated dose and the effect of dose rate. When large quantities of radioactivity are administered to patients, healthy cells may be damaged and may not have enough time to repair. As a result, it is important to measure the amount of radioactive build-up of the human body to make sure the uptake rate is safe yet effective to the patient.

2.5 Conclusion

Radionuclide therapy is very important in clinical practice. A primary problem in radionuclide therapy is the determination of accurate quantitative estimates of radioactive distributions. Nuclear imaging, such as SPECT, is used to acquire the projection images at different angular views and is used to estimate the radiotracer concentration. This chapter has introduced the radioisotopes used in different types of nuclear imaging and image reconstruction techniques to recover the radioactivity distribution. Several methods for image degradation compensation are discussed. In the next chapter, we will introduce an accurate simulation tool - Monte Carlo, which is used to model photon transport in order to more accurately obtain 3D radiotracer quantitation.

Chapter 3

Monte Carlo in Nuclear Medicine

Monte Carlo (MC) is a statistical method that uses random numbers to perform a simulation of the nuclear imaging process. MC methods provide a way to simulate the path of emitted photons through an object, accounting for photon interactions such as scattering and absorption. The underlying process describes the photon transport as a set of probability distributions based upon the step size of photon movement, photon interaction types, and the deflected trajectory when photon scatter occurs. By knowing the physical process based upon accurately defined probability density functions (PDF's), MC is able to simulate the transport of a photon from the point of emission to the point of detection.

Why is MC modeling so important in nuclear medicine imaging simulation? MC makes it possible to test individual parameters of the detector system by changing values such as phantom size, collimator hole shape and crystal type. In the development of a new detector system, MC provides an effective way to test the characteristics of individual components without the expense and complex task of manufacturing. For economic and safety consideration, real experiments may not be possible to perform due to difficulties with transport or storage of radionuclides or because of the radiation dose absorbed by the patient. However, it is possible to perform a simulation using MC in order to model any arbitrary geometry or situation. Another reason why MC is useful is that it enables one to be able to study factors that are not measurable in practice. One example is in the calculation of the exact number of scattered photons in a study. In MC, it is relatively simple to turn off/on some effects such as photon attenuation, scatter or collimator septal penetration.

3.1 Random Number Generation

MC calculation is based upon a large amount of random number sampling, which is obtained by a random data generator. Therefore, the ability to generate random data is a fundamental requirement of MC simulation. A random number generator is a computer algorithm which can produce a set of uniformly distributed random numbers. These random numbers are used as seed values in the MC calculations. One of the best-known pseudo-random number generator algorithms is called linear congruential generator (LCG) which is defined by the recurrence relation:

$$SEED = (aInt(SEED) + c)\, mod(m) \tag{3.1}$$

where, $SEED$ is the sequence of random values, a and c are constants, and m is the integer constant which specifies the generator. In order to set the random number in the range of [0, 1], $SEED$ is normalized by m: $RAND = SEED/m$. The same initial $SEED$ values produce the same set of random number sequence, hence this is known as pseudo-random numbers, however, there is a very low probability that the value of the initial seed might appear in the resulting sequence, thus resulting in a loop sequence. LCG is a very fast random number generator, however, the generated random numbers may not be perfectly independent of each other. There are some other random generators, which can be referred to reference [51]. In this thesis, we used the generator present in the Lahey Fortran compiler.

3.2 Data Sampling In Photon Interaction Simulation

In MC simulation of SPECT, different parameters in photon interactions (i.e., photon scattering type, photon traveling path length, traveling directions and cross-sections) that occur during transport should be sampled from the probability density functions (PDF's) based upon the physical characteristics of photons and the gamma camera. The simulation includes the initiation of a photon event, the cross-section generation, photon pathlength and interaction sampling, which, together with the stochastic variable sampling methods, will be discussed in more detail.

3.2.1 Photon Path Length

When a photon is emitted from its initial location, it will travel a certain distance before interacting with the material. The traveled distance depends upon the photon energy and the material properties. Generally, the higher the photon energy and the lower the material density, the greater the traveled distance. The path length x, can be sampled from the photon pathlength probability function in reference [52]:

$$p(x) = \mu exp(-\mu x) \tag{3.2}$$

where, μ is the linear attenuation coefficient in the material. The probability that a photon is able to travel a distance d, is obtained from the cumulative distribution function, which ranges from [0,1]:

$$P(d) = \int_0^d \mu exp(-\mu x)dx = 1 - exp(-\mu d) \tag{3.3}$$

In order to determine the traveled path length d, a random number R is sampled:

$$d = -\frac{1}{\mu} ln(1 - R) \tag{3.4}$$

Because R is at the range of $[0, 1]$, so is $1 - R$, therefore, Eq. 3.4 can also be written as:

$$d = -\frac{1}{\mu} ln(R) \tag{3.5}$$

3.2.2 Cross-Section Data Generator

A photon interacting in matter at nuclear medicine energies may undergo Compton scattering, Rayleigh scattering, Photoelectric Absorption or Pair Production. Each of these possible interactions has a finite probability of occurring and the probability is designated as the cross-section. As discussed in Chapter 2, the total probability of a photon undergoing one of these processes is called attenuation and is the sum of each individual probability. The photon attenuation coefficient is then calculated based upon the total cross section.

In Monte Carlo modeling, the cross section of each individual photon scatter and the attenuation coefficient is determined using a specific computer code called XCOM [53]. This code produces cross section tables related to different elements, photon scattering and photon energies. The generated cross section tables are then incorporated into the simulation at each photon traveling step to calculate the photon transport weight.

3.2.3 Photon Interaction Type

As seen in Eq. 2.17, the photon attenuation coefficient is composed of four separate components. Assuming a photon scatters during the transit, MC code then generates a random number, R, in the range [0,1] to determine which type of interaction the photon undergoes based upon the following rules:

$$\text{photon scattering type is} \begin{cases} \text{Photoelectric Effect} & R \leq \frac{\tau}{\mu} \\ \text{Compton Scattering} & \frac{\tau}{\mu} < R \leq \frac{(\tau+\sigma_{incoh})}{\mu} \\ \text{Rayleigh Scattering} & \frac{\tau+\sigma_{incoh}}{\mu} < R \leq \frac{\tau+\sigma_{incoh}+\sigma_{coh}}{\mu} \\ \text{Pair Production} & \frac{\tau+\sigma_{incoh}+\sigma_{coh}}{\mu} < R \leq \frac{\tau+\sigma_{incoh}+\sigma_{coh}+\kappa}{\mu} \end{cases} \tag{3.6}$$

where, the definitions of τ, σ_{incoh}, σ_{coh} and κ are the same as Eq. 2.17, and $\frac{\tau+\sigma_{incoh}+\sigma_{coh}+\kappa}{\mu}$ should be equal to 1. Note Pair Production occurs only when the incident photon energy is higher than 1.022 MeV. Because Rayleigh scattering is most likely to occur when the photon energy is lower than 50 keV, the predominant scattering type in SPECT is Compton scattering. For example, the probability of Rayleigh Scattering in the human body and crystal material is small (less than 1%) at the peak photon energy of 140 keV [54]. In practice, these models are often simplified to save computation time. In Monte Carlo simulation, only Compton Scattering and Photoelectrical Effect will be considered when photon energy is higher than 100 keV. Therefore, Eq. 3.6 can be simplified to:

$$\text{photon scattering type is} \begin{cases} \text{Photoelectric Effect} & R \leq \frac{\tau}{\mu} \\ \text{Compton Scattering} & \frac{\tau}{\mu} < R \leq \frac{(\tau+\sigma_{incoh})}{\mu} \end{cases} \tag{3.7}$$

where, $\frac{(\tau+\sigma_{incoh})}{\mu}$ is equal to 1. In the Monte Carlo simulation, the probability of Compton Scattering σ_{incoh} is sampled, resulting in the probability of Photoelectric Effect of $1 - \sigma_{incoh}$. If the photon is scattered, after the path length calculation, the new photon traveling direction is determined. The Klein-Nishina equation is used to calculate the cross-section:

$$d\sigma_{incoh} = \frac{r_e^2}{2}\left(\frac{E_{sc}}{E}\right)^2\left(\frac{E}{E_{sc}} + \frac{E_{sc}}{E} - \sin^2\theta\right)d\Omega \tag{3.8}$$

where, $d\sigma_{incoh}$ is the differential cross-section, which is equal to the probability R, r_e is the classical electron radius, E is the initial photon energy, θ is the scattered angle and E_{sc} is the scattered photon energy. E_{sc} can be calculated by:

$$E_{sc} = \frac{E}{1 + E(1 - \cos\theta)} \tag{3.9}$$

Because of difficulties combining Eq. 3.8 and Eq. 3.9 to derive the value of E_{sc} and angle θ. This model is connected to a sampling method for bounded electrons, which includes atomic effects. Kahn has introduced a method to sample the scattering angle [55]. In his method, the scattering angle is sampled and compared with a certain scattering function discussed in [56]. If the scattering angle is less than the value of the scattering function, the angle is accepted, otherwise, new sampling for the angle should be performed until an effective value is obtained. Once the scattered angle is determined, Eq. 3.8 and Eq. 3.9 are utilized to calculate the probability of Compton Scattering and the scattered energy.

Based upon the scattered angle, the new traveling direction of the photon can be calculated. Assuming the old polar and azimuthal angle of the photon traveling direction in the Cartesian coordinate system are θ_1 and ϕ_1, and the new angles are θ_2 and ϕ_2. The new direction cosines (u', v', w') are calculated from the old direction cosines by:

$$\begin{cases} u' = u\cos\theta_2 + \sin\theta_2(w\cos\phi_2\cos\phi_1 - \sin\phi_2 sin\phi_1) \\ v' = v\cos\theta_2 + \sin\theta_2(w\cos\phi_2\sin\phi_1 + \sin\phi_2 cos\phi_1) \\ w' = w\cos\theta_2 - \sin\theta_2(\sin\theta_1\cos\phi_2) \\ v = \sin\phi_2\sin\theta_1 \\ u = \sin\theta_1\cos\phi_1 \\ w = \cos\theta_1 \end{cases} \tag{3.10}$$

The new coordinates (x', y', z') are then calculated by the direction cosines and the traveling distance d:

$$\begin{cases} x' = x + du' \\ y' = y + dv' \\ z' = z + dw' \end{cases} \tag{3.11}$$

If the photon energy is lower than 100 keV, the consideration of Rayleigh Scattering should be included, however, the exact calculation of Rayleigh Scattering is very complicated and will not be discussed here, but rather detail of this modeling can be found in [52].

3.3 Detector Simulation

As mentioned in Chapter 1, the hardware of a detector system includes the collimator, crystal and other electronic components. Therefore, the simulation of each individual component is required for proper photon transport modeling.

Collimator

When a photon is emitted from the object and hits the collimator, its azimuthal and polar angles are compared with the collimator hole direction. If the angles match the collimator hole direction, the photon event is recorded, otherwise, the photon may interact with the collimator or undergo septal penetration. Some photons may scatter in the collimator and get detected, which is called collimator scatter. The probability function of the detected photons is the collimator response function, which is comprised of geometric response, collimator scatter, septal penetration (more detail will be discussed in the next Chapter), and collimator scatter. Geometric response will be modeled as a Gaussian function. However, septal penetration and collimator scatter is more difficult to describe mathematically, and has to be externally modeled at different photon energies for differing source-detector distances. This will be described later in more detail. It has been studied by Ljungberg. et, al. [57] that when ^{123}I point source is measured by low energy general purpose

(LEGP) collimator with the source-detector distances as 10-25 cm, the fractions of geometric photons, penetrated photons and scatter photons are about 62.8%-73.4%, 23.2%-17.4% and 14.0%-9.2%, when a low energy high resolution (LEHR) collimator is used, the fractions are about 49.2%-62.0%, 32.0%-25.0%, 18.8%-13.0%. In this thesis, the focus will be on the simulation of penetrated photons only.

Crystal

When the photon travels through the collimator and hits the crystal, an interaction between the photon and crystal is assumed to occur by sampling a random number within the probability of interaction (Photoelectric Effect). The resultant visible light with amount related to the photon energy is emitted.

Other Electric Components

Simulation of the rest of the electron components includes energy resolution simulation and temporal resolution simulation.

Energy resolution is the ability of the gamma camera to distinguish two photon energies. It is described by the full width at half maximum (FWHM), as seen from Fig. 3.1. When two photon energies are separated by less than FWHM, the system might not distinguish them and hence records the photon events as one input photon (Fig. 3.1). The energy resolution depends on: 1) crystal material, which affects the number of visible light photon emitted, 2) the collection and amplification ability of the detectors, 3) the signal processing ability of the other circuit. Box and Muller [58] have used a Gaussian function P to describe the energy resolution centered at energy E with a standard deviation (σ), which is a constant number given the parameter of the detector system and photon energy. $FWHM = 2.35\sigma$ is used to denote the energy resolution. In MC, two random numbers R_1, R_2 (within the range [-1,1]) are continuously sampled until they fulfill the criterion $R_3 = R_1^2 + R_2^2 < 1$, where, R_1 denotes the resolution due to crystal and R_2 denotes the resolution due to PMT,

R_3 is system resolution [59]. The value of P is then calculated by:

$$P = E + \sqrt{2\frac{ln\left(\frac{1}{R_3}\right)}{R_3}R_1} \cdot \sigma \tag{3.12}$$

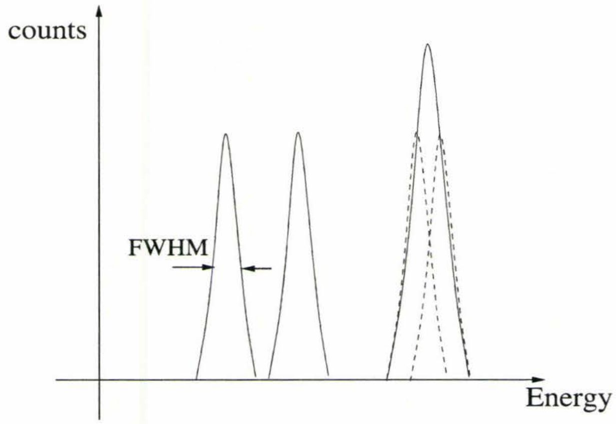

Figure 3.1: Energy spectrum configuration. The x-axis denotes the energy of the emitted photons, and y-axis is the relative number of collected photons. Energy resolution is denoted as the full width at the half maximum value. If two energy spectra are too close, they will appear to overlap [59].

The energy resolution for NaI(Tl) is around 10% at 140 keV. Fig. 3.2 shows the energy spectrum with ideal energy resolution and 10.5% resolution when ^{131}I emitted photons (primary photon energy: 364.5keV) are simulated from a phantom and detected by the gamma camera with HEGP collimator. Fig. 3.2(b) is seen when a Gaussian function is convolved with Fig. 3.2(a) [59].

Because of the decay time, T, of photon events detected, pulse pile-up might occur when two photons are detected within a very short time period. Temporal resolution is the ability of a gamma camera to distinguish two photon events in time. The time between two consecutive events is calculated by a random number R:

$$e^{-\frac{T}{TK}} = R^{\frac{1}{TK \cdot IA}} \tag{3.13}$$

where TK is the photon event decay constant and IA is the expected count rate

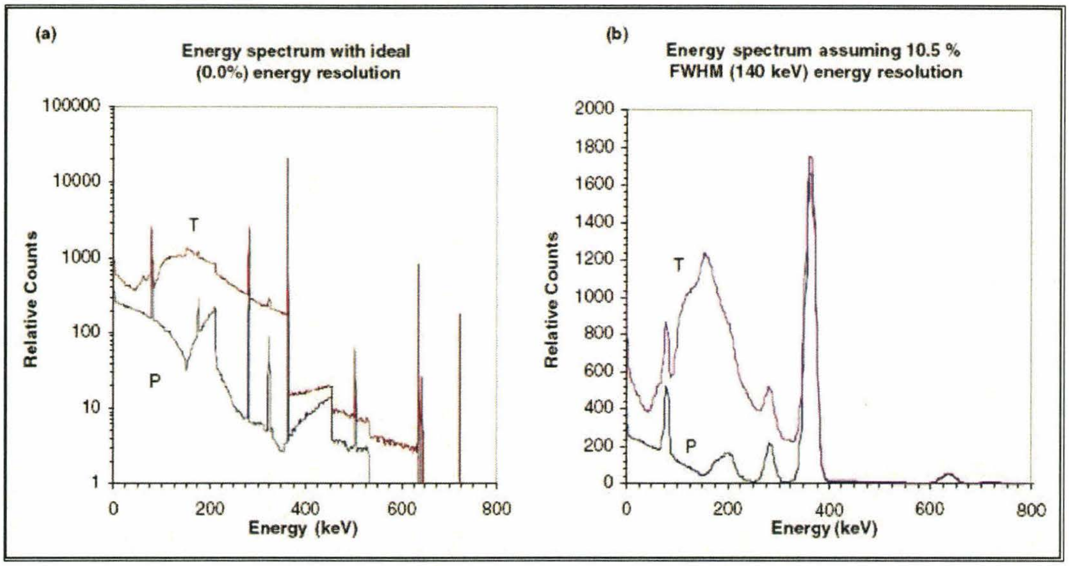

Figure 3.2: The energy spectra for ^{131}I with (a) ideal resolution when photon energy is imparted in the crystal, and b) 10.5% energy resolution [59]. T is total photon, and P is primary photon.

which denotes the ratio of the number of photons being detected to the number of incident photons. Two photon events are accepted only when the sample time is greater than the temporal resolution, otherwise, they are rejected.

3.4 Phantoms

Phantoms are pre-designed realistic or mathematical models of physical distributions and attenuation materials. They are used either for testing and training on the scanners or studying physical characteristic of human organs. Some models contain very simple geometric shapes, and some are made more complex in order to approximate real human anatomy. In this thesis, most of the phantoms used are mathematical phantoms. They are divided into two categories, analytical phantoms and digital (voxel-based) phantoms. Digital phantoms are primarily used in most

MC simulations. Simple phantom models may be composed of ellipsoids, cylinders, spheres, or rectangular volumes. The advantages of these phantoms are the simple structure and fast calculations of the simulation, but the phantoms are limited to simple geometries of the sources and constant value of attenuation medium. In order to better understand human imaging, more complicated models are developed for use in nuclear medicine. There are several very well known phantoms used in MC simulation: digital anthropomorphic phantom such as the Zubal phantom developed by Zubal and Harrell [60, 61], cardiac phantoms such as the mathematical cardiac torso (MCAT) phantom, Nurbs-based cardiac-torso (NCAT) phantom and mouse phantom (MOBY) developed by Tsui, Frey and Segars, et. al. [62–64].

3.4.1 Digital Anthropomorphic Phantom

A digital anthropomorphic phantom is based on realistic data, but with constant parameters such as phantom size. A very well known anthropomorphic phantom, the Zubal phantom is based on CT images of a healthy adult male, 177.8 cm tall and 68.2 kg in weight. The reconstructed CT images were segmented into organs. The phantom consists of 243 128×128 slices with the voxel size $= 4mm \times 4mm \times 4mm$. The free Zubal phantom data can be obtained at: *http://noodle.med.yale.edu/zubal.* Fig. 3.3 shows the lateral and anterior views of the Zubal phantom. The skin and internal bones have been highlighted in order to make the phantom more visible. The Zubal phantom is widely used in the assessment of brain, lungs, liver, thyroid, spleen, bone and whole body. Each organ is assigned a specific value, which denotes the relative activity concentration.

3.4.2 Cardiac Torso Phantom

Mathematical Cardiac Torso and Nurbs-based Cardiac Torso Phantoms

The mathematical cardiac torso phantom (MCAT) is a phantom used to simu-

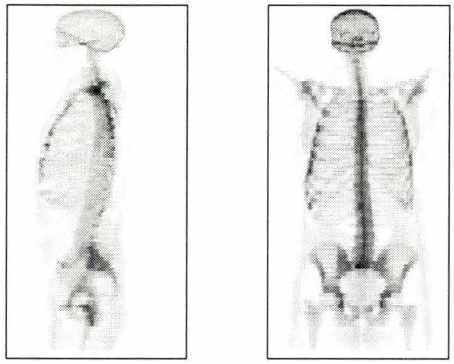

(a) (b)

Figure 3.3: Lateral and anterior views of the Zubal phantom. The skin and bones have been highlighted.

late the organs of a real human being and was initially developed to evaluate the accuracy of image reconstruction techniques for SPECT [65]. It is originally based upon the MIRD phantom developed by Snyder et al. [66]. The complex surfaces of different organs are formed using simple geometries with cut planes and intersections. The surfaces of the organs are defined continuously. Therefore, it is easy to model different organ sizes and shapes with varying spatial sampling. However, the simple organ geometries limit the modeling accuracy of anatomic problems. It has also been used to study the effects of anatomical variations in cardiac imaging and gated imaging [67, 68].

In order to model more accurate organ shapes, anatomical variations and patient motion, a 4D computer graphic technique called non-uniform rational B-splines (NURBS) is applied to the MCAT phantom to more accurately describe the 3D organ surfaces [62]. This NURBS-based cardiac torso phantom (NCAT) uses an actual human CT dataset as the basis of generated surfaces. It also contains a beating heart model and respiratory motion. Reconstruction images of a gated magnetic resonance imaging (MRI) cardiac scan are employed to generate the beating heart model, and a respiratory model is derived from respiratory physiology. The NCAT phantom is more realistic and flexible than the MCAT phantom due to the more realistic organ surfaces.

Digital Mouse Phantom

The digital mouse whole body phantom (MOBY) is modeled similarly to the NCAT phantom but is based on a cardiac-gated and respiratory-gated MRI dataset of a healthy mouse. 3D NURBS technique is also used to define the 3D organ surfaces [64]. The MOBY phantom has been used in SPECT and X-ray computed tomography (CT) simulation.

MCAT, NCAT, and MOBY phantom data are most likely used in cardiology imaging simulation, or in organ studies such as: liver, lung and kidney. Just as for the Zubal phantom, each organ of the Cardiac Torso Phantoms is also assigned a specific value for more flexible application. They are widely used in dynamic SPECT simulation and gated imaging simulation. The data can be acquired at:

http://www.bme.unc.edu/~wsegars/phantom.html

3.5 Frequently Used Monte Carlo Codes

There are several MC codes used in nuclear medicine. In the general domain, the well known, general-purpose MC codes include: i) electron gamma shower (EGS), ii) electron transport (ETRAN), iii) integrated tiger series (ITS), iv) Monte Carlo N-particle transport (MCNP) and vi) geometry and tracking (GEANT).

The EGS computer code system is a general purpose package for the simulation of the coupled transport of electrons and photons in an arbitrary geometry. The range of the particle energies is from a few keV up to several TeV. It is written in the computer language MORTRAN, which is a forerunner of FORTRAN. EGS does not include its own definition of the phantom geometry and parameters, and therefore, the operation has to be linked with external code that describes the phantom geometry and parameters. The application of EGS is also limited by its computer language. Although it is very flexible and powerful, it requires good computational skills of the users.

ETRAN is a MC code used in electron and photon (energy range: 1keV to 1 GeV) transport simulation [69]. This code is written in FORTRAN computer language. It is able to handle primary sources of electrons and photons, however, it still does not include geometric object information except for some simple phantoms such as a cylinder. The few geometry options keep ETRAN from wide application. It is useful in the investigation of specific interactions. Therefore, ETRAN can be used as a standard for the development of more general codes and has been included in ITS and MCNP.

ITS is a linear time-integrated coupled electron/photon radiation transport simulation written in FORTRAN. It is a powerful MC simulation code with a user-friendly software package. ITS has its own geometry package, which increases the convenience to the user. ITS can be used relatively straightforwardly and no further programming experience is required.

MCNP has capabilities to simulate almost all particles and is written in FORTRAN language. It uses a built-in random number generator but is not dependent on the computer on which it runs. MCNP utilizes external cross section libraries and physics models for particle types and energies where tabular data are not available. The photon energy ranges from 1 keV to 1000 keV in this simulation code [70]. The interaction types include coherent scatter, incoherent scattering, and Photoelectric Effect. MCNP has the potential to simulate high energy photons and could be widely used in SPECT imaging.

GEANT is written in both FORTRAN and C computer language and used to simulate particle transportation. GEANT has capabilities to easily handle complex geometries. It offers a broad selection of physics models. GEANT is very powerful and flexible, but it is also very complex. As a single simulation might take a few days, GEANT is very difficult to use.

There are three types of specific MC softwares used in nuclear imaging simulation: SPECT dedicated MC, PET dedicated MC, and MC used in both. The SPECT dedicated MC includes SIMIND (FORTRAN), simulation system for SPECT (SIMSPECT, FORTRAN and C), MCMATV (FORTRAN). The PET dedicated MC includes simulation system for PET (SIMPET, FORTRAN), and EIDOLON (C). The MC codes used in both include simulation system for emission tomography (SIMSET, C) and general architecture for text engineering (GATE, C), which is based on GEANT.

Whether to use a general purpose or a dedicated code depends on the user's needs and abilities. A dedicated code does not usually require strong programming skill in order to use, however users will be limited to certain capabilities. On the other hand, using a general purpose MC code makes it possible to study original configurations (i.e. new detector designs), as general purpose codes include more flexibility but also more complexity.

All MC codes used in nuclear medicine share some common components, such as the random number generator, the estimation of the probability density function, and probability density function sampling techniques. Rather than these common features, MC codes differ in their accuracy, flexibility, efficiency, and ease of use.

The accuracy of the MC code is related to:

- The way in which the particle interactions are simulated and the types of interactions that are simulated.
- The components simulated and how those components are modeled.

Photoelectric and Compton scattering are two kinds of photon interactions that are always modeled in MC simulation. Other photon interactions, such as Rayleigh scattering, might be neglected as it usually takes place when the photon energy is lower than 50 keV. However, the study of Zaidi, et. al. [71] has illustrated the relative strengths of photon interactions versus energy for low-Z material (e.g., water) and high-Z material (e.g., bismuth germanate). The contribution due to Rayleigh Scattering is less than 1% for energies above 250 keV, whereas this contribution is about 7% for high-Z materials. Therefore, in PET or some high energy photon detection (e.g., ^{131}I) in SPECT, Rayleigh Scattering has to be accounted for in the simulation. It is expected that all kinds of photon interactions within the detector system need to be simulated. ^{99m}Tc is the most commonly used radionuclide.

In SPECT, the application of the collimator greatly reduces the detection efficiency. Therefore, geometric response is often analytically simulated, and other less significant collimator response such as septal penetration and collimator scatter are usually neglected. This neglect leads to significant error when high energy photons (e.g., I^{131}) are used because of penetrating photons. The detector spatial resolution is usually modeled analytically using an effective probability density function, rather than by simulating the impact of the crystal, light guide and photomultiplier tube. When high energy photons are incident, however, back-scattering might occur which requires further simulation.

The flexibility of MC depends on how many of the following features a MC code includes:

- Source distributions.
- Detectors.
- Acquisition configurations.
- Output data.

As we have discussed previously, the source and attenuation distribution used in MC are based upon either analytical or voxel representations. Although both analytical and voxel-based phantoms are becoming more and more sophisticated and can include very realistic attenuating media, more accurate knowledge of the physiological distribution of different radionuclides due to differing photon energies is still needed.

In SPECT, the most common detector is the planar camera, while in PET, scanners are full-ring detectors. Generally, the MC codes should have the ability to simulate a number of detectors, geometrical shapes, size, or other physical characteristics. Moreover, these codes should also be able to model most commonly used detector materials such as BGO, NaI and LSO. In general purpose codes, these crystal materials are simulated based on the physical and chemical compositions of the material.

The more flexible MC codes are able to acquire 2D projection images of 2D or 3D objects of arbitrary size. When these acquisition processes are dependent on a specific SPECT and PET scanner, dedicated MC codes are required.

The efficiency of MC code depends on the ratio of the number of detected photons to the number of simulated photons. In practice, the efficiency of MC is very low (only about 1 out of 10,000 photons emitted is detected in SPECT simulations [59]). In an effort to improve the detection efficiency, analytical models have been generated externally to avoid unnecessary MC simulation. Variance reduction techniques are applied to incorporate these models into MC, but at the expense that some photon effects are neglected in different cases. Chapter 3 will discuss some of these variance reduction techniques in more detail.

In this thesis work, the SIMIND MC program has been used as it is able to accurately simulate the photon transport through different attenuation media and the detector systems for SPECT imaging. Different types of phantoms are very easy to use in SIMIND. Simulation results include projection views, energy spectra, and scattered photon fraction. SIMIND is written in FORTRAN language, easy to run in Linux system, and is able to be incorporated with other programming codes easily.

3.6 The SIMIND Monte Carlo Program

The SIMIND Monte Carlo program uses a series of random numbers to simulate the various photon events. Photons are emitted from their initial locations within the object and are followed step by step until they reach the gamma camera and are detected.

The flow chart of SIMIND can be seen in Fig. 3.4. When a photon is emitted from its initial location, the photon history weight is set as 1. The attenuation map is used to determine whether the emitted photon is a primary photon. If it is a primary photon, the photon is directed to the detector in order to increase the simulation efficiency. Its detected location on the detector is sampled based upon the detector spatial resolution, then the traveling direction is determined. The photon weight is still 1 before it hits the detector because no attenuation exists along its traveling path. The simulation of a detector system is then performed to calculate the final photon history weight.

If the photon is traveling in an attenuating media, the maximum scattering order is determined. When the photon scattering order is less than the maximum number, a sampling of photon scattering continues. In each sampling, the new photon transport pathlength is sampled first followed by the photon location, the probability of scattering, the new scattered energy and the new traveling direction, as referred in Eq. 3.5, Eq. 3.8, Eq. 3.9 and Eq. 3.10, respectively. The new photon traveling weight is updated by multiplying the old weight with the probability. The sampling is repeated until the photon is outside of the object or the maximum order of scattering is reached. SIMIND always tries to force the photon to the detector at the final scattering location (or primary photon at the initial location), thus greatly improving the detection efficiency.

When the photon hits the detector, the interactions with the collimator, crystal and other components are determined and the probability of these interactions cal-

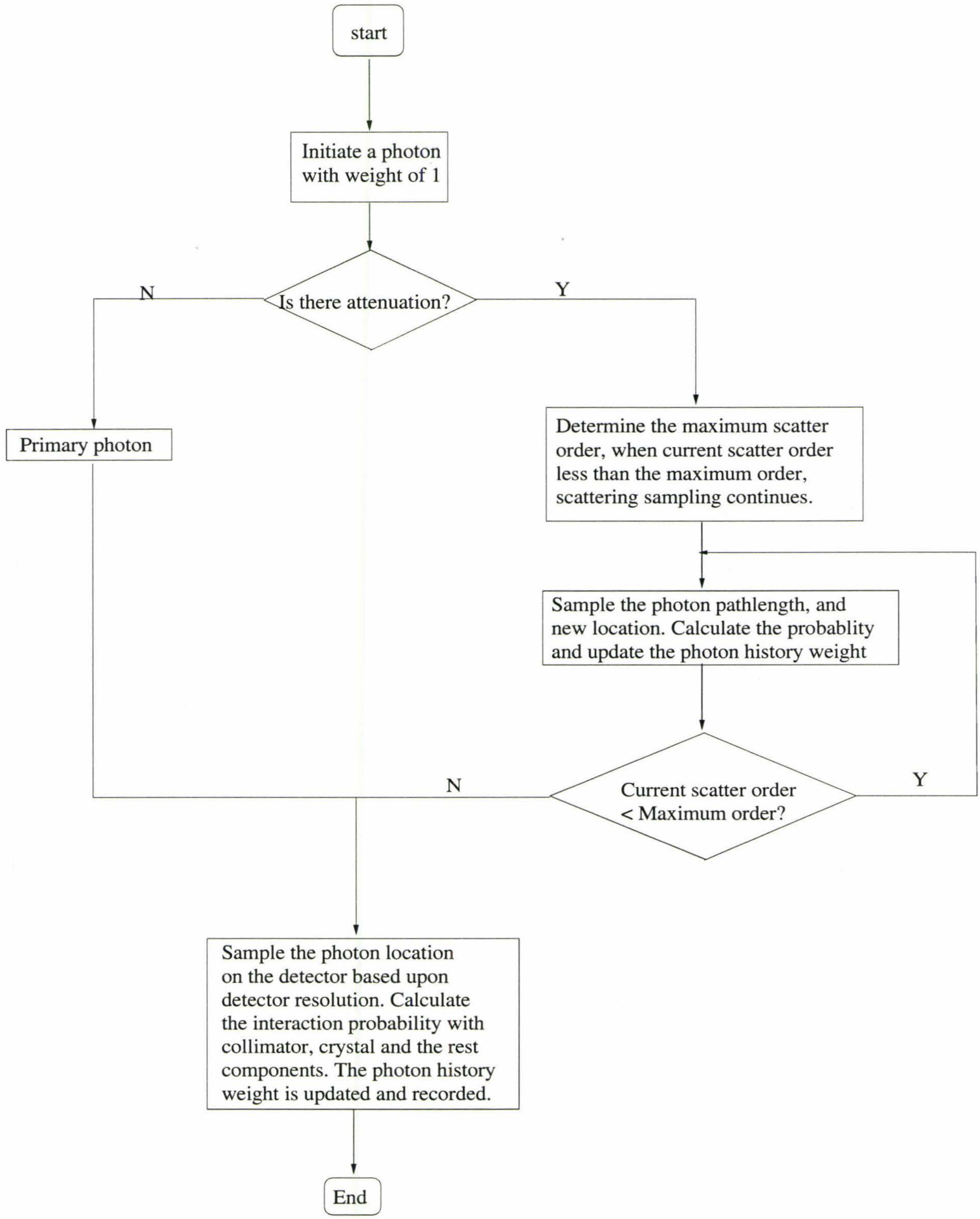

Figure 3.4: The flow chart of SIMIND program.

culated. The final photon weight is recorded at the corresponding location in the projection image.

Source Map and Density Map

In SIMIND, an activity source map and an object density map must be provided that represent the radiopharmaceutical distribution and the tissue density, respectively. The voxel value of the source map is the relative radioisotope concentration in each voxel and the total activity amount is determined by the source activity with the unit of MBq.

Because the linear attenuation value is a function of photon energy and material density, SIMIND uses a density map for modeling photon interactions. The linear attenuation value is the product of the mass attenuation coefficient and density map. The mass attenuation coefficient is a constant in spite of material state for a given photon energy.

Main Program

There are two main executable programs in SIMIND, one is **change**, and the other one is **simind**. The **change** program is used to define system parameters, such as the primary energy of the initial emitted photons, the matrix size of the object, the starting camera rotation angle, and so on. Different parameters to define the specific geometry and simulation are produced in a *.smc file that is used to run SIMIND.

The **simind** command is then used to run the MC code by reading the input files and simulating the photon transport. The operation of **simind** is:

simind parameter.smc output flags

where, parameter.smc defines the activity source, attenuation source and all the simulation parameters. Output is the name of the resultant output files. The output files include projection data (output.dat), photon spectrum (output.spe) and other data of interest. Flags denote the primary parameters used in the simulation. For example,

simind ge.smc output/px:0.442/41:0

where, ge.smc includes the information of all input files and parameters. /px:0.442 denotes the pixel size = 0.442 cm, and 41 denotes the 41^{st} parameter in the *.smc file, which defines the starting angle of the acquisition. /41:0 denotes the projection views start at angle = 0. Therefore, using **simind** is also able to modify the parameters in ge.smc. For more detail description, the reader can refer to: *http://www.radfys.lu.se/simind/*.

3.7 Evaluation of Monte Carlo

The greatest advantage of Monte Carlo is its accuracy due to the appropriate photon transport modeling. However, the accuracy of MC is also limited by different models. Moreover, as mentioned previously, the speed of MC is very slow due to the low detection efficiency.

3.7.1 Advantage of Monte Carlo

Monte Carlo is used extensively in SPECT simulation due to its accuracy. It is able to accurately predict the physical response of a photon event and characterize the physical performance of a detector. The accuracy of a Monte Carlo code depends on the appropriate modeling of the photon event and detector component. The physical response of a radionuclide source is evaluated by comparing the simulated result with the experimentally measured data directly or indirectly. Normally, it is considered to be validated if the experimental system response can be accurately reproduced by Monte Carlo. The evaluation parameters used most often are the spatial resolution, scatter fractions and detection efficiency.

3.7.2 Drawback of Monte Carlo

One of the predominant limitations of MC is the PDF function estimation of photon events. An accurate simulation depends on having an accurate understanding of the physical system. The other drawback is the large computational burden. The directions of emitted photons are randomly distributed after they are emitted from their initial locations. Even photons traveling in the direction of the detector might not be detected because of the possibility of photon scattering. In SPECT, only about one out of 10^4 photons is ultimately detected by the imaging system. Therefore, a large number of photons must be tracked in order to acquire a high quality projection image, and each simulation of one photon event includes several time-consuming calculations at each step. This low speed makes it difficult to repeat the simulations several times to obtain a noise-free image.

3.8 Variance Reduction Techniques in Monte Carlo

It has been mentioned that Monte Carlo simulation is one of the well established tools that have been used in SPECT due to its ability to accurately model photon transport [45, 72]. However, the high computational demand of MC limits its use to research applications. In order that MC modeling be routinely used for clinical practice, it is necessary to improve the simulation speed through the use of variance reduction techniques (VRT's) [73, 74]. These methods must ensure that the accuracy of MC is maintained while it is accelerated. The models of photon scatter, attenuation and collimator response can greatly affect the quality of SPECT images [75, 76].

One technique used to improve the speed of MC modeling is the VRT known as forced detection (FD). With this method, photons are followed as they traverse the object under study, but are then forced to travel in the direction of the detector.

In FD, a photon is emitted from an initial location and may scatter at various sites in the object prior to escaping. At each scatter site, the photon can be forced in the direction of the gamma camera and is incident on the detector as shown in Fig. 3.5. The probability of detection for those photons is modified by multiplying the initial photon weight at the scatter sites with the probability the photon travels through the forced direction and is detected [72]. The forced path direction is sampled from a probability density function (PDF) obtained from the model of distance-dependent collimator response.

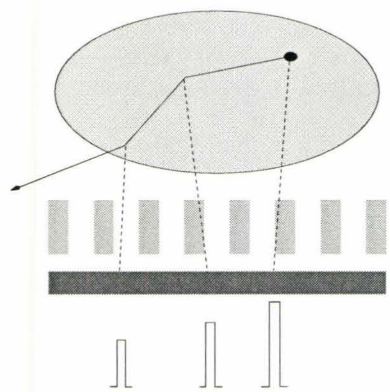

Figure 3.5: Schematic of FD. The solid lines are the scattered photon paths, and the dash lines are the forced paths.

A very simple evaluation of the forced detection method is presented here. In the evaluation, a 1-cm-length and 0.5-cm-diameter ^{99m}Tc pill is located in air and moved along the axis perpendicular to the detector when GE Millennium VG camera with LEHR collimator is used. Because of the relative large size of the detector compared with the size of the source, the ^{99m}Tc pill can be seen as a point source. The pill is moving along the axis that perpendicular to the detector. The source-detector distances are 2.54, 7.52, 12.7, 17.78, 22.86 and 27.94 cm. For each distance, the point source is scanned for 5 minutes to obtain a relatively noise free projection image with the matrix size of 1024×1024 and the pixel size $= 0.055$ cm. The parameters in the simulation are the same as the experiment except the projection images are of the size 128×128 with pixel size $= 0.442$cm. The experimental results are downsampled to match the size of simulated result.

Fig. 3.6 shows the evaluation of the FD method (the evaluation method is going to be introduced in Chapter 3). The accuracy of FD has been evaluated by measuring the FWHM's of the point spread functions for point sources positioned at different distances to the detector, as shown in Fig. 3.6(a) and Fig. 3.6(b). The profiles of a central line along the horizontal and vertical directions of the PSF's are fitted by Gaussian function and the FWHM's of the simulation results are calculated and compared with experimental data. The photon counts per second (CPS) per MBq activity for different source-detector distances are recorded (Fig. 3.6(c)). The simulation result is very similar to the experimental data. More detail has been performed by Beck, et al. [72, 77]. The count rates for the experimental data are not stable. This might because of the penetrated photons, whose amount decreases with the increase of source-detector distances.

While FD is a well used technique to increase MC simulation speed, the computation times are still too long to be clinical useful. In the next Chapter, we will present several additional techniques to improve MC simulation speed.

3.9 Conclusion

Monte Carlo is a very effective simulation tool in nuclear medicine and is able to accurately simulate the transport of photons through the patient and imaging system. In this Chapter, the simulation of transport using Monte Carlo has been described based upon random number sampling. Different types of Monte Carlo codes are compared. The general-purpose MC codes are very flexible to be modified but not easy to be used. The dedicated MC codes are more simple to use, but they are limited by the fixed system configuration. SIMIND SPECT dedicated MC code is applied in this thesis. The most significant advantage of MC is its accuracy of simulating realistic problems. However, the main drawbacks of MC are the accurate photon transport modeling and its long computation time because of the

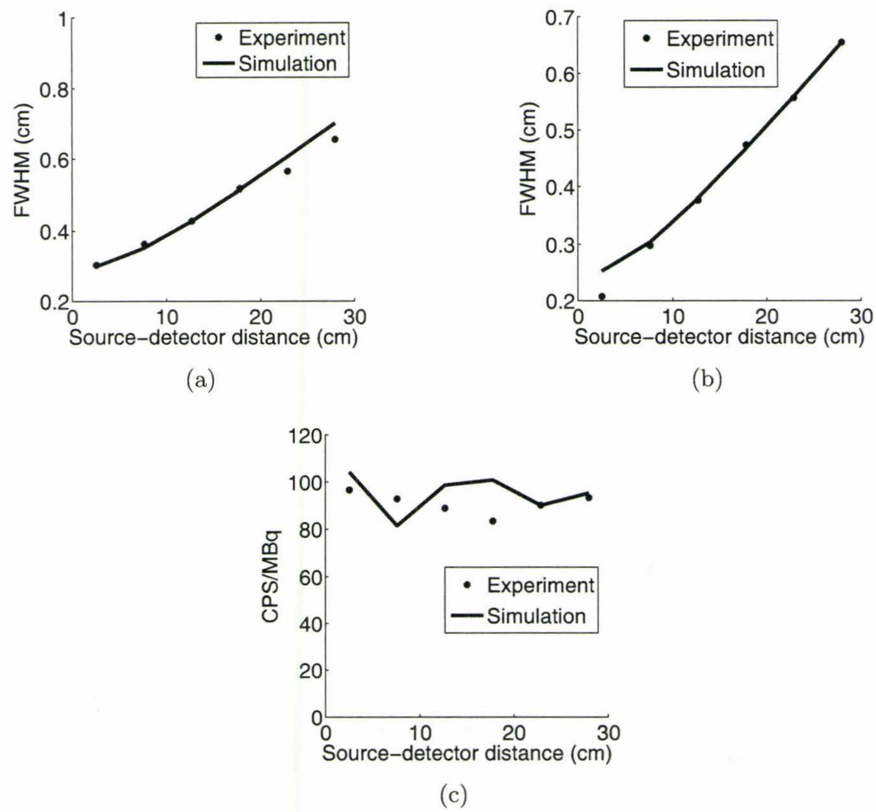

Figure 3.6: Comparison between experimental data and FD simulation result for a ^{99m}Tc point source in air with a LEHR collimator. (a) and (b) are the FWHM plots for the horizontal and vertical profiles of the experimental and simulated PSF. (c) gives the plots of the photon count number collected by the actual and simulated detectors per second (CPS) per MBq activity vs. different source distances.

low detection efficiency. Therefore, it is almost impossible to use MC code directly without any acceleration. Variance reduction techniques (VRT's) are required to accelerate MC. A well known forced detection technique has been introduced and more techniques will be developed and introduced in the following Chapter.

Chapter 4

Accelerated Monte Carlo Modeling using Improved Variance Reduction Techniques

Chapter 2 has introduced the forced detection technique used to accelerate Monte Carlo. In this Chapter, several new methods are developed aimed at further accelerating MC modeling of photon transport. The first method is convolution-based forced detection, which is based upon the concept of FD method. The other two methods, multiple projection sampling CFD (MP-CFD) method and CFD incorporating ray tracing generated models (RT-CFD), are both developed based upon the CFD method.

In forced detection, the photons are directed to the detector. A similar but more efficient method called convolution-based forced detection (CFD) is based upon the concept of FD with the exception that detected photons are convolved with a distance-dependent blurring kernel rather than a simple δ function. This method will be described in more detail in this Chapter.

In order to further increase the speed of MC, a method called multiple projection sampling convolution-based forced detection (MP-CFD) will also be presented [78]. Rather than forcing photons to interact on a single detector, the MP-CFD method follows the photon transport through the object, but then at each scatter site, forces the photon to interact with the detectors at a variety of angles surrounding the object. In this way, it is possible to simulate all the projection images in a SPECT acquisition simultaneously, rather than as separate projections. The result is a vastly improved simulation time as much of the computation load of simulating photon transport through the object is done only once for all projection angles.

With CFD or MP-CFD Monte Carlo, often only the geometric response of the collimator is modeled together with the detector intrinsic resolution, thereby making the assumption that the collimator material is thick enough to completely absorb photons at undesired angles. However, in order to retain high collimator sensitivity and high spatial resolution, the septa is made to be as thin as possible, thus resulting in a significant amount of septal penetration for high energy radionuclides. A method for modeling the effects of both collimator septal penetration and geometric response using ray tracing (RT) techniques will be presented and included into a CFD-MC program.

4.1 Phantoms Used in Computer Simulation

The evaluation of variance reduction techniques are based upon a comparison of simulated results with experimental data or with an accepted alternative method (e.g., forced detection). Point sources using different radioisotopes within differing attenuation media have first been used to validate the accuracy of VRT's. Three types of collimators, high energy general purpose (HEGP), medium energy general purpose (MEGP), and low energy high resolution (LEHR) collimators have been evaluated using different radionuclides appropriate for each collimator. A block source is used to assess the speed of each technique. The NCAT phantom has also been applied to study the case of non-uniform attenuation map.

4.1.1 Point Sources

A point source is one of the standard phantom geometries used in nuclear imaging. It is usually used to verify the accuracy of the simulated detector system. The collimator-detector response makes the projection of a point source appear as a 2D Gaussian shape on the gamma camera. This representation of a point source is usually evaluated by the point spread function (PSF) which includes an evaluation of width and detection sensitivity.

The width evaluation is performed through the measurement of full-width at half-maximum (FWHM). Horizontal and vertical line profiles of PSF are measured and these lines are fit to Gaussian functions to obtain the corresponding σ value. The FWHM value is calculated by:

$$FWHM = 2\sqrt{2\log(2)}\sigma \tag{4.1}$$

where, σ is the standard deviation of the fitted Gaussian function.

The detection sensitivity evaluation is performed by the measurement of the count rate, which is represented as counts per second (CPS) or counts per minute (CPM).

The PSF is a function that varies with the source-detector distance. In simulation, several point sources are placed at varying distances to the detector and projected onto the detector. The correlation coefficient (r^2) is used to define how well the FWHM's of different source-detector distances linearly fit experimental data. Mean square error(MSE) is taken for each distance to measure the difference between the simulation and experiment. Moreover, in order to study the effect of scatter and attenuation, point sources are usually placed in different media, such as air or water. In this chapter, uniform water phantom is taken as the attenuation map for most of the point source evaluations, since it is easy to implement in the experiment. Digital phantoms are used for more complicated non-uniform object for both this chapter and next chapter.

4.1.2 Block Source

In order to evaluate the speed improvements as a result of these accelerated methods, we have utilized a block source phantom. In radionuclide imaging, projection images are generated by collecting photons emitted from a source. Photons arrive at any point on the projection, following a statistical Poisson distribution, over a period of time. The finite scanning time results in noisy projection images that may reduce the lesion detectability. The applications of VRT's might, however, alter the properties of the noise in the projection views in a non-predictable way. Therefore, noise-free projection images are usually required in the simulation.

In order to test the noise level of the projection images, block sources are used and MC simulation is initiated using different numbers of simulated photons. The coefficient of variation (CV) is used to quantify the homogeneity of a projection image. In MC simulation, the more photons that are simulated, the better the resultant projection image quality (i.e. the smaller the CV value), but the longer the computation time. The computation time required to create images with the same CV values using different projection methods are recorded and compared with each other.

4.1.3 Digital Phantom

Following the evaluation of simple geometric shapes, more complex objects are simulated using digital phantoms to model more realistic geometries. These geometries introduce complexities due to different tissue densities and organ shapes. These phantoms have been used for the evaluation of both accuracy and speed. It is difficult to compare simulated phantom data with real patient images because these phantoms represent known situations, but the information of real patient is unknown. Therefore, in this study, the accuracy of the proposed methods are evaluated with experimental data and the evaluated methods, but not with the actual patient data.

4.2 Data Analysis Methods

Several validation methods have been used for data evaluation. The correlation coefficient (r^2) is used to provide a measure of the strength and direction of a linear relationship between two variables. The Normalized Mean Square Error (NMSE) is provided to compare two images on a voxel by voxel basis. As discussed in the previous section, the degree of homogeneity of a projection image is measured by coefficient of variation, CV.

4.2.1 Correlation Coefficient

The correlation coefficient is a measurement that indicates the degree of linear dependence of two observed data values. It is calculated from:

$$r^2 = \frac{\sum_{i=1}^{n}(x_i - \overline{x})(y_i - \overline{y})}{\left[\sum_{i=1}^{n}(x_i - \overline{x})^2 \sum_{i=1}^{n}(y_i - \overline{y})^2\right]^{1/2}} \tag{4.2}$$

where x_i is the experimental (past valued data) value, $\overline{x}$ is the mean value of x, y_i is simulated value, and $\overline{y}$ is the mean value of y. The correlation coefficient is a number between -1 and 1. If $r^2 = 0$, there is no relationship between the measured values and expected values. A value of 1.0 represents a perfect correlation between these two data sets, while $r^2 = -1$ represents a perfect anti-correlation. Therefore, the higher the correlation coefficient, the tighter the relationship between these two data sets.

The correlation coefficient is used to evaluate the accuracy of the detector response model. When a point source is imaged at a given location, the corresponding FWHM is compared with the experimental (or evaluated) values. A set of FWHM's of different source-detector distances are recorded and r^2 and mean square error(MSE) is utilized to see how close the simulated result matches the experimental (or evaluated) value. r^2 may not predict how well one group of data matches the other. Therefore, MSE is also used to estimate the difference between two data. The same application is also performed on the measurement of full width at tenth maximum (FWTM) of septal penetration when the ray tracing method is applied.

4.2.2 Normalized Mean Square Error (NMSE)

Two images can be compared on a pixel by pixel basis using the NMSE, which is the normalized mean square quantization error for all the pixels between the simulated image and the standard image. It can be calculated as:

$$NMSE = \frac{\sum_{i=1}^{n} (O_i - F_i)^2}{\sum_{i=1}^{n} {F_i}^2} \tag{4.3}$$

where, O_i and F_i are the i^{th} pixel values of the estimated images and the standard images, respectively. This error is normalized to a range between 0 and 1. It is independent of the magnitude in the predicted image or the standard image. NMSE is used to verify the accuracy of the simulated images. In contrast to r^2, the smaller the value of NMSE, the higher the degree of accuracy. NMSE is used here to measure the degree of similarity of MP-CFD generated images and CFD generated images.

4.2.3 Coefficient of Variation (CV)

The coefficient of variation (CV) is equal to the ratio of standard deviation, σ, to the mean, μ, and represents the degree of homogeneity in a set of data. It is calculated from:

$$CV = \frac{\sigma}{\mu} \tag{4.4}$$

Unlike r^2, the smaller the CV value, the more uniform the projection image. The CV value will be used in the speed evaluation when the projection times of a block source using different methods are recorded for a same CV value.

4.3 Accelerated Monte Carlo Simulation Using Convolution-based Forced Detection

4.3.1 Method

In SPECT imaging, the overall detector resolution is a combination of the intrinsic camera resolution, R_i, and the specific collimator geometric resolution, R_c. The intrinsic resolution refers to how precisely the scintillator and associated localization electronics can position an event to a specific location.

It is normally a property of the camera and usually a constant for a given photon energy. It is usually several millimeters, (3.8 mm for a 9.5 mm crystal at 140keV and 4.5 mm for a 15.9 mm crystal). The collimator resolution, on the other hand, is dependent upon the collimator length, l, hole size, h, source distance from the collimator, z, and linear attenuation coefficient, μ, for the collimator material (eg. lead) at a certain photon energy. Table. 4.1 has listed the symbols used in this section.

The overall detector resolution can be described in terms of the full width at half maximum (FWHM) [2]:

$$FWHM = \sqrt{R_i^2 + R_c^2} \tag{4.5}$$

where, R_c can be written as the following equation when a parallel hole collimator and low energy isotope are used:

Table 4.1: Symbols used CFD method.

Symbols	Definition
σ	standard deviation in Gaussian function
r^2	correlation coefficient
R_i	intrinsic resolution
R_c	collimator resolution
l	the collimator length
h	hole size
z	source-detector distance
μ	linear attenuation coefficient in the collimator material at certain photon energy
P	photon probability
α	detector angle
KN	Klein-Nishina function
ϕ	photon scattering angle
$\mu(E)$	linear attenuation coefficient for photon energy of E
l_{FP}	photon forced traveling length

$$R_c = h\left(\frac{l - \frac{2}{\mu} + z}{l - \frac{2}{\mu}}\right) \tag{4.6}$$

here, $\left(l - \frac{2}{\mu}\right)$ is the effective collimator hole thickness as it accounts for some septal penetration. It has been shown that the detector response (represented as the point spread function, PSF) of a collimator can be modeled as a Gaussian function described by:

$$PSF(x,y)|_z = \frac{1}{2\pi\sigma_x\sigma_y} \cdot e^{-\frac{(x-x_0)^2}{2\sigma_x^2} - \frac{(y-y_0)^2}{2\sigma_y^2}} \tag{4.7}$$

where $(x_0,\, y_0)$ is the central location where photons are detected on the collimator face and σ_x and σ_y are derived from the aforementioned $FWHM$ of the particular collimator.

The convolution-based forced detection (CFD) method is very similar to FD, with the exception that photons are forced to travel in the path perpendicular to the gamma camera and the detection probability being convolved with a Gaussian function determined by Eq. (4.7), and illustrated in Fig. 4.1. The convolution process is performed at every photon interaction location, and the attenuation coefficient of each directed path is calculated using a specific μ value corresponding to the given photon energy, E, at each step.

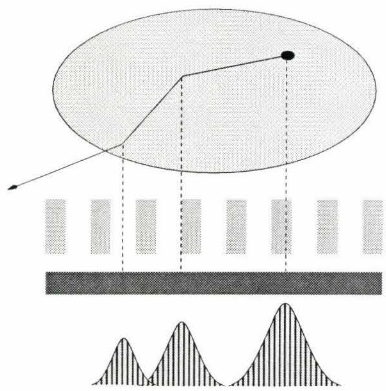

Figure 4.1: Schematic of CFD. The solid lines are the photon scatter paths and the dash lines are the forced paths in CFD. Unlike that shown in Fig. 3.5, these lines are perpendicular to the collimator face.

The main photon interaction types in SPECT are Compton scatter and photoelectric absorption. During the transport of each photon, the probability that a photon travels to a given interaction position is determined by the product of the photon history weight (PHW initially set as 1). The probability that the photon is not absorbed by the photoelectric interaction is $(1-P_{pe}(E))$ (which is approximately set as the probability of Compton Scattering), and the probability of scattering at angle ϕ due to the Compton Scattering, where angle ϕ defines the photon traveling line to the detector. The Klein-Nishina function, which is denoted as $KN(\phi)$ is introduced to calculate the probability of Compton Scattering at angle ϕ. As a result, a new photon energy (E) and direction are given for the subsequent photon transmission. At each scattering location, the attenuation of the CFD-forced photon travel path will also influence the photon history. Therefore, the probability of a photon being detected by the detector located at the angle α, can be found by:

$$P(\alpha) = PHW_i \times (1 - P_{pe}(E)) \times KN(\phi) \times e^{\int_0^{l^{\alpha}_{FP}} -\mu(E)dl} \quad (4.8)$$

where, i is the i^{th} photon interaction, and $e^{\int_0^{l_{FP}} -\mu(E)dl}$ is the attenuation factor. When the photon energy is higher than 100 keV, only Compton scatter and photoelectric absorption are dominant and, therefore, σ_{incoh} in Chapter 2 is equal to $1 - P_{pe}(E)$.

4.3.2 Evaluation of CFD Monte Carlo

CFD is a VRT method which is able to be combined with other VRT's for increased acceleration, and so the validation of its accuracy is very important. Point source responses are recorded for different source-detector distances when different collimators and radionuclides are used. The computation speed of CFD is also evaluated based upon block source projection images and compared with standard FD simulation.

In the PSF evaluation, a point source of ^{99m}Tc located in either air or water. The 100 MBq source is placed in a 1 cm long and 0.5 cm wide pill, which can be seen as a point source compared to the size of the detector. Fig. 4.2 depicts the experimental setup. Only head 1 is used in this simulation, and the source-detector distances for different sources and collimators are listed in Table 4.2.

In the experiment, the point source at each distance is imaged for 5 minutes using a GE Millennium VG camera with a LEHR collimator to acquire a 1024×1024 pixel, noise-free projection image with pixel size = $0.055cm$. 20% energy window (126-154 keV)is applied here.

In the CFD simulation, a point source is moved along the central axis of a $128 \times 128 \times 128$ object (voxel size = 0.442 cm^3) while the phantom contains either air or water. The simulated detector is the same as the experiment. The units in Monte Carlo simulated images is counts/second. Therefore, the simulated projection

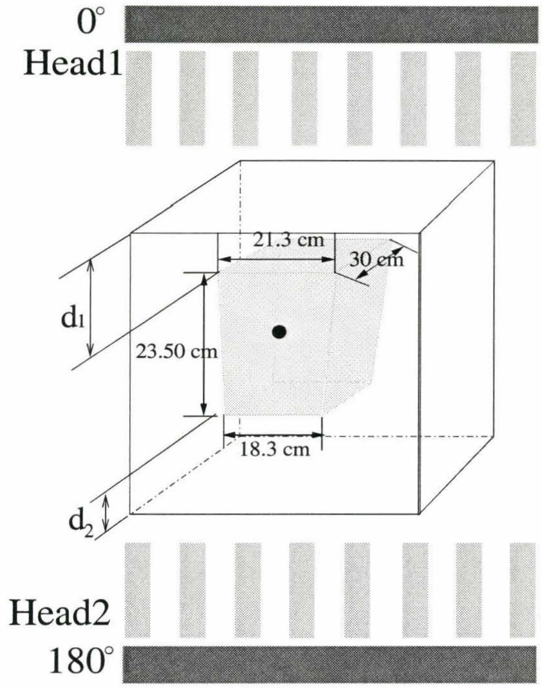

Figure 4.2: Point source in the phantom (gray area) and scanned by a dual head detector. Two detectors are placed opposite to each other. When LEHR is used, d_1 = 0 cm, and d_2 = 6.98 cm. When MEGP and HEGP collimators are used, d_1 =9.94 cm, d_2 = 22.44 cm.

images should be multiplied by the projection time, which is 300 seconds. The projection images are set as 128 × 128 pixels and only geometric response modelling is applied.

Fig. 4.3 and Fig. 4.4 shows the FWHM evaluation of the PSF's for the two types of simulations (LEHR/air, LEHR/water). The experimental data has been downsampled to match the dimensions of the simulated image. The vertical and horizontal central line profiles of the resultant PSF's are fitted to Gaussian curves and the FWHM's are calculated and compared with the experimental data. In Fig. 4.4, the widths of the experimental results are always higher than the simulated data may because there are some scattered photons that are not included in the simulation.

Fig. 4.3 presents the FWHM comparison of the experimental data along with

Table 4.2: The source-detector distances using different isotopes and collimators when attenuation medium is/isn't included. Dual head detector is used to produce the projection images. The unit of these distances is cm. Numbers without * denote source-detector distances when the projection views are acquired by head 1, and numbers with * are for head 2. The numbers in the brackets are related to the source depth in the water to the corresponding detector.

No.	^{99m}Tc-LEHR-no att	^{99m}Tc-LEHR-att	^{111}In-MEGP-no att	^{131}I-HEGP-no att	^{131}I-HEGP-att
1	2.54	2.54 (2.54)	2.54	2.54	15.24 (5.30)
2	7.52	7.52 (7.52)	7.62	7.52	18.20 (8.26)
3	12.7	12.70 (12.70)	12.7	12.7	22.86 (12.92)
4	17.78*	17.78 (17.78)	17.7	17.78	27.94 (18.90)
5	22.86*		25.4	25.40	27.94 (5.50) *
6	27.94*		30.48*	30.48*	33.02 (10.58)*
7			38.10*	38.10*	37.68 (15.24)*
8			43.18*	43.18*	40.64 (18.20)*
9			48.26*	48.26*	
10			53.34*	53.34*	

the simulated results when the ^{99m}Tc source is placed in air. The simulation results of the sources in air are very accurate, with good agreement between the experiment and simulation, as the r^2 values are both higher than 0.99 in Table 4.3. However, as shown in Fig. 4.4, when the source is placed in water, there are some differences in PSF's between experimental data and CFD results in the presence of attenuation and scatter. Table 4.3 summarizes the r^2 values of these FWHM evaluations. Although the simulation results for point sources in water is not as accurate as the results of sources in air, the r^2 value is still greater than 0.99, which denotes that the simulation results linearly correlate well with the experimental data. The mean square error between the experimental data and simulated data is much higher than the result in air, which means there are some errors when attenuation map is included.

Fig. 4.5 shows the evaluation of count rate for both cases when the source is either in air or in water. The y-axis in Fig. 4.5 denotes the number of photon counts collected by the real system and simulated detector per second (CPS) for a 1 MBq

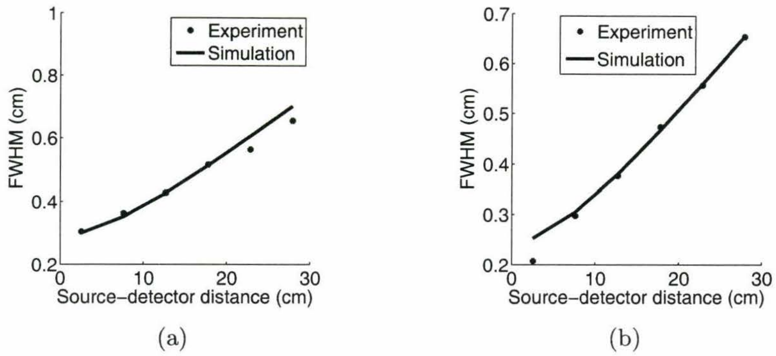

Figure 4.3: PSF CFD simulation results compare with the experimental data using LEHR collimator when the ^{99m}Tc source is placed in air. The left is the FWHM evaluation of the horizontal and the right is for the FWHM vertical profile evaluation.

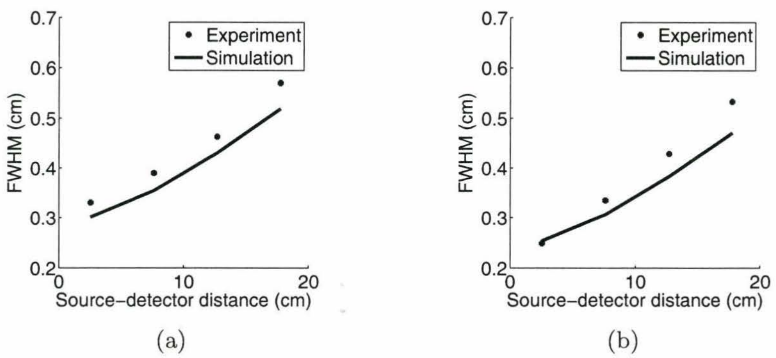

Figure 4.4: PSF CFD simulation results compare with the experimental data using LEHR collimator when the ^{99m}Tc source is placed in water. The left is the FWHM evaluation of the horizontal and the right is for the FWHM vertical profile evaluation.

source. Fig. 4.5(a) shows the count rate when a ^{99m}Tc source is placed in air. It is noted that the count rate should be stable and independent of the source-detector distances because no attenuated photons are considered. The experimental count rate fluctuates around 90 CPS/MBq (about 10% variation) as a result of penetrated photons. The CFD generated results are more stable and close to the experimental result.

Fig. 4.5(b) shows the simulation of ^{99m}Tc in water. In order to more easily analyze the effect of attenuation, the x-axis is set as depth of the source in water.

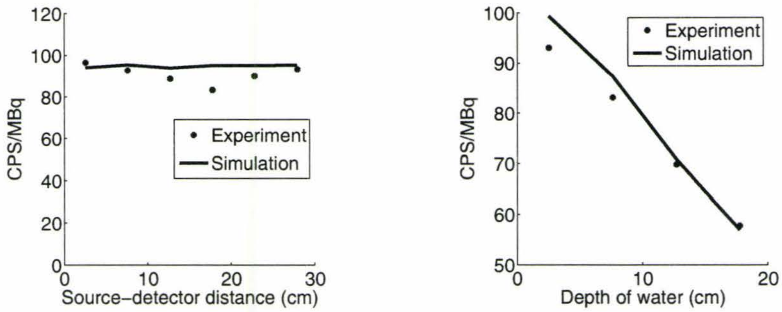

Figure 4.5: The photon counts collected per second (CPS) comparison between the experimental data and the simulation. (a) and (b) are related to ^{99m}Tc in the air and water, respectively.

It can be seen that the CFD simulated results are close to the experimental result. The count rate decreases when the depth of source in the water increases. This is because when the depth increases, the attenuation fraction in Eq. 2.16 decreases and the signal intensity also decreases. In theory, the count rate curve should be exponentially decreased, however, the curves here are linear decreased probably because the real system and simulated system has a wide energy window (126-154 keV) and may collect a lot of scatter. Compared to the detection efficiency of HEGP collimator, which is shown in the next section, different collimators will also affect the detection efficiency, therefore, the linearly decreased lines in Fig. 4.5(b) may only be contributed by the application of LEHR collimator.

Table 4.3: r^2 and MSE value of FWHM of PSFs in the air and water using CFD method when LEHR collimator and ^{99m}Tc are used.

source/collimator	$Hori.(air)$	$Vert.(air)$	$Hori.(h2o)$	$Vert.(h2o)$
r^2	0.998	0.999	0.997	0.997
MSE	0.063	0.046	0.107	0.076

In the speed evaluation, CFD results are compared to standard FD results. A $30cm \times 30cm \times 30cm$ ^{99m}Tc block source is simulated in the center of a $128 \times 128 \times 128$ matrix (voxel size = 0.442 cm^3). A GE Millennium VG camera with LEHR collimator is simulated to acquire the projection images. Different numbers of photons are simulated by CFD and FD: 1×10^5, 2×10^5, 5×10^5, 6.5×10^5, 1×10^6, 2×10^6, 5×10^6, 7.5×10^6, 1×10^7, 2×10^7, 3×10^7, 4×10^7, 5×10^7. The simulation time of each projection image is recorded for both CFD and FD and the CV value is calculated. Fig. 4.6 shows plots of the CV value vs computation time for both methods. It takes FD about 200 seconds to obtain a stable CV value of 0.06, but it only takes CFD 40 seconds to obtain a stable CV value of 0.01. The projection images of the stable CV values using CFD and FD are shown on the Fig. 4.6(b). The stable CV level of FD is higher than the stable CV level of CFD. Therefore, CFD is not only able to increase the speed of MC by a factor of 5, but also increase the signal to noise ratio (SNR) by a factor of 6.

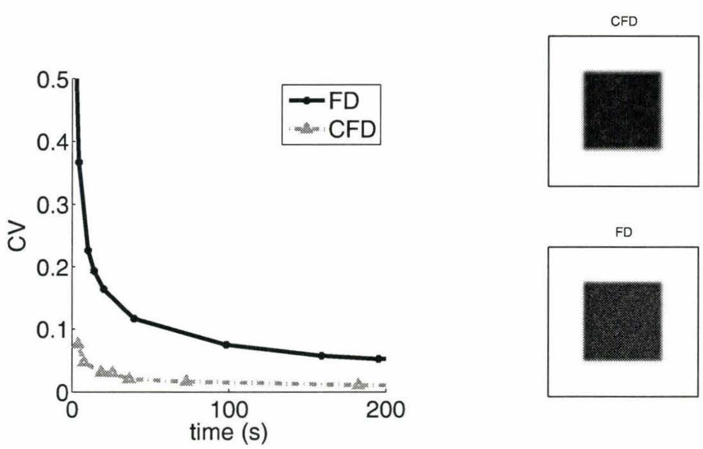

(a) (b)

Figure 4.6: The CV comparison of FD and CFD over different computation time in (a). (b) is the projection images for CFD and FD with the corresponding stable CV vlaue.

In order to further verify the accuracy of CFD, the NCAT phantom has been used to compare the result of CFD with FD. A total of 100 MBq of ^{99m}Tc is simulated in the phantom. The main four organs with their activity amounts are heart (8.5 MBq), kidney (10 MBq), lung (10.5 MBq) and liver (48 MBq). The total activity of these four organs is 77 MBq, and 23 MBq activity is distributed in the rest of the NCAT phantom such as bone, stomach, et, al. Again, a GE Millennium

VG camera with LEHR collimator is modeled to generate projection data. 10^{10} photons are simulated by FD to provide a reference image. Different numbers of photons(3×10^5, 10^6, 10^7, 10^8, 10^9) are simulated by CFD and all projection images are anterior views.

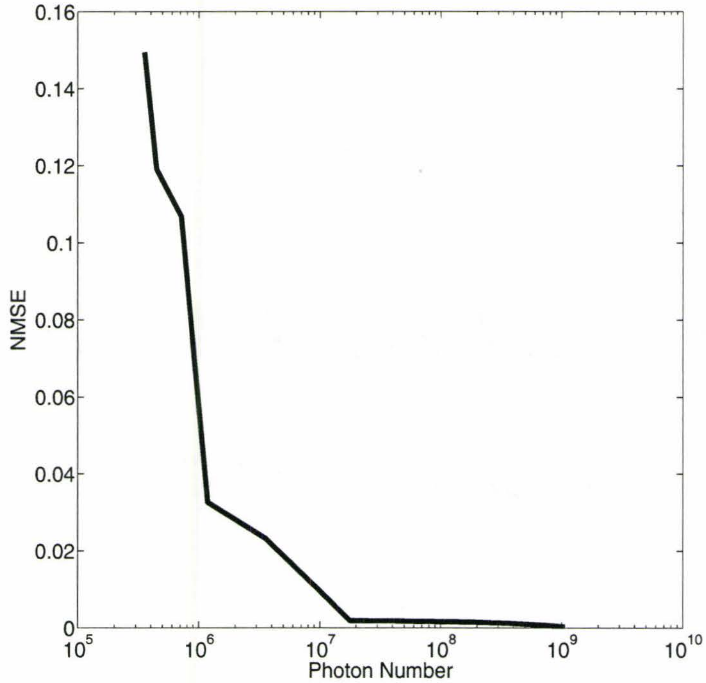

Figure 4.7: NMSE values of CFD generated result compared with FD method using NCAT phantom.

Fig. 4.7 shows NMSE values of CFD generated images compared with the reference image when the number of simulated photons varies. When the total number of photons is higher than 10^7, the NMSE yields a stable value and the error is less than 0.01. Fig. 4.8(b)-Fig. 4.8(e) show slice profiles of CFD simulated results and the reference image. The slice profiles are related to the lines in the reference image of Fig. 4.8(a), and the number of photons shown for CFD simulations. It can be seen that when 10^7 photons are simulated, the CFD simulated result is close to the reference image. Although larger numbers of photon simulations results in reduced

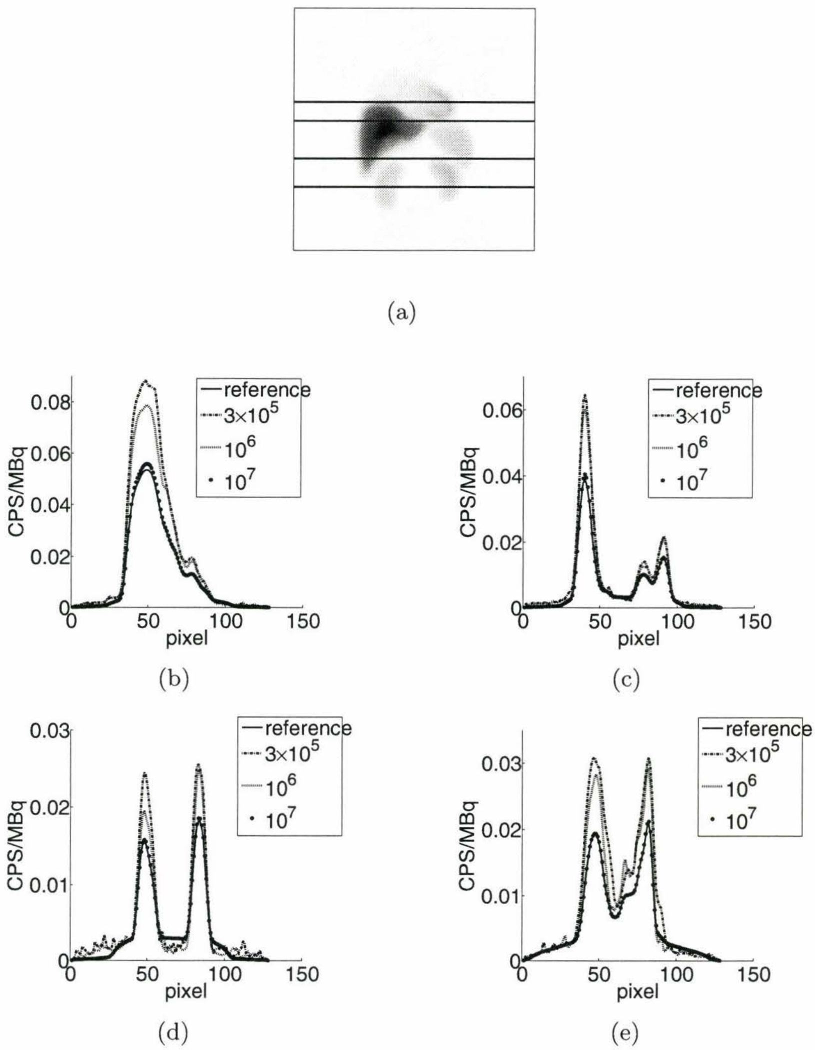

Figure 4.8: NCAT phantom simulation result by CFD method. The reference image is generated by the simulation of 10^{10} photons. (a) is the reference projection image with four line profiles shown on (b),(c),(d) and (e) with three different photon numbers.

noise in the projection image, the small noise reduction results in a substantial increase in computation time. In the complex real phantom simulation, at least 10^7 photons are needed to obtain a noise-free projection image.

4.4 Accelerated Monte Carlo Simulation Using Multiple Projection Sampling and Convolution-based Forced Detection

4.4.1 Method

In both FD and CFD, photons are forced to travel towards the gamma camera. It is noted that the detection of these photons occurs at only a single projection angle for each simulated photon. When a SPECT acquisition is performed, however, the projection data must be acquired using cameras at different projection angles. Thus, when using conventional FD and CFD, the simulation time increases linearly with the number of projection angles simulated.

We now introduce the multiple projection sampling method (MP) which will simulate projection images at different angles around the object simultaneously. An illustration of this method is shown in Fig. 4.9(a) and Fig. 4.9(b). Several detectors are modeled simultaneously with the number of detectors and their angular distributions being dependent upon the SPECT acquisition parameters. A photon is emitted from the site of decay to a certain interaction point, and subsequently is directed to each of the detectors surrounding the object. The CFD method is implemented to every detector by forcing the photon to travel along the path directly to each of them, which is depicted in Fig. 4.9(b). Table. 4.4 has listed the symbols used in this section.

When the photons are directed to different cameras, the probabilities are different at each angle due to differing attenuation paths and the probability of Compton

Table 4.4: Symbols used in MP-CFD method.

Symbols	Definition
σ	standard deviation in Gaussian function
r^2	correlation coefficient
R_i	intrinsic resolution
R_c	collimator resolution
P	photon probability
α	detector angle
KN	Klein-Nishina function
ϕ	photon scattering angle
$\mu(E)$	linear attenuation coefficient for photon energy of E
l_{FP}	photon forced traveling length
θ	detector angle in MP-CFD simulation

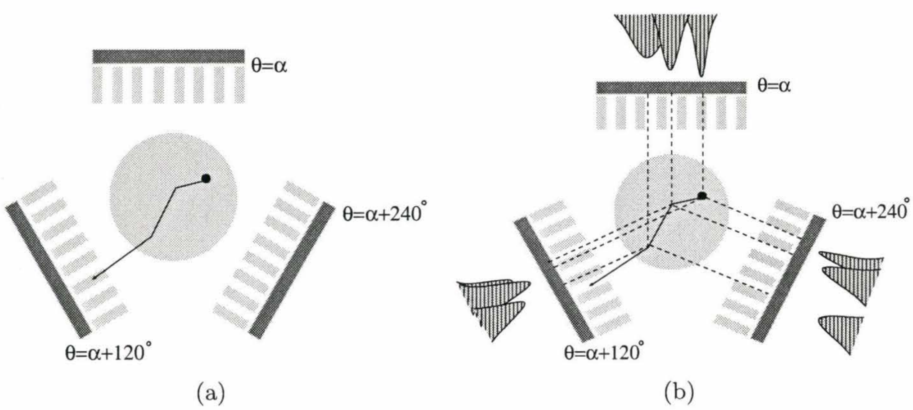

Figure 4.9: Schematic illustration of multiple angle projection. α is the location of the base projection detector, and θ shows the location of one of other detectors. (a) Multiple detectors around the object. (b) Multiple angle projection using CFD.

Scattering. Thus, the overall probability of detecting a photon at angle θ can be written as:

$$P(\theta) = PHW_i \times KN(\phi + \theta - \alpha) \times (1 - P_{pe}(E)) \times e^{-\int_0^{l_{FP}^{\theta}} \mu(E)dl} \qquad (4.9)$$

where $(\phi + \theta - \alpha)$ is the Compton scatter angle required for the photon to be detected by the detector at angle θ. Combining Eq. 4.8 and Eq. 4.9 together, we have:

$$P(\theta) = P(\alpha) \cdot \frac{e^{-\int_0^{l_{FP}^{\theta}} \mu(E)dl}}{e^{-\int_0^{l_{FP}^{\alpha}} \mu(E)dl}} \frac{KN(\phi + \theta - \alpha)}{KN(\phi)} \tag{4.10}$$

where, $P(\alpha)$ denotes the photon detection probability for the detector at the angle of α, which acts as the base projection detector. $P(\theta)$ is the photon event detection probability for the detector at angle θ, and l_{FP}^{θ} is the forced path (FP) length in the direction of θ angle detector. $\mu(E)$ is the linear attenuation coefficient corresponding to the photon energy E , which is assumed to be constant along the forced path. The term $e^{-\int_0^{l_{FP}^{\theta}} \mu(E)dl}$ gives the attenuation along the path perpendicular to the detectors at the angle of θ, from the photon scatter locations to the corresponding detectors. In practice, we assume the attenuation term consists of both Photoelectric Effect and Compton scattering probability, and the probabilities of Compton scattering at different angles are equal to each other. Therefore, Eq. 4.10 can be approximated as:

$$P(\theta) = P(\alpha) \cdot \frac{e^{-\int_0^{l_{FP}^{\theta}} \mu(E)dl}}{e^{-\int_0^{l_{FP}^{\alpha}} \mu(E)dl}} \tag{4.11}$$

The detection probabilities of photons to different detectors are calculated at each photon interaction location using Eq. (4.8) and Eq. (4.11).

deJong et,al. [79] have developed a method of extending a base projection to multiple projections which is close in angle to the base projection in a similar manner which is more precise than our method. However, in their method, the scatter photon locations are stored in several layers, which may cause some blurring due to the thickness of the layers when projected at large angles. Our method is based upon the calculation of photon physical locations. The maximum angle of the multiple projections away from the based projection can be adjusted depending on the degree of accuracy required in the simulation, but the cost is the computation time.

4.4.2 Evaluation of Monte Carlo Simulation Using Multiple Projection Sampling

MP-CFD is an extension of CFD that simulates multiple projections around the object based upon the photon traveling to a single detector. The evaluation of this method focuses on the validation of the accuracy of MP-CFD compared with the result of CFD when the photons are directed to different detectors at multiple angles, separately.

To test the accuracy of the MP-CFD method, projection images of a distance dependent point source are obtained and again compared with the experimental measurement. A HEGP collimator has been used with a 100 MBq ^{131}I point source located in either air or water. The evaluation using uniform attenuation map is going to be performed later on. The experimental setup with point sources located in the attenuation medium (non-radioactive water) is the same as depicted in Fig. 4.2. A two-head GE Millennium VG detector is used in order to increase the detection efficiency. 20% energy window (328-400 keV) is used here. The acquisition time for each frame is 5 minutes. The point source is moved along the central axis of the phantom, varying the source detector distance, as seen in Table 4.2. The normal CFD method is run twice for each source location in order to acquire simulated images for both detector heads, whereas, the MP-CFD code only needs to simulate once to obtain the images of both heads. However, in order to validate the effect of base projection, MP-CFD is performed twice using both head 1 and head 2 as base projections, respectively. Therefore, MP-CFD will generate 4 projection images for each point source. In both CFD and MP-CFD simulation, models of geometric response only are used. The center profile through each projection image has been fit to a Gaussian function. The FWHM of the Gaussian function, and the total counts of each projection image detected per second (CPS) for 1 MBq activity are recorded for comparison with the experimental data.

Fig. 4.10 depicts CFD and MP-CFD generated results compared with the experimental measurement for point sources in air. The result of MP-CFD is the measurement of both head 1 and head 2 using head 1 as base projection. Fig. 4.10(a) and Fig. 4.10(b) depict very good agreement of normal CFD and MP-CFD generated images by both detector heads with the experimental data in air. Fig. 4.10(c) shows the photon count rate in counts per second for 1 MBq activity (CPS). It can be seen that the detection sensitivity of both MP-CFD and CFD simulation is somewhat lower than the real value. This is because the convolution kernel used in CFD only includes geometric resolution, which lacks the penetration model. On average, the photon detection sensitivity of CFD is about 8 CPS (20%) lower than the actual value (40 CPS) of all the source-detector distances due to the amount of SP photons. In order to further study the effect of SP, Fig. 4.10(d) shows the numbers of detected photons for different source-detector distances when both geometric resolution and septal penetration are considered in the convolution model (more detail will be discussed in the next section). It can be seen that the detection sensitivity is now close to the actual value. SP results in about 20% more than geometric resolution model when the source is in the air. When high energy radionuclides are used, septal penetration and collimator scatter can not be ignored. In this thesis, septal penetration is going to be modeled.

Fig. 4.11 shows a comparison of the horizontal and vertical FWHM measurements for FD and CFD, along with the relative sensitivity detected by these two heads when the point source is located in water. The source-detector distances and depth in water can be seen in Table 4.2. Fig. 4.11(a) evaluates the accuracy of MP-CFD when using head 1 as the base detector, and Fig. 4.11(b) shows the evaluation of MP-CFD when using head 2 as the base detector. The first two columns of Fig. 4.11(a) and Fig. 4.11(b) give the evaluation of MP-CFD generated images on head 1, with the other two columns showing the evaluation of the head 2 results. The top rows of Fig. 4.11(a) and Fig. 4.11(b) compare the detector resolution in terms of FWHM with the x-axis set as the source-detector distance. It is not sur-

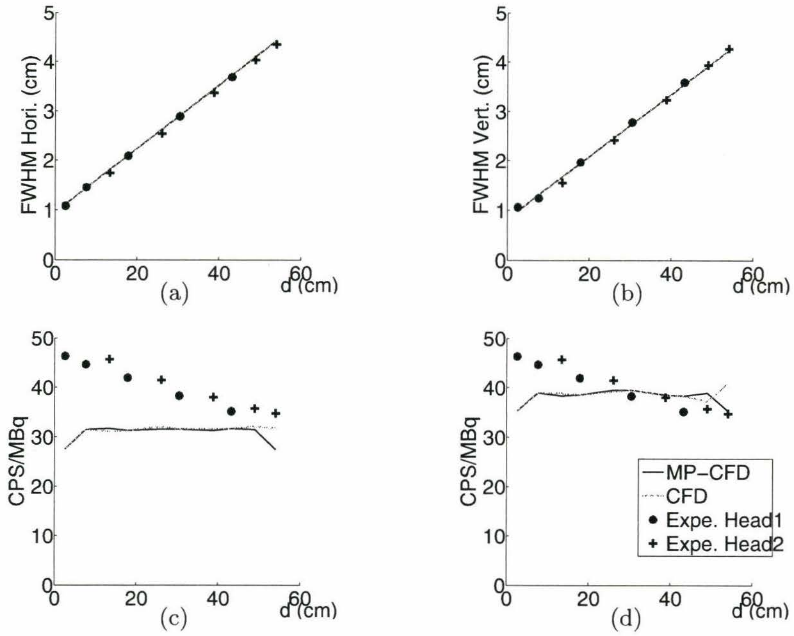

Figure 4.10: Simulation result of PSF in air using HEGP collimator. The horizontal and vertical widths of the PSFs are validated by FWHM in (a) and (b). (c) and (d) show the average counts detected by the camera per second given 1 MBq activity for simulations and experimental data w/o and with SP modeling. d denotes the distance between the point sources and the corresponding detector.

prising that MP-CFD matches CFD for base projection images, and they both agree well with the experimental data. For the off-base projection images, there are some slight differences between MP-CFD, CFD simulations and the experimental data. This maybe because of the difference between the two detector heads due to manufacturing even though they are supposed to be identical and the approximations in Eq. 4.11. The bottom rows of Fig. 4.11(a) and Fig. 4.11(b) provide a comparison of the average detection sensitivity of these two heads. The x-axis has been set as the depth of water from the point source to the detector in order to observe the effect of attenuation. It has been noted that our simulation results compare well to the detection sensitivity of head 2, but not head 1, when no SP is included. However, when SP is included, both the results are similar to the actual value. Table 4.5 gives the r^2 and MSE value for FWHM measurement in Fig. 4.11. The value shown in the table for MP-CFD is the average r^2 or MSE value for the simulation results related to the two detector heads using different based detector. The result of MP-CFD agrees well with CFD, and both are correlated with the experimental data as r^2 values for FWHM are all above 0.99 and most of the MSE is less than 0.1cm.

Table 4.5: r^2 value and MSE of FWHM of PSFs in air and water between the experimental data and MP-CFD or CFD simulation result when HEGP collimator is used. (Note: the results are the average value of head 1 and head 2, the unit of MSE is cm.)

source	$Hori.(air)$	$Vert.(air)$	$Hori.(h2o)$	$Vert.(h2o)$
MP-CFD (r^2)	0.9980	0.9990	0.9971	0.9974
MP-CFD (MSE)	0.0164	0.0202	0.0706	0.1160
CFD (r^2)	0.9980	0.9980	0.9975	0.9981
CFD (MSE)	0.0083	0.0229	0.0458	0.0796

Fig. 4.11 also shows the detection sensitivity evaluation of PSF's for MP-CFD and CFD. The first and third columns of Fig. 4.11(a) and Fig. 4.11(b) are for the simulation result without septal penetration photons, and the other columns are with septal penetration photons. It can be seen that the simulation results do not match head 1 and head 2 simultaneously. This may because of two reasons: 1) the two heads are not identical through they are supposed to be. 2) there is some error of MP-CFD while ignoring the difference of Compton scattering. Observing the results of both heads, it can be seen that the amount of penetrated photons compared to the geometric photons are different for different source-detector distances. When the source is close to the detector, the ratio of penetrated photons to geometric photons is about 1:2, however, when the source is far away from the detector, this ratio is reduced, and the amount of penetrated photons can be neglected.

In order to further verify the accuracy of the PSF's generated by MP-CFD when only geometric response is included (no septal penetration modeling), Fig. 4.12 presents the profiles of the two projection images detected by head 1 and head 2 using head 1 as the base projection, when the point source is placed 22.86 cm away from head 1 detector (33.02 cm away from head 2). Therefore, the depth in water to the two heads are 12.92 cm and 10.58 cm, respectively. The left column

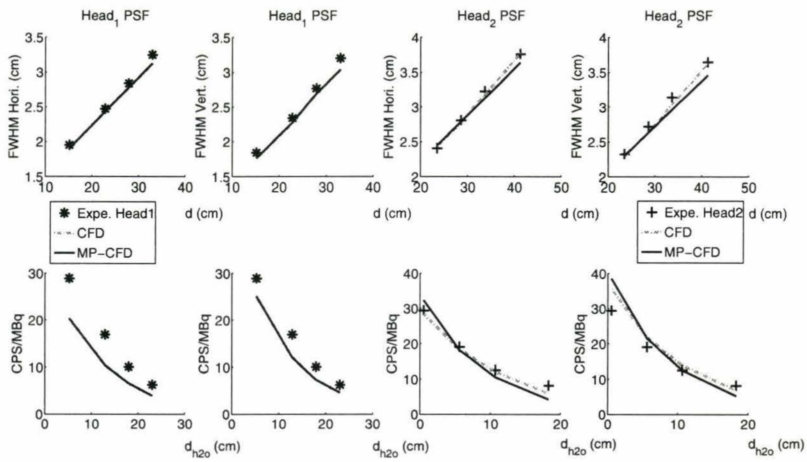

(a)

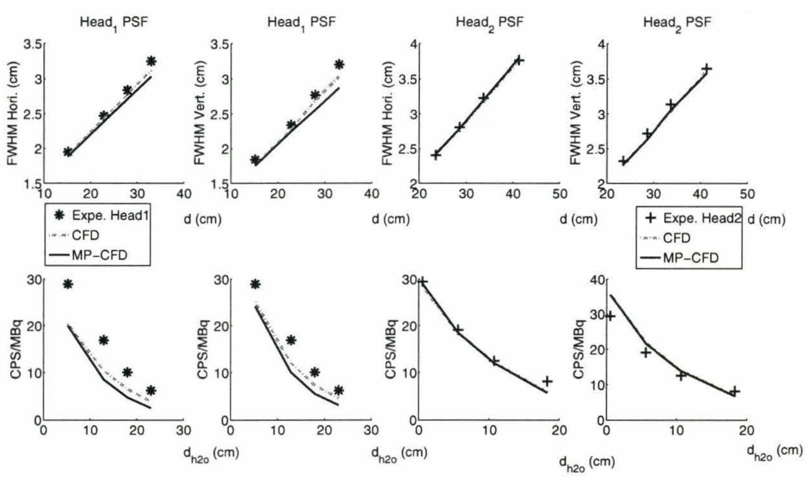

(b)

Figure 4.11: Simulation results of point sources in no activity water container using HEGP. The MP-CFD simulation results comparison using head 1 as base projection is shown on (a), with (b) giving the results using head 2 as the base projection. The first two columns in (a) and (b) are the comparison of head 1 detection, and the rest two columns are the results of head 2 detection. The first and third columns of top row are the horizontal direction FWHM measurements, and the second and fourth columns are the vertical direction measurements. The first and the third columns of the second row are the photon amount evaluation when the septal penetration photons are not included, with the second and fourth columns of the second row showing the photon amount evaluation with septal penetration photons. d denotes the distance from the point source to corresponding detector head. d_{h2o} denotes the depth of water from the point source to the detector.

shows the projection images on head 1 and head 2. The dots correspond to the photons traveling through the collimator holes, whereas the areas between these dots correspond to septa where most of the photons are stopped. The middle column shows the PSF profiles and are compared with experimental data in order to evaluate the accuracy in more detail. The MP-CFD simulated result is smoother than the experimental result because septal penetration is neglected. However, the profiles of simulated result is very close to the experiment. The right column shows the log value of the profiles. Although the central part of MP-CFD simulation is close to the experiment, the tails are lower than the experimental result. The difference is related to septal penetration photons because the convolution models in MP-CFD does not include penetrated photons. Combined with the detection sensitivity, it can be said that septal penetration photons can not be neglected when high energy photons are imaged using conventional collimators.

The accuracy of MP-CFD has also been investigated by simulating a SPECT acquisition of the NCAT phantom. 120 noise-free projection images were simulated using a HEGP collimator with the $64 \times 64 \times 64$ voxel NCAT phantom containing 100MBq of ^{131}I. The activity concentrations of different organs are the same as the simulation in Fig. 4.8. The voxel size of the phantom is set as 0.884 cm. CFD projection images are used as the reference images. Both CFD and MP-CFD simulation use geometric response models as the convolution kernel. A total of 100 million photons were simulated for each CFD projection, while the MP-CFD method required only a total of 100 million photon simulations for all 120 projection angles. Three base projection detectors are chosen (at the angle of $\alpha = 0°$, $\alpha = 80°$, and $\alpha = 200°$).

The NMSE value, as a function of detector angle, is introduced to evaluate MP-CFD accuracy compared to CFD images. Results are plotted in Fig. 4.13. The maximum NMSE error is less than 0.03 for all measurements using different base projections. Fig. 4.14 depicts the comparison of resultant images of $\alpha = 0°$

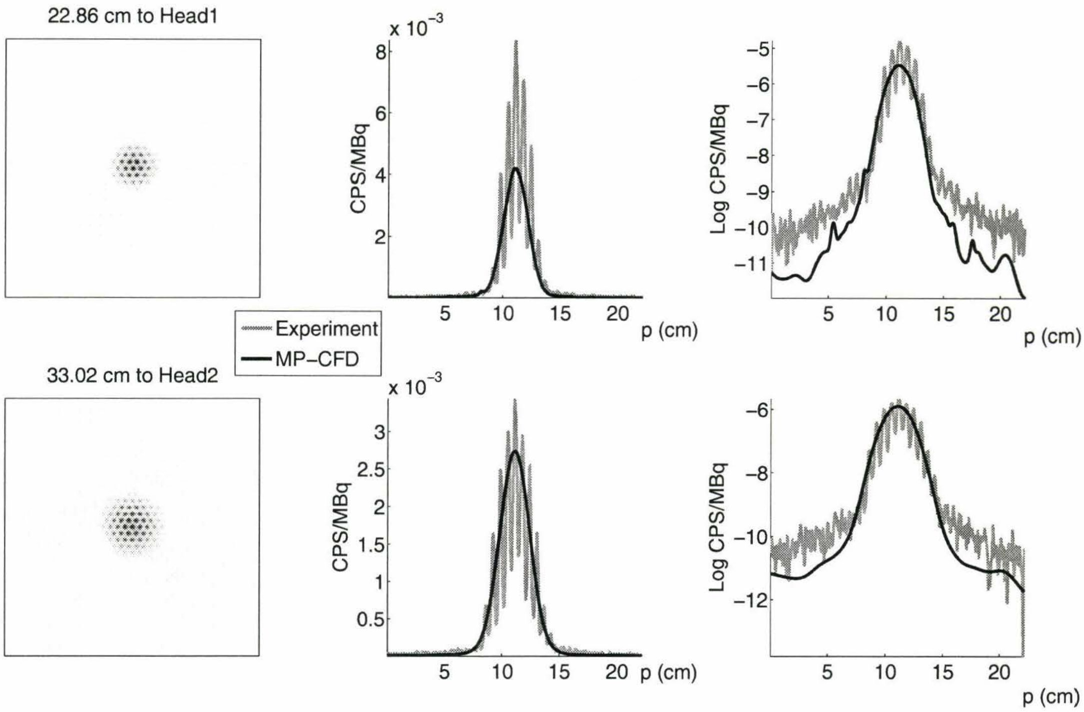

Figure 4.12: Dual head SPECT point source detection result comparison between MP-CFD and experimental data. Top row are the comparison of head 1 detections, with bottom row showing comparison of head 2 detections. The left column are the experimental projection images of these two heads, and the middle column show the center horizontal linear profiles. The right column are the log value of the center profiles.

base projection MP-CFD and CFD for different detectors when $\theta = 0°$, $\theta = 120°$, and $\theta = 240°$. Several line profiles at the maximum error and other locations are analyzed thereby verifying the accuracy of MP-CFD compared to CFD. The phantom is upside down, so the last line profiles are across the lungs. It can be seen that the projection images of MP-CFD and CFD are well matched.

The same $64 \times 64 \times 64$ voxel NCAT phantom has also been used in speed tests of the MP-CFD method. A varying number of detectors (N_p) have been simulated using MP-CFD and the resultant projections are compared to CFD simulated projections with the same number of projections. For each simulation, the total computation time for CFD and MP-CFD was recorded. As seen in Fig. 4.15, the

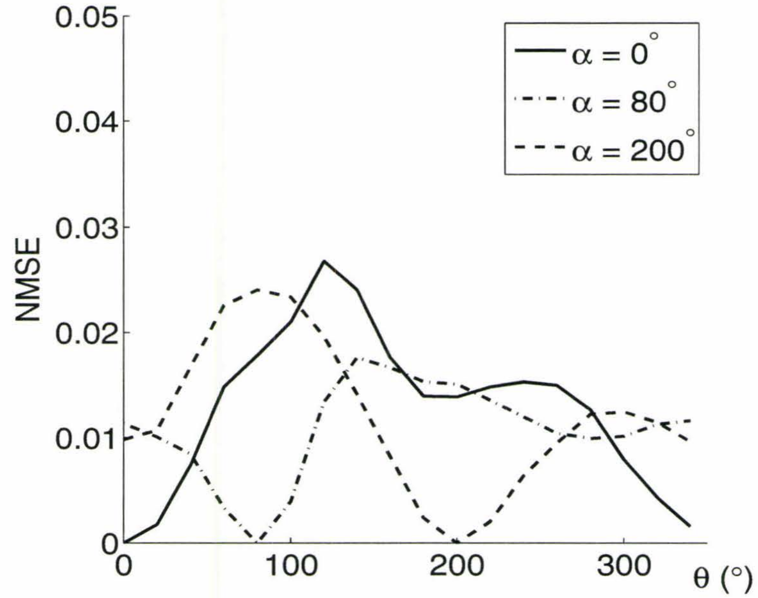

Figure 4.13: NCAT phantom MP-CFD resultant images NMSE comparison with CFD generated images. α is the location of base projection detector. θ denotes the location of gamma camera. The maximum error is less than 0.03 for the projection images around $\theta = 120°$.

simulation time of one CFD (for one MP-CFD) projection view for 100 million photons is about 80 seconds, which includes 68 seconds for photon propagation inside the phantom and 12 seconds for the attenuation and convolution calculation. With increasing numbers of detectors, the MP-CFD computation time increases because of the calculation of attenuation and convolution at each angle, however, the computation time is linear with the number of projections for both CFD and MP-CFD but with different slopes. The MP-CFD method is about 6 times faster than CFD.

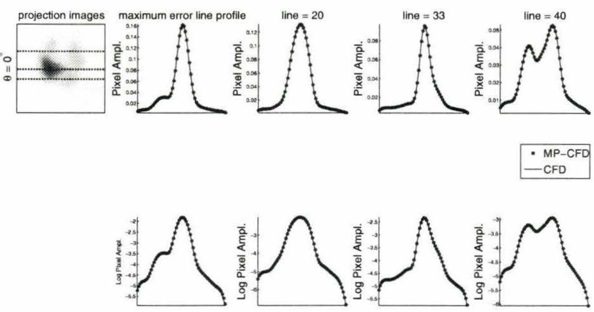

(a)

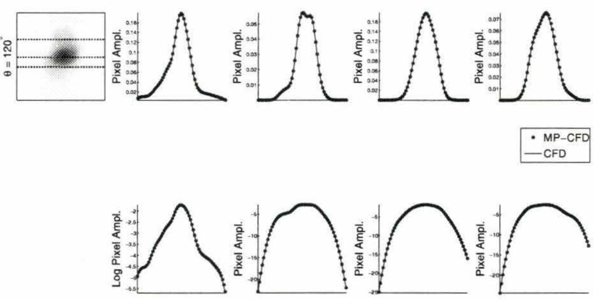

(b)

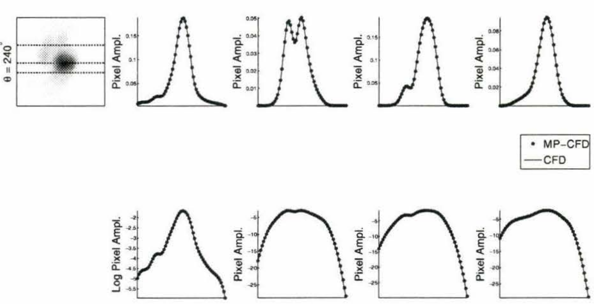

(c)

Figure 4.14: Line profiles of NCAT phantom images projected by MP-CFD ($\alpha = 0°$) and CFD. The plots in (a), (b) and (c) are for $\theta = 0°$, $\theta = 120°$, and $\theta = 240°$ projection images, respectively. The first column in each one shows the projection images generated by CFD. The second column are the profiles of maximum error, while the others are the specific lines denoted at the top. Except the projection image, the first row of each sub-figure gives the linear line profiles, with the second row presenting their log values.

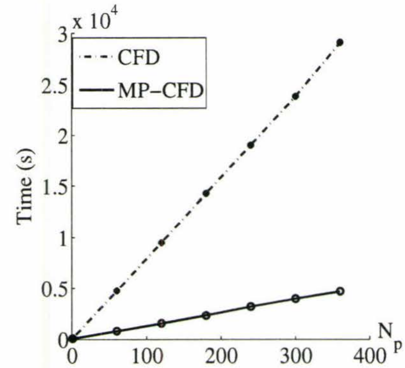

Figure 4.15: Computation time comparison between CFD and MP-CFD. N_p denotes the number of detectors to be simulated.

4.5 Convolution-based Forced Detection Monte Carlo Simulation Incorporating Collimator Response Modeling

4.5.1 Collimator Response Modeling

With CFD, the probability of photon detection is convolved with a Gaussian blur function representative of the collimator geometric response function. This mathematical model only estimates the response based on the assumption that photons interacting within the collimator material will be completely absorbed. However, when the photon energy exceeds 200 keV, there is high probability that photons will be able to penetrate the collimator, yet still be detected by the camera [27]. Furthermore, some photons may interact in the collimator material before they penetrate the collimator septa. Therefore, a complete characterization of the collimator response involves geometric response (GR), collimator septal penetration (SP) and collimator scatter. Although different collimators are used to minimize the amount of septal penetration, thin septa are preferred when high detection efficiency is required. Therefore, the effect of penetrated photons is typically significant when medium or high energy radionuclides are used. Overall, the amount of penetrated photons is determined by photon energy and the path length of rays through the septa which depends on the distance between the radioactive source and collimator, collimator material, collimator length, collimator hole pattern and septal thickness [80].

Several studies have been done to model collimator response. Ljungberg, et al. have developed a Delta-Scattering technique by sampling a series of random numbers to determine the photon interaction types in the collimator when photons are tracked [57]. Du, et al. used Monte Carlo N-Particle (MCNP) to simulate photon interaction types in the collimator [81]. Song, et al. presented a method using MC code to generate the collimator response models based upon the angular response functions (ARFs), which depends on the photon traveling directions and photon energies [82]. Recently, Staelens, et al. used convolution-based forced detection (CFD) to convolve the photon transmission probabilities with MC-derived collimator responses when ray tracing is performed onto the object [83]. However, the MC simulation of a noise-free collimator response image is extremely time consuming. In this work, we will introduce a method using ray tracing (RT) to analytically generate the collimator response model incorporating both GR and SP. The collimator scatter component is not going to be discussed here because of the difficulty of analytically simulating photon scatters. RT has been used previously to evaluate the collimator characteristics by modeling the collimator response [27, 80, 84], however, it has not been applied to compensate for the collimator response. The RT models are applied to CFD-MC when septal penetration is needed to be simulated in order to provide further acceleration. Table. 4.6 has listed the symbols used in this section.

In RT method, a point source O is simulated at a distance of z away from the collimator front face, as shown in Fig. 4.16(a). Several rays (OB) are traced from the point source to the collimator in different directions. The intensity of ray OB depends on the septal thickness that it travels through. OB may pass through several collimator septa but not just one, and the calculation of the septal thickness

Table 4.6: Symbols used in RT-MC method.

Symbol	Definition
O	point source location
A	interaction point of emitted rays and collimator front plane
B	interaction point of emitted rays and collimator back plane
γ	azimuthal angle of the emitted rays
θ	polar angle of the emitted rays
P_{OB}	path length of OB within the septal region
I_B	signal intensity at point B
I_0	the initial photon intensity
μ	linear attenuation coefficient of the collimator material at a specific photon energy
O''	the projection point of O on the collimator back plane
A'	the projection point of A on the collimator back plane
$P_{A'B}$	path length of $A'B$ within the septal region
$P_{O''B}$	path length of $O''B$ within the septal region
$P_{O''A'}$	path length of $O''A'$ within the septal region
$L_{O''B}$	length of segment $O''B$
z	source-detector distance
l	collimator length
D	equally spaced points on segment O"B
d	distance between two adjacent points D
(C_x, C_y)	center of the collimator hole
L_x	width of the collimator hole
L_y	height of the collimator hole
L_s	septal thickness
N_r	number of rays
d_p	distance between two adjacent point sources
d_μ	linear attenuation coefficient spacing

is difficult in 3D space. Therefore, we project ray OB onto the 2D space and calculate the septal thickness from the corresponding projection ray $O''B$. There are two look-up tables generated in this work. One is called pathlength lookup table (PL-LUT), which is used to record the septal thickness of each $O''B$. The number of rays and the step of B are going to be discussed. The other one is collimator response lookup table (CR-LUT). In CR-LUT, various point sources at difference source-detector distances are simulated, and several rays are traces from them to the detector. The septal thickness for each ray is calculated by searching the associated $O''B$ value in PL-LUT. The intensity of each ray is calculated by the attenuation equation. Therefore, both geometric response and septal penetration models are included in the RT generated models. The step of source-detector distance and and the step of photon energy are going to be discussed. In the following simulation, the point source is always placed along the axis through the center of a collimator hole. In practice, the size of one pixel is more larger than the collimator hole size. Therefore, this arrangement will not cause a significant error.

The fundamental idea of the RT method is shown in Fig. 4.16(a). Consider a parallel hole collimator and a point source located at the distance, z, above the collimator surface. The gray regions denote the collimator septa and the white represent the collimator hole. If a ray originating at point O passes through the gray region, it contributes to septal penetration, otherwise, it contributes to the geometric response. Simulated photons are isotropically emitted from the point source $O(O_1, \ldots, O_i, \ldots, O_n)$, thus striking onto the collimator back plane. Suppose the emitted rays interact with the collimator at point $A(A_1, \ldots, A_i, \ldots, A_n)$ on the front plane and $B(B_1, \ldots, B_i, \ldots, B_n)$ on the back plane, where the subscript i corresponds to i^{th} ray. The direction of each ray can be specified by the azimuthal angle $\gamma(\gamma_1, \ldots, \gamma_i, \ldots, \gamma_n)$ and polar angle $\theta(\theta_1, \ldots, \theta_i, \ldots, \theta_n)$. The intensity of the photons striking point B depends on the path length of OB within the septal region, as denoted by P_{OB}. It is easy to see that $P_{OB} = 0$ for geometric response (i.e., no septal penetration). The intensity at point B can be written as:

$$I_B = I_0 \exp(-P_{OB} \cdot \mu) \tag{4.12}$$

where, I_0 is the initial photon intensity (which is equal to photon history weight) at a certain photon scatter location, and μ is the linear attenuation coefficient of the collimator material at a specific photon energy (e.g., 3.12 cm^{-1} for lead at 364.5 keV.)

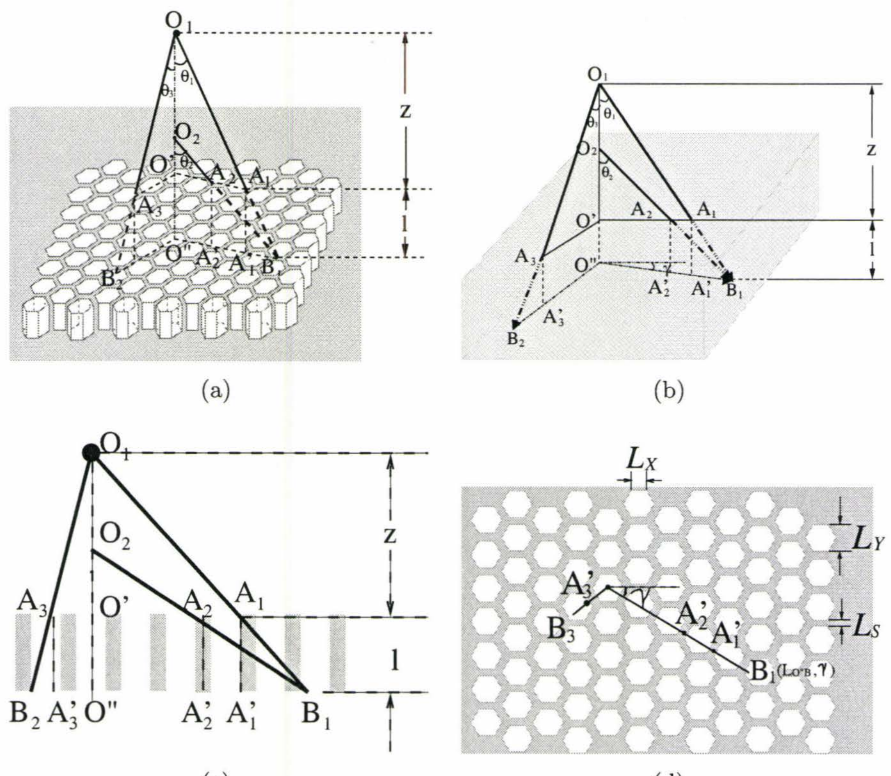

Figure 4.16: Representation of a point source above a parallel hole collimator in ray tracing method. (a) Rays emitted from point source to the collimator. (b) Simplified illustration of the ray tracing method. (c) Collimator side view. (d) Collimator top view.

Fig. 4.16(b) and Fig. 4.16(c) simplify Fig. 4.16(a) and specify two interesting ray characteristics which stress the fundamental ideas of the RT method as presented in this thesis. The first point is that the projections of rays from the source along the axis OO'' to a certain point B on the collimator are the same no matter where the point source O is located. Thus, the projection line of ray OB is always $O''B$ when point source O is moved along the axis OO''. In addition, the location of point $A'(A'_1, A'_2, \ldots, A'_n)$, which is the projection of point A, is moved along $O''B$ with respect to the movement of O, as shown in Fig. 4.16(b). The second point is that the three dimensional (3D) septal path length P_{OB} can be obtained by the calculation of the two dimensional (2D) path length $P_{A'B}$, which denotes the path length of $A'B$ in the gray region. We then have:

$$P_{OB} = \frac{P_{A'B}}{\sin\theta} = \frac{P_{O''B} - P_{O''A'}}{\sin\theta} \tag{4.13}$$

where, $P_{O''B}$ and $P_{O''A'}$ represent the path length of $O''B$ and $O''A'$ in the gray region, respectively. It is noted that Eq. (4.13) can only be used in the case of a parallel hole collimator.

If the location of B is denoted as $(L_{O''B}, \gamma)$ ($L_{O''B}$ is the length of segment $O''B$, and γ is the angle of $O''B$ away from the horizontal direction.), and defined by polar coordinates as shown in Fig. 4.16(d), the value of θ and location of point A' in Fig. 4.16 can be derived from the collimator parameters and location of the point source O. Suppose the point source is placed above the collimator at a distance z, the collimator length is l, and the angle of ray $O''A'$ in the horizontal direction is γ, the same as ray $O''B$. θ can be derived from the trigonometric functions:

$$\theta = \arctan\left(\frac{L_{O''B}}{z + l}\right) \tag{4.14}$$

where L represents the length of the segment denoted by the appropriate subscript, then $L_{O''A'}$ is:

$$L_{O''A'} = z \cdot \tan(\theta) \tag{4.15}$$

and so the position of A' can be written as $(L_{O''A'}, \gamma)$ on the polar plane.

From the above discussion, it can be seen that the intensity of photons at point B can be calculated by Eq. (4.12) using P_{OB} once the locations of B and O are known. For different O positions, the corresponding values of $P_{O''B}$ are the same but $P_{O''A'}$ is not. However, $P_{O''A'}$ may be the same for different B. The calculation of $P_{O''B}$ and $P_{O''A'}$ are significantly time consuming, therefore, it would be helpful to produce a lookup table LUT_{PL} to store the cumulative septal thickness $P_{O''B}$ and $P_{O''A}$ for a given collimator geometry. In this study, hexagonal hole parallel collimators are used, although this method is applicable for all types of parallel collimators.

Several rays are traced in the collimator back plane from center point O'' in different directions, with each ray divided into a large number of equally spaced segments denoted $D(D_1, \ldots, D_i, \ldots, D_n)$, as seen from Fig. 4.17(a). A region including a collimator hole and the surrounding septa is equally divided into n sub-regions, and the center location of each sub-region is set as the center point O''. n is a positive integer number which should at least be greater than the ratio of a projection image pixel area to a hole-septa area. In the following discussion, O'' is chosen as the center of a collimator hole as an example.

After $P_{O''D}$, the septal path lengths of segment $O''D$ are calculated and stored in LUT_{PL} together with their polar coordinates, a second lookup table consists of the resultant collimator response functions (denoted as LUT_{CR}) based upon LUT_{PL}, and is constructed by the projection images of a point source located at different distances from the collimator at a variety of photon energies. LUT_{PL} is incorporated into SIMIND MC program in order to provide additional acceleration. The following section discusses the creation of LUT_{PL} and LUT_{CR} and their subsequent implementation in CFD-MC.

The 360° circle centered at point O'' is equally divided into N_r evenly spaced radial rays, as illustrated in Fig. 4.17(a). The location of points D on the rays are

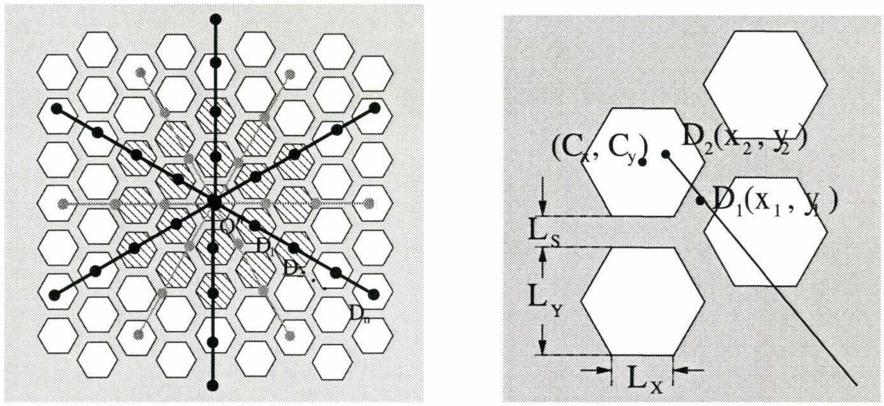

(a) (b)

Figure 4.17: Septal thickness calculation on the collimator back plane. (a) Rays on collimator back plane. (b) Schematic for checking whether point D is inside or outside a hexagonal hole.

computed to see whether they are within the septa or inside the collimator hole, which can be seen in Fig. 4.17(b).

Suppose the center of a hexagonal hole is given by location (C_x, C_y) with width and height denoted as L_x and L_y, respectively, and the distance between two adjacent points D_{i-1} and D_i is denoted as d. d should fulfill the conditions that $d \ll L_s$ and $d \ll L_y$ to minimize the error. A study of the optimal number of rays, N_r, and sampling interval, d, has been performed and is described in the next section. A given point (x, y) within the hexagonal hole should satisfy:

$$\begin{cases} |\tilde{y}| < L_y/2 \\ |\tilde{y} - \sqrt{3}\tilde{x}| < L_y \\ |\tilde{y} + \sqrt{3}\tilde{x}| < L_y \end{cases} \tag{4.16}$$

where, $\tilde{x} = x - C_x, \tilde{y} = y - C_y$. These three inequality expressions correspond to the functions of the 6 edges of the hexagonal hole. Note this equation varies with different hole geometries.

When point D is moved along a ray, it is difficult to determine into which hexagonal hole the point D is contained. With so many holes in one collimator, it is exceedingly time consuming to determine all the possible hexagons by Eq. (4.16). Rather, suppose the coordinates of point O'' is $(0,0)$, then the center distance between two adjacent vertical holes along a single column is:

$$S_y = L_s + L_y \tag{4.17}$$

and the center distance between 2 adjacent horizontal holes along a single row is:

$$S_x = \sqrt{3} \cdot S_y \tag{4.18}$$

Assuming now that the current hole is located on the 0^{th} row and 0^{th} column, (i.e., location $(0,0)$), then the coordinates for the hole centered on the n^{th} row and m^{th} column are:

$$\begin{cases} C_x = \frac{S_x}{2} \cdot m \\ C_y = \frac{S_y}{2} \cdot n \end{cases} \tag{4.19}$$

where n and m can be any integer number.

Observing the hole pattern and septal thickness, when a ray exits out of a hole and proceeds to the next hole, the second hole must always be adjacent to the first. For a practical (low/medium/high energy, general purpose/high resolution) collimator, it is usually adequate to consider only the adjacent 18 holes, as depicted by the shaded holes in Fig. 4.17(a). The number of adjacent holes should be increased only when $2L_y < L_s$, which makes the next point D, always within the septa until it gets into a new hole other than the shaded hole. Initially, we will call the current hole that D resides, the center hole, and its 18 adjacent holes as side holes.

The RT process starts with point D moving from O'' along one of the rays, with center hole (C_x, C_y) as $(0,0)$ and initial cumulated septal thickness (CST_0) as 0 cm, with the subscript 0 denoting the starting D. The previous point D is recorded as

D_{i-1}, and the current one being D_i. When D is inside the center hole (or one of the side holes), it is denoted as $D \in H_c$ (or $D \in H_s$), with D within the septa being denoted as $D \in S$. During the movement along ray $O''D$, four possibilities may occur:

- $D_{i-1} \in H_c$, and $D_i \in H_c$. This means point D_i is still within the same hole and thus $CST_i = CST_{i-1}$. The current hole is still the center hole.
- $D_{i-1} \in H_c$, and $D_i \in S$. This means D_i is moving from air to septa. $CST_i = CST_{i-1} + d$. The current hole changes from the center hole to a side hole.
- $D_{i-1} \in S$, the coordinates of D_i are required to be calculated with respect to each side hole using Eq. (4.16) to check whether it is inside one of the side holes. If $D_i \in S$, $CST_i = CST_{i-1} + d$, and the current hole is still a side hole.
- $D_{i-1} \in S$, but $D_i \in H_s$. This means D_i is moving from the septa to a collimator hole, and $CST_i = CST_{i-1}$. The center hole is renewed as the one which holds the current D_i. The current hole changes back to the center hole, and the side holes are updated.

This process is repeated until D_i goes to the end of all the rays being simulated with the CST of each position on the ray being stored in the lookup table LUT_{PL}.

Once generated, the collimator response can be calculated using the table, LUT_{PL}, by reprojecting the cumulative 2D septal thickness back to the 3D septal thickness based upon Eq. (4.13). By reading the term $P_{O''B}$ from Fig. 4.16 from the look-up table, LUT_{PL}, the polar coordinates $(L_{O''B}, \gamma)$ of B and the cumulative septal thickness, $P_{O''B}$, are determined. The coordinates $(L_{O''A'}, \gamma)$ of A' can be derived from Eq. (4.14) and Eq. (4.15), the subsequent value of $P_{O''A'}$ can be determined by searching LUT_{PL}, and P_{OB} can be determined from Eq. (4.13). Therefore, the intensity of the photon flux striking detector location B is determined by Eq. (4.12). As the detector surface is typically divided into a number of detector bins, this intensity gets added to the value of the detector bin corresponding to this location and the number of photons striking at this bin is subsequently incremented. Thus,

$$\begin{cases} V_{i,j} = V_{i,j} + I_B \\ CNT_{i,j} = CNT_{i,j} + 1 \end{cases} \tag{4.20}$$

where i and j denote the i^{th} row and j^{th} collimator bin. $V_{i,j}$ is the value of this bin, I_B is the intensity of certain photon flux on point B, as calculated from Eq. (4.12), and $CNT_{i,j}$ is the total number of photons striking this position.

This procedure is repeated for all the locations on a given ray and for all possible emission angles over 360°. Eventually, the value of each bin is normalized,

$$\widetilde{V}_{i,j} = \frac{V_{i,j}}{CNT_{i,j}} \tag{4.21}$$

In order to generate the LUT_{CR}, the point source is moved along the axis OO'' at a step of d_p and the value of μ at a step of d_μ in Eq. (4.12) is altered according to different photon energies. The sum of each resultant projection image is normalized to 1 before the image is stored in LUT_{CR} for each point source location and different μ . The projection images are usually of limited size. When the point where a ray hit the detector is one of the vertices of the projection image, the convolution kernel stored in LUT_{CR} should be able to cover all of the projection image. Therefore, the matrix size of the resultant ray-traced images should be twice that of the projection images. The reasonable sampling intervals for d_p and d_μ are analyzed in section 3.5.4.

4.5.2 Convolution-based Forced Detection Incorporating Ray-Tracing Models

Following the generation of LUT_{CR}, it was then implemented into a CFD version of the SIMIND MC program (RT-MC) [73, 74]. The conventional CFD method uses 2D Gaussian functions as the convolution model, however, RT generated models together with the intrinsic resolution model are utilized here to represent the collimator response including geometric and penetration components.

The RT generated models can be referred to in the lookup table, LUT_{CR}, for different source-detector distances and photon energies (i.e. linear attenuation coefficient μ in lead). It is not feasible to store all possible photon locations and energies within LUT_{CR}, so rather a subset of possible values is stored. For a given photon with energy E_i, at object location (x_i, y_i), LUT_{CR} is then consulted to determine the projection images that most likely match the photon energy and its scatter location. If an exact match is not found, then the most appropriate value is obtained via linear interpolation in both μ and source-detector distance.

4.5.3 Evaluation of CFD Incorporating Collimator Response Modeling

Compared to the evaluation of geometric response, the point spread function of combined geometric response (GR) + septal penetration (SP) models are not able to be modeled as Gaussian functions. The effect of GR and SP thus has to be evaluated separately. However, in most situations geometric response photons are still predominant, and so the central component of the PSF can still be fit by a Gaussian function to determine the FWHM. Because the amplitude of SP is lower than GR, the evaluation of the septal penetration component uses the full width at tenth maximum (FWTM). In the following discussion, the RT-MC modeled data has been compared with the experimental data using different types of radionuclides and collimators.

The geometry of collimator response including both GR and SP is different than the previous study. A 100MBq ^{131}I point source (a 1-cm-length and 0.5-cm-diameter pill) is placed in the air 30 cm above a GE Millennium VG camera with HEGP collimator and scanned for 5 minutes. Again, a 20% energy window (328-400 keV) is used here.

Fig. 4.18 shows the simulation results using RT-MC along with experimental data. It can be seen from Fig. 4.18(a) and Fig. 4.18(b) that the RT-MC generated image looks similar to the experimental data. Note that the RT image for the HEGP collimator has been rotated counterclockwise by 15° to match experimental results. The central dark region corresponds to the geometric response while the long tails of each image correspond to septal penetration and have been individually illustrated in Fig. 4.18(c) and Fig. 4.18(d). The image counts between two penetrated lines in Fig. 4.18(a) denotes the scatter photons, which is not simulated in Fig. 4.18(b). Septal penetration appears as a very well-known 6 sided star pattern with a second, less obvious star pattern situated 30° from the first one. This can be explained with the aid of Fig. 4.16(d). In the vertical direction (black lines), the rays at every 60° travel through the first cumulative septal thickness. The second, less intense star pattern appears offset 30° (gray lines) from the first pattern due to another thin septal thickness compared to its surroundings. Fig. 4.18(e) and Fig. 4.18(f) respectively give the linear-plot and log-plot of one tail profile to accentuate the difference between RT-MC and experimental data. The RT-MC simulation shows larger fluctuating ripples because our model lacks additional photon interactions such as collimator scatter, X-ray emission, and other interactions after the crystal.

There is an additional structure seen in the PSF images as regions of higher and lower intensity along the septal penetration tails as seen in Fig. 4.18. This can be explained from the cumulative septal thicknesses ($CST's$) stored in the LUT_{PL}. Fig. 4.19(a) plots $P_{O''B}$ in the horizontal direction for a single ray. Fig. 4.19(b) shows a magnified view of the selected region in (a), and Fig. 4.19(c) and Fig. 4.19(d) plot the septal thickness $P_{A'B}$ and P_{AB} for differing B when the point source is located 30 cm above the collimator. The CST appears as a staircase pattern, with the flat lines corresponding with point B in the collimator hole and the increasing lines associated with the points in the collimator septa. In Fig. 4.19(c) and (d), we can

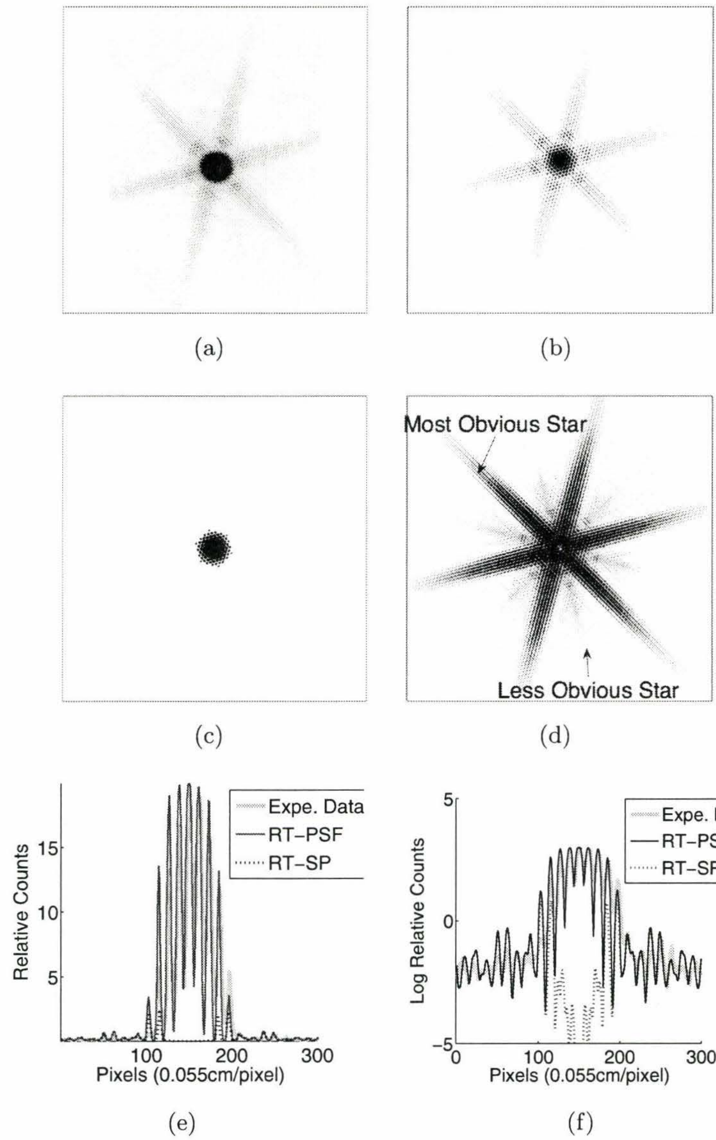

Figure 4.18: Comparison between RT-MC model and experimental result using HEGP collimator when point source located at 30 cm above the collimator. (a) and (b) compare the experimental measured data and RT-MC resultant image, which has been separated into geometric (c) and septal penetration (d) compartments. The linear and log center profiles of one tail are plotted in (e) and (f) showing the great agreement between the measured data and RT simulation. RT-PSF in the legend is the profile for RT generated PSF result, and RT-SP is the profile for RT generated SP result.

see some ripples in this pattern whereby several ripples combine to a larger packet. These ripples originate in the numerator of Eq. (4.13). The increasing portions or flat portions in Fig. 4.19(a) minus another increasing portion results in periodically appearing ripples. Between every two bumps, $P_{O''B}$ and $P_{O''A}$ moves along two flat lines and the minus term results in the slowly increasing line, which denotes the increasing azimuth angle canceling with the increase in the septal thickness. The sin term in the denominator of Eq. (4.13) flattens the septal thickness P_{AB}, but enlarges the first bump more than others because of the small photon emission angle.

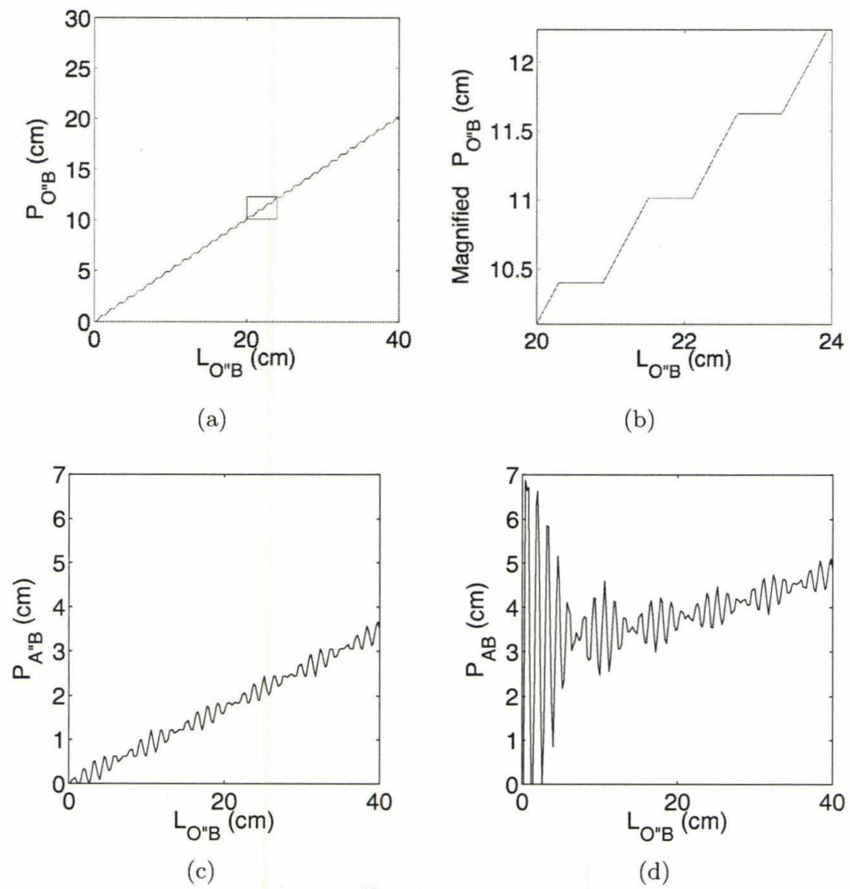

Figure 4.19: The cumulative septal thicknesses from O'' and O to point B along a ray. The x-axis denotes the location of point B away from the center O'' with the unit of cm. (a) Cumulative septal thickness $P_{O''B}$. (b) The magnified view of the block region in (a). (c) Septal thickness $P_{A'B}$ on the collimator plane. (d) The 3D septal thickness P_{AB}.

The FWHM has been introduced to evaluate the RT-MC geometric component. Because the result of RT does not include the intrinsic resolution of the detector, it is necessary to further convolve the result of RT with the camera intrinsic resolution. This has been found to consist of a $\sigma = 0.2$ cm Gaussian function for HEGP collimator using 1.6 cm thick crystal. The experimental and RT-MC generated images are further convolved with an additional $\sigma = 0.2$ cm Gaussian function, to remove the effect of the collimator hole pattern as seen in Fig. 4.18.

In the accuracy evaluation, a point source was again used here to evaluate the accuracy of RT-MC. Three collimators with the corresponding radionuclide sources were used here: HEGP collimator ($L_y = 0.4$ cm, $L_s = 0.18$ cm) for ^{131}I sources in air, together with the same evaluation for medium energy general purpose collimator (MEGP collimator: $L_y = 0.3$ cm, $L_s = 0.1$ cm) with ^{111}In in air, and low energy high resolution collimator (LEHR collimator: $L_y = 0.15$ cm, $L_s = 0.02$ cm) with ^{99m}Tc when the source is placed in air. In the RT model evaluation, we have also conducted an experiment using a 100 MBq ^{131}I point source and GE Millennium VG dual head camera with HEGP collimator. The two detectors are 58 cm apart, and the point source is placed in air. The source-detector distances to head 1 are 5 cm, 10 cm, 15 cm, 20 cm and 25 cm. The corresponding distances to head 2 are 53 cm, 48 cm, 43 cm, 38 cm, and 33 cm and 28 cm. The scan time for each distance is 5 minutes. 20% energy window (328-400 keV) is used here. Projection images were acquired at 512×512 pixels, and the pixel size is 0.11cm/pixel. The experimental setup for MEGP and LEHR collimators can be seen in Fig. 4.2, and the source-detector distances can be seen in Table 4.2. The scanning time is also 5 minutes. Projection images are acquired at 1024×1024 pixels, and the pixel size is 0.055cm/pixel. Only the data for source in air is used in this evaluation.

For the evaluation using HEGP collimator, RT-MC is applied to simulate the projection images with the same parameters as the experiment. Fig. 4.20 shows the FWHM evaluation for the geometric part of RT and experimental PSF's. It can be seen that the RT-MC simulated result is very close to the experiment. Fig. 4.20(c) shows that the simulated detector sensitivity (CPS/MBq) of RT-MC agrees well with the measured data. The amount of geometric photons is still stable as the source-detector distance varies, but the amount penetrated photons decreases when the source-detector distance increases. The total photon amount matches the real data. The evaluation of the septal penetration can be assessed using full width at tenth maximum (FWTM) [85]. Fig. 4.21 shows excellent agreement between the RT-MC models and the experimental PSF's for the penetration portion. The correlation coefficient (r^2) has then been introduced to determine how well the RT models correlate with the experimental data.

In this thesis, the discussion of septal penetration is aimed mainly for use with a HEGP collimator. MEGP and LEHR collimators, which are used for relatively low energy photons, were not considered. Therefore, the evaluation of FWHM and FWTM for MEGP and LEHR collimators only uses RT generated results (The RT generated results are not incorporated in MC simulation), but not RT-MC results. That is, the detection efficiency is not included in the evaluation. The results can be seen in Fig. 4.22 and Fig. 4.23.

Table 4.7 shows the r^2 and MSE evaluation for all these four simulations. We can see that all the correlation coefficients of the PSF's of these three collimators are greater than 0.995 except FWTM of LEHR collimator, showing that the RT models are consistent with experimental data. The MSE values for HEGP collimator are higher than the other two collimator. However, based upon the hole size and septal thickness, the simulation of HEGP is still of the most accuracy. The accuracy of FWTM for LEHR collimator is low because the number of penetrated photons is low due to the low energy photon source.

The RT models do not include photon interactions within the collimator or gamma camera. However, photon scatter within the collimator and crystal, X-ray emission, and backscatter from the materials behind the crystal can be very

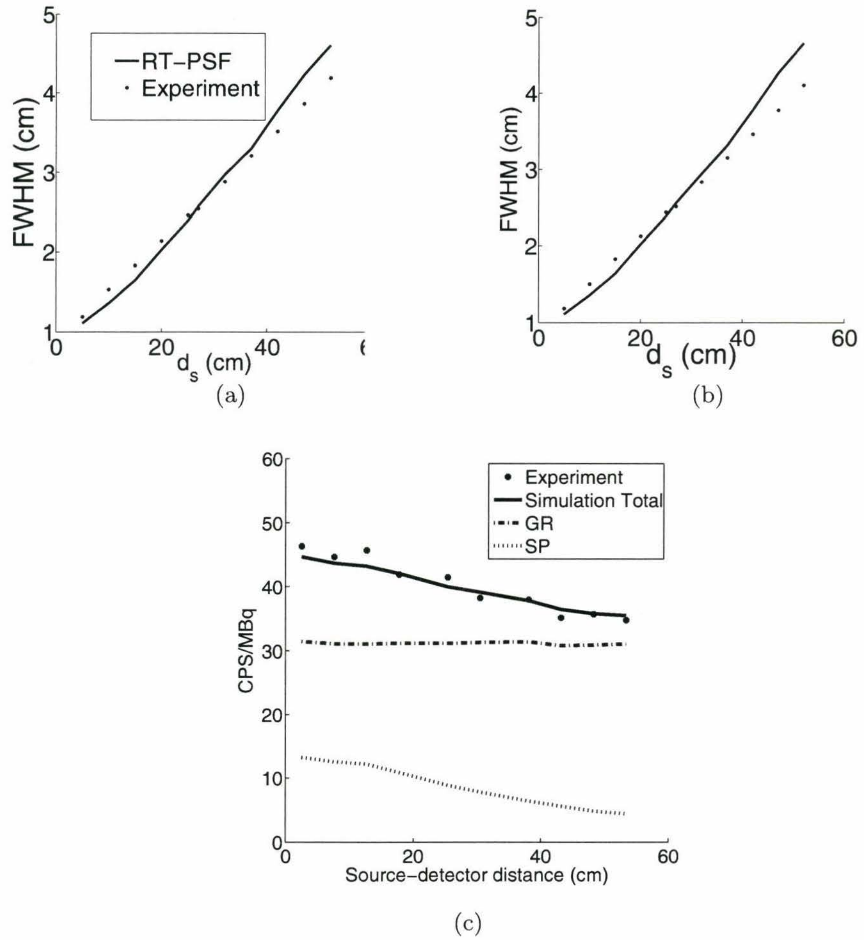

Figure 4.20: RT method geometric response and sensitivity evaluation for PSF with point source in air. (a) is the horizontal FWHM evaluation, with (b) showing the vertical FWHM. (c) presents the sensitivity of the detection based upon the detected photon counts per second for 1MBq activity.

important when medium or high energy photons are imaged. Fig. 4.24 shows the energy spectra of ^{131}I using the HEGP collimator. Solid curve in Fig. 4.24 is the spectrum when photon interaction in the detector and gamma camera is counted, and dash curve corresponds to the case that no photon interaction in the detector. It can be seen that when photons interact with the detector, some X-rays may be produced in the collimator, and some photons may be scattered from the materials behind the crystal and hit the crystal again. The number of photons in both the high energy and low energy parts of the spectrum with detector-photon interactions

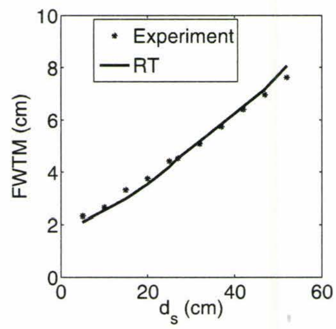

(a)

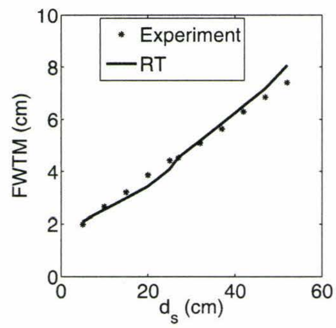

(b)

Figure 4.21: FWTM values of PSF's using HEGP collimator and ^{131}I isotope. d_s denotes the distance between point source and detector, as in the unit of cm. (a) shows the FWTM values of PSF's in the horizontal directions, with (b) plotting the vertical one.

Table 4.7: r^2 value and MSE for FWHM and FWTM measurement of different collimators. Subscript h denotes horizontal direction, with v being vertical direction. The unit of MSE is cm.

collimator	$FWHM_h$	$FWHM_v$	$FWTM_h$	$FWTM_v$
HEGP (air, r^2)	0.9976	0.9966	0.9985	0.9932
HEGP (air, MSE)	0.1699	0.2046	0.1909	0.2511
MEGP (air, r^2)	0.9954	0.9954	0.9960	0.9933
MEGP (air, MSE)	0.0774	0.1135	0.1547	0.1989
LEHR (air, r^2)	0.9956	0.9964	0.9708	0.9872
LEHR (air, MSE)	0.0407	0.0365	0.1243	0.0967

are both less than the total of non interaction photons. Photon interactions within the collimator and gamma camera affect the photons with energies lower than 200 keV much more than those with higher energies. In practice, for ^{131}I a 10% energy window centered at 364.5 keV is used, which makes the photon interactions not a significant problem. For more accurate simulation, the new SIMIND MC code developed by Ljungberg, *et al.*, which is able to simulate the photon interaction in the collimator, is recommended to be combined with the RT models [57].

In order to evaluate the speed of the RT method when implemented into the SIMIND MC program, we have simulated a $50 \times 50 \times 50$ ^{131}I block source contained within a $128 \times 128 \times 128$ voxelized air space using a HEGP collimator. Different numbers of photons have been simulated and the computation time recorded. As

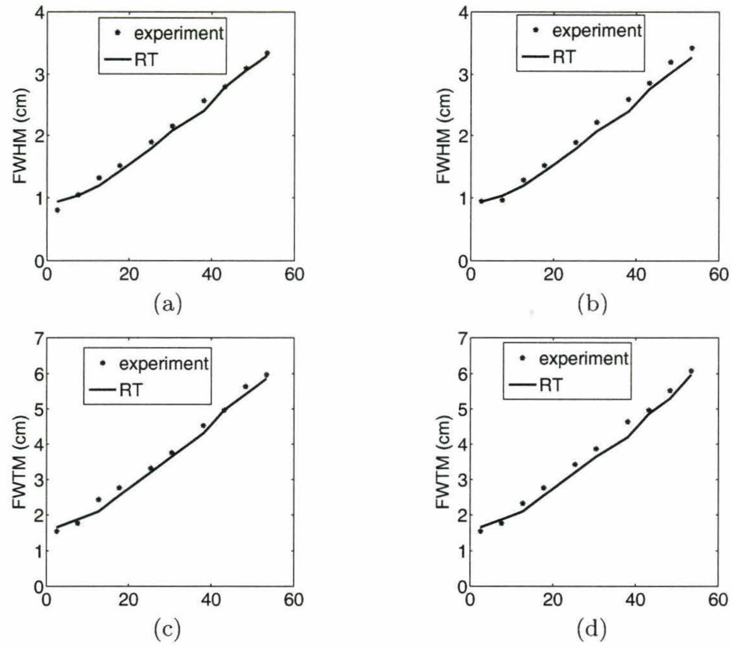

Figure 4.22: FWHM and FWTM values of PSF's using MEGP collimator and ^{111}In isotope. (a) and (b) show the FWHM values of PSF's in the horizontal and vertical directions, with (c) and (d) show the FWTM values in these two directions, where, x-axis is the distance between point source and detector.

the projection image is expected to be relatively uniform, the coefficient of variation (CV) of the center 50×50 dark region in the resulting images is calculated to measure the degree of uniformity.

Fig. 4.25 shows a plot of CV vs computation time. As seen, the RT method requires approximately 100 seconds in order to achieve a stable CV = 0.006. SIMIND forced detection MC is performed as a non-RT Monte Carlo method (non-RT MC) to compare with RT-MC. Similar to RT-MC, only geometric response and septal penetration are included in to forced detection MC simulation, and collimator scatter is not simulated.It takes the non-RT SIMIND program 1494 seconds to achieve an image with $CV = 0.03$. In order to achieve a noise free image with $CV = 0.006$, it takes the non-RT MC longer than 750,000 s (9 days) to run, indicating a speed improvement for the RT-MC of about 7,500 times. Fig. 4.26(a) and Fig. 4.26(b) shows the projection images of non-RT MC and RT-MC with $CV = 0.006$. It is

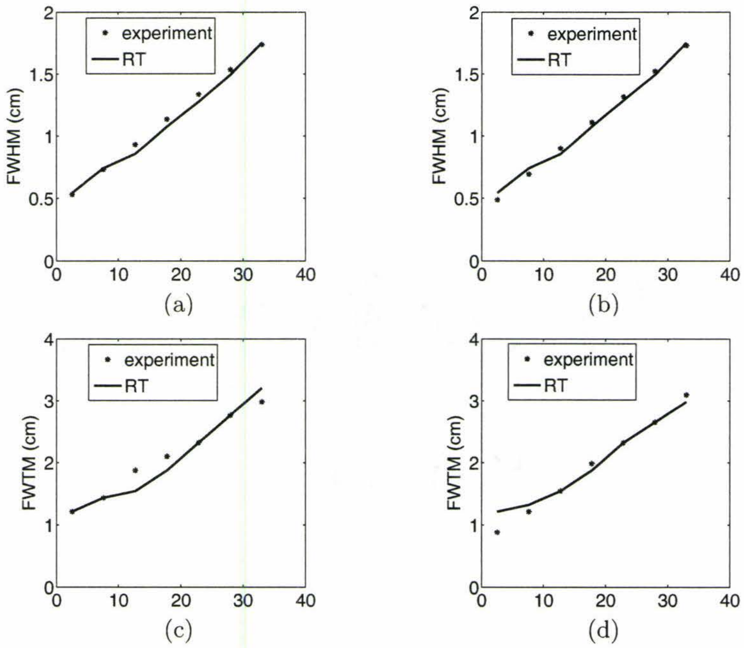

Figure 4.23: FWHM and FWTM values of PSF's using LEHR collimator and ^{99m}Tc isotope. (a) and (b) show the FWHM values of PSF's in the horizontal and vertical directions, with (c) and (d) show the FWTM values in these two directions, where, x-axis is the distance between point source and detector.

easy to see that the result of RT-MC is relatively noise free but even after 9 days simulation, the non-RT MC is not. The center regions both depict the hexagonal pattern, which is due to the geometry of the collimator. The resultant non-RT image appears somewhat sharper than RT possibly because the maximum emission angle of septal penetration rays is limited in SIMIND MC for different source-detector distances. The maximum emission angle θ in Fig. 4.16(a) is defined by Monte Carlo. In SIMIND MC simulation, when $\theta \geq \arctan \frac{O''B_{1max}}{O_1B}$, θ value is modified to be $\arctan \frac{O''B_{1max}}{O_1B}$ automatically, where O'' is the center point of the collimator. However, the photon emission angle may be greater than this maximum number when O'' is not in the center. SIMIND MC generated septal penetration is limited by this angle. Therefore, the blurring caused by septal penetration is less than the ray-tracing generated result. In SIMIND MC simulation, only one single maximum emission angle can be used for the cubic source which includes several different

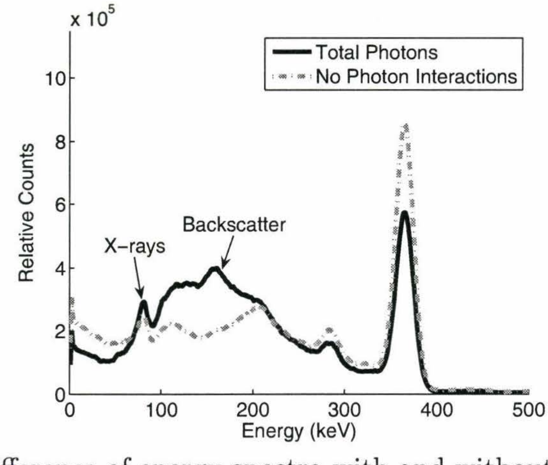

Figure 4.24: The difference of energy spectra with and without photon interactions in the detector when photons hit on the collimator and gamma camera.

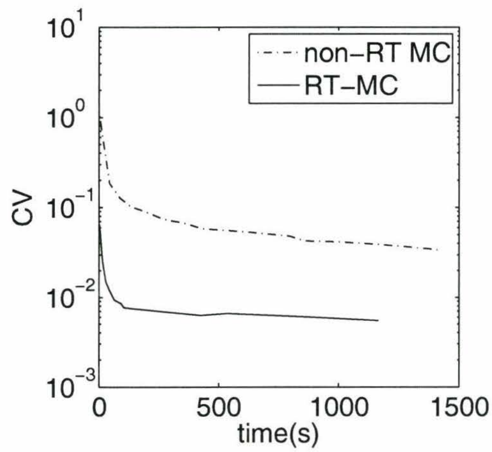

Figure 4.25: CV vs time. Solid line is the computation time of RT-MC, and dash line is computation time of non-RT MC. The computation time of RT-MC is much less that non-RT MC, and the stable noise level of it is lower than non-RT MC.

distances. This limitation will result in insufficient septal penetration photons and an overestimate of the geometric photons, which can also been seen in the linear and log center profiles shown in Fig. 4.26(c) and Fig. 4.26(d).

4.5.4 Septal Penetration Simulation Parameters

In the implementation of the RT method, it is possible to alter the number of the rays (N_r), ray step size (d), the distance between two adjacent source/detector planes (d_p) and the linear attenuation coefficient spacing (d_μ) used in the LUT_{PL} corresponding to different photon energies and LUT_{CR} lookup tables. By increasing

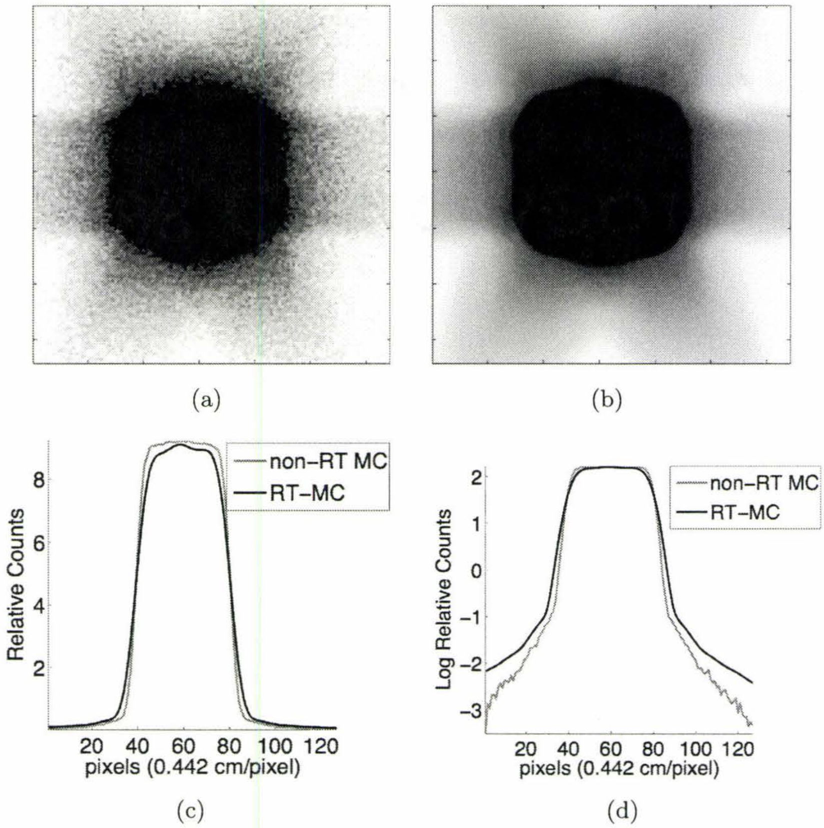

Figure 4.26: Noise-free projection images of non-RT MC and RT-MC. The projection image of non-RT MC in (a) is still not noise free even after 9 days running, comparing with the noise free projection image of RT-MC in (b). The non-RT MC resultant image looks sharper than RT-MC image might because of the rays maximum emission angle limitation of the SIMIND MC code, which results in the insufficient septal penetration photon estimation shown by the linear and log center profiles in (c) and (d).

N_r, and by reducing d, d_p, and d_μ, the resultant septal penetration model should yield higher accuracy, but at the expense of increased computation time and storage requirements for LUT_{PL} and LUT_{CR}. As such, a study of these parameters has been undertaken to determine the optimal setting in order to maintain accuracy, yet reduce computational and storage requirements. The following section discusses the appropriate parameters for HEGP, MEGP, and LEHR collimators.

An evaluation has been performed to determine the minimum N_r necessary, and the optimal d in order to minimize computer requirements while still maintaining accuracy. The CST and L_y of different collimators vary, which makes the optimal simulated parameters of each collimator different. The evaluation depends on the hole size and cumulative septal thickness. For reference, we have used projection images generated using a lookup table calculated with $N_r = 10,000$ and $d = 0.002cm$, which have shown high accuracy compared with experimental data. PSF's are modeled using reduced numbers of rays, N_r, and larger step sizes, d, have been compared to these reference images using NMSE as the evaluation criteria. The evaluation of N_r and d should be combined together. Therefore, when N_r is studied, the average value of source-detector distances in the range of 10 cm to 60 cm (10 cm intervals) with d varies from 0.002 cm to 0.15 cm is taken, and when d is studied, the same source-detector distance and N_r varies from from 500 to 10,000.

Fig. 4.27(a) shows the average value of the NMSE for the same N_r value when the point source moves from 10 cm to 60 cm in 10 cm intervals, and d is altered from 0.002 cm to 0.15 cm. Fig. 4.27(b) shows the average value of the NMSE for a same d value when the point source moves from 10 cm to 60 cm at each step of 10 cm, and N_r is altered from 500 to 10,000. Fig. 4.27(c) and Fig. 4.27(d) show the log scales of Fig. 4.27(a) and Fig. 4.27(b). We can see that d affects the result more than N_r. In fact, it can be seen that the LEHR collimator requires more precise parameters due to its thinner septal thickness and smaller hole size. Table 4.8 shows the reasonable choices for the values of N_r and d when the corresponding NMSE value gets to a stable level. For all collimators, it is seen that 1,000 rays are enough for RT simulation when the step size is set to half of the collimator septal thickness.

Table 4.8: Optimal parameters for different collimators.

Collimator	hole size L_y (cm)	septal thickness L_s(cm)	ray number N_r	stepsize d(cm)
HEGP	0.4	0.18	500	0.1
MEGP	0.3	0.1	500	0.05
LEHR	0.15	0.02	1000	0.01

As the location of an emitted photon is variable and the resultant collimator

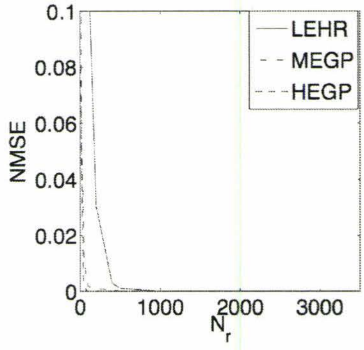

(a)

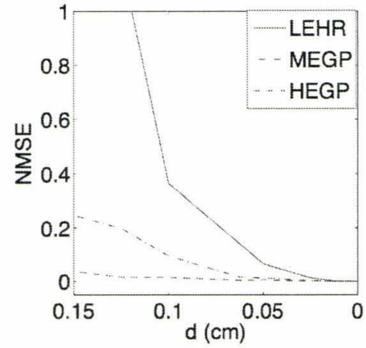

(b)

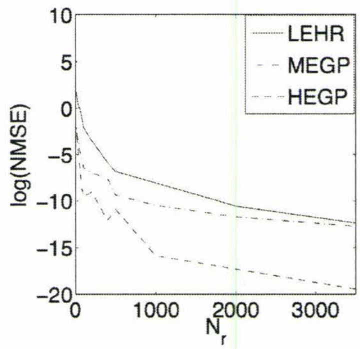

(c)

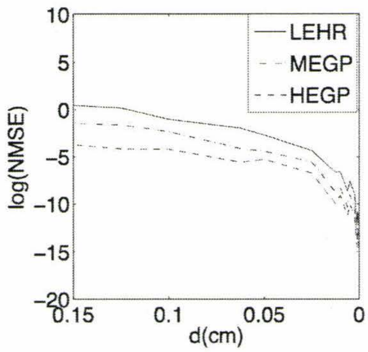

(d)

Figure 4.27: NMSE comparison of the model for the 3 collimators with the reference projection images over various N_r and d. (a) shows the effect of N_r is not very obvious, 1,000 rays is enough for simulation. (b) shows the effect of d is significant. The reasonable value is about half of the septal thickness and results in accurate modeling. (c) Log value of (a). (d) Log value of (b).

attenuation coefficient for lead varies widely as a function of energy (ranging from 1.167 cm^{-1} at 700 keV to 62.13 cm^{-1} at 100 keV), it is impossible to store all possible source location and energy combinations in the lookup table. Rather, we have implemented the LUT_{CR} for set distances from the detector surface and for set photon energies. Thus, for a given source location and photon energy, we determine the correct collimator response model via linear interpolation between the stored values. Thus, we must determine the optimal spacing for source-detector distance, d_p and linear attenuation coefficient, d_μ.

For the determination of d_p, we have simulated the PSF's for two point sources with a specified d_p. A linear interpolation is performed between these PSF's and compared to the actual PSF at that location using the NMSE. The evaluation for d_μ is performed in an analogous manner. The HEGP collimator is used in the following evaluation. As seen in Fig. 4.28, when the separation between calculated values for d_μ increases, the NMSE increases as the linear interpolation scheme is not accurate. It can generally be seen that reasonable accuracy exists in the simulated PSF even for $d_\mu = 0.5cm^{-1}$. As expected, it is seen that by reducing the plane separation, d_p, more accurate PSF's are obtained. This trend is seen to be essentially linear, thereby suggesting that the optimal plane spacing may be equal to the voxel size as simulated in the subsequent MC simulation.

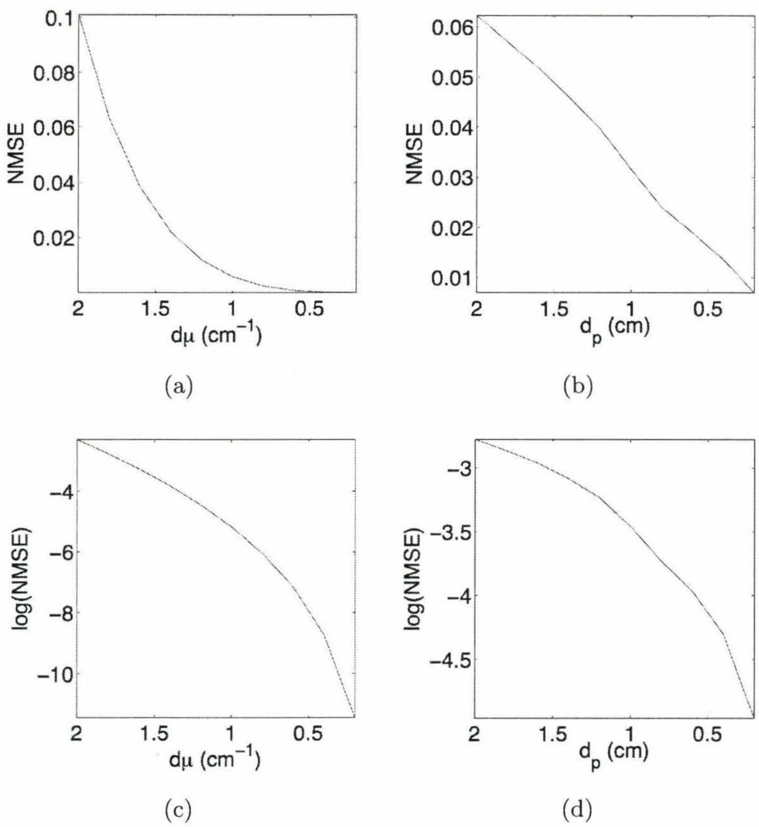

Figure 4.28: The estimation of d_p (source-detector distance step) and d_μ (linear attenuation coefficient step). (a) NMSE comparison of the interpolated images with the actual PSF at different d_μ. (b) NMSE comparison of the interpolated images with the actual PSF at different d_p. (c) Log NMSE of (a). (d) Log NMSE of (b).

4.6 Conclusion

In this Chapter, we have discussed several variance reduction techniques used to accelerate Monte Carlo modeling of photon transport. Both CFD and MP-CFD have been developed based upon the forced detection method. The RT method to model collimator response including geometric resolution and septal penetration is introduced when high energy photons are imaged. The generated models have been incorporated into CFD yielding a very flexible model that is easy to combine with other VRT's.

We have evaluated the accuracy of CFD, MP-CFD, and RT-MC for simulated photon transport. It has been assessed that the computation time of CFD is roughly 5 times faster than FD, due to the fact that the program uses an analytically determined blurring kernel rather than sampling the photon path direction from a probability density function. As a result, CFD converges to a noise-free projection image much faster than FD. The speed of MP-CFD is seen to be a further 6 times faster than CFD because the computationally demanding simulation of photon transport within the object only needs to be simulated once in MP-CFD and then forced to multiple detectors. Overall, the speed of MP-CFD is about 30 times faster than that of standard FD with similar image accuracy.

A validation of the RT method has been performed assessing the correlation coefficient for FWHM and FWTM of the point spread functions, and has shown that the ray tracing method is very accurate. When incorporated into the SIMIND Monte Carlo program, it has been shown that the speed of the ray tracing method has increased the simulation speed by a factor of 7,500 compared to the conventional Monte Carlo program. The reasonable parameters used in the lookup table for the RT method have also been determined.

In the next Chapter, image reconstruction based upon accelerated Monte Carlo is introduced.

Chapter 5

Monte Carlo based Quantitative SPECT Reconstruction

The previous chapters have introduced several variance reduction techniques used to accelerate Monte Carlo projection images of a SPECT system. Projection images obtained over all angular views do not present the 3D radioactivity distribution in a patient, as the lack of depth information in each image makes organ images overlap on projection views. The overlap depends on the structure of the organs and their locations. Thus it is difficult to determine the 3D distribution of radioactivity directly from the projection images, however this can be determined by using a number of 2D projections along with image reconstruction. Image reconstruction is a technique to solve inverse problems which estimates the input system from a set of projection views. It can recover radioactivity distribution within an object given a set of projections images obtained around the object.

Many mathematical approaches have been used to reconstruct 3D objects using projection images [86]. As discussed in Chapter 1, there are two classic reconstruction strategies that play important roles in clinical use: analytical and iterative methods. The analytical method is simple and straight-forward to implement, but it is difficult to estimate the exact quantitative activity distribution within the source object, and moreover, with this method it is difficult to improve the quality of the reconstructed images that are influenced by various degradation factors. Physical effects such as photon attenuation, scatter and collimator-detector response can greatly affect the reconstruction accuracy and estimation of the radioactivity distribution. These factors result in changes to the projection images and so the accurate modeling of these factors is essential in order to improve reconstruction accuracy. In this Chapter, we have incorporated Monte Carlo simulation into the image reconstruction process in order to accurately model the photon transport and compensate for the physical effects photons undergo.

5.1 Monte Carlo based OS-EM Reconstruction

In Monte Carlo based OS-EM reconstruction, SIMIND Monte Carlo is used to simulate the forward projections in Eq. 2.15. The degradation factors are compensated by including these models in either forward or back-projection. Attenuation and collimator response, which can be modeled prior to the simulation given a specific source-detector distance, can be included in both forward and back-projections. Scatter, however, as an unknown effect, can only be included in the forward projection through Monte Carlo. Another advantage of using Monte Carlo in the reconstruction is its ability to estimate the amount of activity present based upon the reconstructed activity distribution.

5.1.1 Image Degradation Factor Compensation

In Monte Carlo simulation, a photon event is usually combined with three factors for any photon location: photon history weight, photon direction and photon energy. The photon history weight is the probability that the photon is at a specific location with a specific direction and energy. It is initially set to unity, and is reduced as the photon undergoes various interactions.

Attenuation Correction

Attenuation is the effect of reduced signal intensity along the photon traveling direction due to photon interactions. It can be expressed mathematically by the exponential function:

$$TF(t, s', \theta) = exp(-\int_{s'}^{\infty} \mu(t, s)ds) \tag{5.1}$$

where, TF is the transmitted fraction, $\mu(t, s)$ is the linear attenuation coefficient in the object with respect to a certain location as depicted in Fig. 2.10.

In the forward projection process, before a photon is forced to the detector, accelerated MC simulates Compton Scattering and photoelectric effect, which results in μ. When the photon is forced to the detector, the photon history weight is multiplied by TF and recorded by the detector. s in the equation denotes the source-detector distance, and the exponential term denotes the probability that a photon is attenuated and is detected. In the back-projection step, each pixel value in the projection image is followed back to the 3D reconstructed object, as the value is also multiplied by TF and added into the corresponding voxel value in the object, where s now denotes the point from the projection images to the object.

Scatter Compensation

The compensation of scatter is performed in the forward projection using Monte Carlo simulation. The sampling for different photon scatter types has been discussed in Chapter 2. When a photon travels to a certain location, its scatter type, scattered energy and reflected angle are determined. The photon history weight is updated by multiplying with the probability of the photon scattering in Eq. 3.8. This scattered photon is followed until it is detected. Therefore, in the projection image, the effect of scattered photons is recorded and included in the reconstruction.

Collimator Response Compensation

As mentioned, system resolution is a combination of the intrinsic resolution of the detector and geometric collimator resolution. The intrinsic resolution refers to how precisely the scintillator and associated localization electronics can position an event to a specific location. It is normally a property of the camera and constant for a given photon energy. The collimator resolution, on the other hand, is dependent upon the collimator parameters and source-detector distances. The geometric response can be mathematically written as a 2D Gaussian function by assuming the photons are all stopped when they hit the collimator septa. However, some photons can penetrate through the thin septal walls of collimator, which is defined as septal penetration (SP). SP is also an important aspect of collimator response, especially when isotopes with high photon energy are used. The compensation of collimator response requires modeling of the collimator response during the image reconstruction process.

In the compensation, pixel (2D) or voxel (3D)-driven based forward projection and ray-driven based back-projection are applied, as shown in Fig. 5.1. In this method, the rays are traced from the emission location to the collimator. In the accelerated Monte Carlo, the photon history weight is convolved with the corresponding CR model when the photon is directed to the detector. That is, a ray is traced from a source location within the object, following the pattern of source detector resolution, to the projection plane. In back-projection (ray-driven method), several rays are traced from the collimator bin through the object. The voxel value, attenuated by the material along projection lines, is added to the corresponding point on the projection image. The cross-sections of these rays correspond to the collimator response for a certain source-detector distance. In order to simplify the reconstruction, only geometric response model is included in the back-projection.

5.1.2 Radioactivity Estimation

The value of each pixel in the projection images denotes the number of photons collected in the corresponding detector bin. The number of photons collected is related to the activity of the radionuclide. Therefore, the estimation of radioactivity

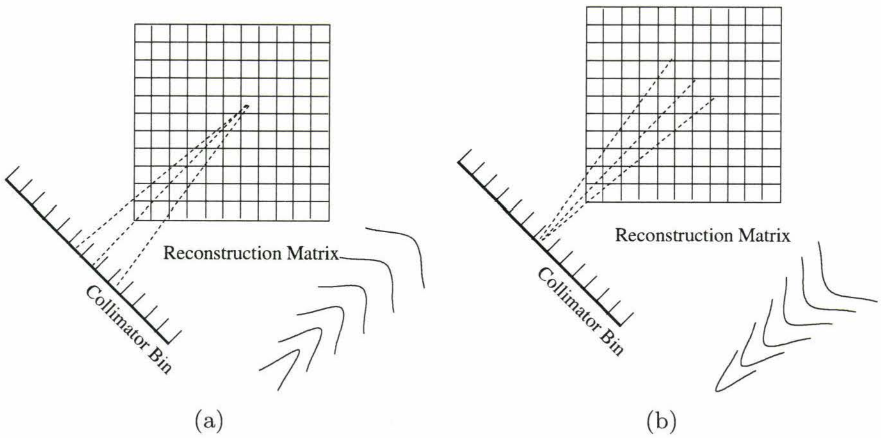

Figure 5.1: Two ways of GR compensation projection. (a) forward projection, and (b) back-projection.

is based upon the total number of photons collected in the projection image during a certain time period.

5.1.3 Summary of OS-EM Reconstruction Including Image Degradation Factor Compensation

Combining the image degradation factor compensation methods and the description of OS-EM reconstruction in Chapter 1, accelerated Monte Carlo based quantitative SPECT reconstruction consist of the following steps:

1) The reconstruction estimate starts with a uniform object, with 1 for each voxel value. The total initial object activity is set as 1 MBq.

2) In each sub-iteration, perform MP-CFD to simulate forward projection images. The angle of the first projection varies in each sub-iteration. The corresponding attenuation and scatter effect is included based upon the attenuation map used in the simulation. For the models of collimator response, when a low energy photon emitter (e.g., ^{99m}Tc) is used, only the geometric response modeled by 2D Gaussian function is included. When a high energy photon emitter (e.g., ^{131}I) is used, both geometric response and septal penetration modeled using the ray-tracing method is applied.

3) The corresponding measured projection images are compared with the simulated projections. Their ratios are determined and back-projected. When attenuation compensation is applied, it is included in the back-projected rays through TF in Eq. 5.1. The collimator response compensation can be seen in Fig. 5.1(b).

4) The 3D back-projected image of the image ratio is multiplied by the previous reconstructed object and the estimated activity is determined (see below).

5) The activity is estimated in each sub-iteration of OS-EM. The total object activity present in the initial iteration is set as 1 MBq. In each sub-iteration, the total number of photons collected in the simulated projection images is recorded and compared with the actual number of collected photons in the real projections. The total radio-activity is updated by multiplying the old activity value with the ratio of the true total photon number to the simulated total photon number. The OS-EM reconstructed object corresponds to the radioisotope concentration with the unit of Bq/voxel. The radioactivity distribution is obtained by distributing the total activity to each voxel based upon the concentration distribution.

6) Repeat the above procedure over the remaining angles, recording the average error between the true images and simulated images. If the error is above a certain threshold, ϵ, and the iteration number has not reached the maximum number, go back to step 2), otherwise, the simulation is stopped, and the current reconstruction image and the activity are set as the final result.

5.2 Evaluation

In the evaluation of accelerated Monte Carlo based quantitative reconstruction, different radionuclides (eg. ^{99m}Tc and ^{131}I) have been evaluated. The energies of the emitted photons from these radionuclides are different, and so is the collimator response. Therefore, different collimators are utilized corresponding to different photons with various energies.

In the simulation, simple source phantoms such as spheres, cylinders and phantoms with a uniform attenuation map were utilized to evaluate the accuracy of the reconstruction process, followed by more complicated phantoms, such as the NCAT phantom with non-uniform attenuation map.

Projection images were acquired by MP-CFD incorporating either geometric response models or geometric and septal penetration models. The simulated scanning time for each projection was set as 15 seconds by default.

The OS-EM method was applied to reconstruct the radioactivity distribution within the object using MP-CFD as the forward projector. The evaluation of attenuation and scatter compensation was performed first, followed by the collimator response evaluation. GR compensation does not use Monte Carlo simulation as the forward projector, so it is discussed in the Appendix.

By default, simulated objects of $128 \times 128 \times 128$ voxels were used unless specified. The voxel size was 0.442 cm, and the closest distance between the object and detector was set as 2 cm. 20% energy window was used for different radioisotopes. 120 projections were obtained over 360° for 15 s/view. In reality, 15 seconds may be short, and some noise can be seen on the projection images. However, noise free images are assumed in this thesis and no Poisson noise will be added externally. Images are reconstructed using OS-EM method with 5 iterations and 4 projections/subset.

A drawback of the simulation is the projection data is simulated using the same MP-CFD simulation code as used in the reconstruction. This may not provide a reasonable prediction of how precise this method is but rather may provide a "best-case" scenario. However, due to the time limitation, we did not do experiments or use other Monte Carlo simulation tools to generate the measured images.

5.2.1 Attenuation and Scatter Compensation

Prior to the evaluation of attenuation and scatter compensation, the fraction of attenuated photons in a cylinder phantom is studied. A 15-cm-diameter sphere source filled with 100 MBq ^{99m}Tc was simulated at the center of a 21 cm diameter and 38 cm high cylinder shown in Fig. 5.2. Convolution-based forced detection Monte Carlo (CFD-MC) was used to collect photons when the cylinder was filled with air or water, respectively. A 20% energy window was used with the lower/upper limits of 126/154 keV with a LEHR collimator. The simulated acquisition time was 15 seconds. When the cylinder was filled with air, a total of 1.5×10^5 photons were collected. When the cylinder was filled with water, there were about 1.0×10^5 photons counted. Therefore, about 33% of the photons are attenuated in this case.

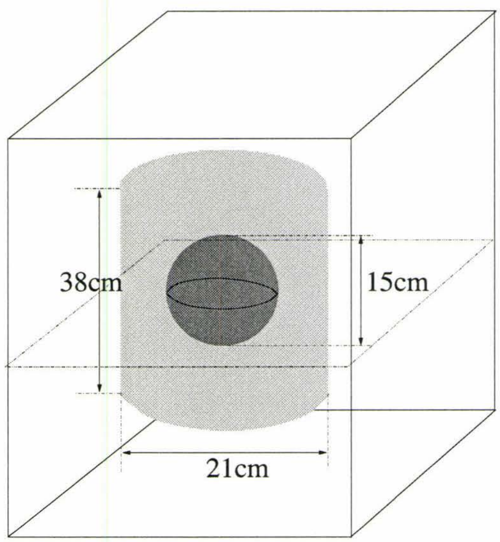

Figure 5.2: Hot spheres filled with ^{99m}Tc in the cylinder phantom. The total activity in the sphere is 100 MBq.

In the evaluation of attenuation compensation, a 15-cm-diameter sphere, filled with a uniform concentration of 100 MBq ^{99m}Tc, was centered in the same cylindrical phantom in Fig. 5.2, filled with non-radioactive water. Noise-free projection data has been simulated at 120 projection angles around the sphere over 360° by MP-CFD simulating a GE Millennium VG camera with LEHR collimators. The effects of attenuation, scatter and geometric response are included in the simulation.

Reconstruction: The OS-EM algorithm is used to reconstruct the 3D activity distribution. Two different reconstruction images are generated, one is with attenuation and scatter compensation, and the other one without. In the compensated reconstruction, the water cylinder in Fig. 5.2 was used as the attenuation medium and attenuation compensation is also included in the back-projection. In the uncompensated reconstruction, no attenuation or scatter compensation was included. In both methods, MP-CFD was used as the forward projection, and geometric response compensation was included. The activity estimation for both methods was based upon the corresponding simulated images with or without attenuation and scatter compensation.

Result: Five iterations were used for both reconstructions, the total activity estimated by the uncompensated result is 69.0 MBq, with the compensated result yields 99.5 MBq, which is close to the true activity. These results match the fact that about 33% of the emitted photons are attenuated as they travel through the cylinder.

Fig. 5.3 shows the uncompensated and compensated result. The central profiles of the reconstructed results shown in Fig. 5.3(c) further denote that the estimated activity without compensation is much lower than the true activity. The ripples shown in the reconstructed profiles is called Gibbs ring artifact, which is caused by incomplete spatial frequency sampling as a result of geometric response compensation. For more detail, please refer to Appendix A.

5.2.2 Collimator Response Compensation

In Monte Carlo simulation, a collimator should always be included to limit the detected photon traveling direction, therefore, it is impossible to compare the effect of geometric response compensated reconstruction and uncompensated reconstruction using MC simulation. Appendix A shows the effect of geometric response compensation reconstruction using the analytical method. In this section, the effect of septal penetration compensation is discussed.

In this simulation, four different sized spheres (diameters of 6 cm, 7.5 cm, 9

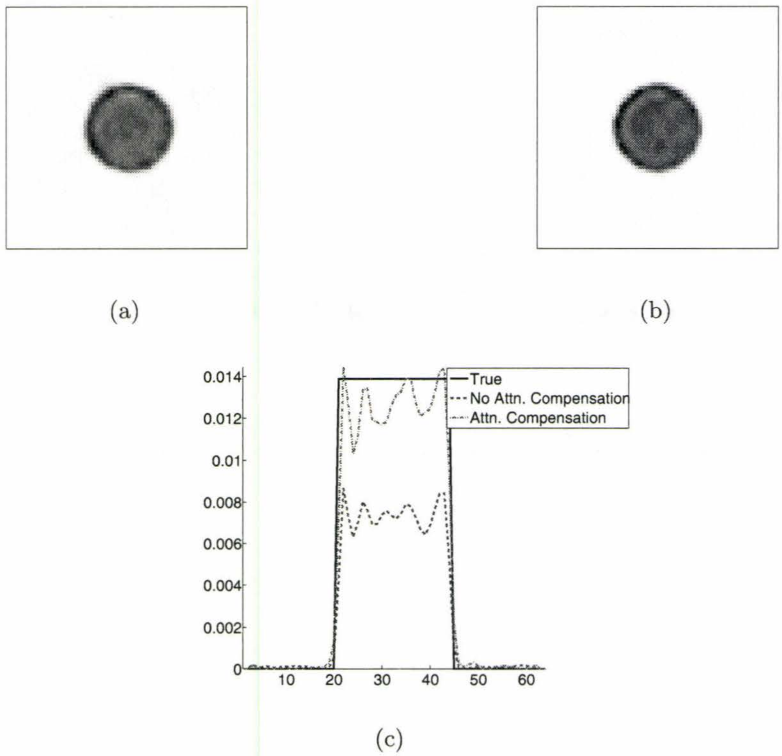

Figure 5.3: The assessment of attenuation and scatter compensation using the central slice of the resultant images. The uncompensated result in (a) is compared with compensated result in (b). The center line profiles of these three images are plotted in (c).

cm, and 10.5 cm, respectively) were filled with ^{131}I and placed in: i) air, ii) water without activity, and iii) cylindrical phantom filled with water containing 100 MBq activity, as seen in Fig. 5.4(a). The total activity of these four spheres was 100 MBq, and the activity for each individual spheres can be seen in Table 5.1, Table 5.2 and Table 5.3. In the simulation of ii) and iii), the diameter of the cylinder was 56cm and the height was also 56cm.

In the simulated acquisition, 120 projection images were generated by MP-CFD over 360° using an HEGP collimator with 15s/view. The convolution models in MP-CFD includeed geometric photons and penetrated photons which are determined via the ray-tracing look-up table. For a collimator, the fraction of penetrated photons varies as the source-detector distance changes. It can be seen in Fig. 4.11 that the further the source is from the detector, the fewer number of penetrated photons. For head 1, when the source is close to the collimator, the ratio of penetrated photons to geometric photons is about 1:2, however, when the source detector distance is about 20 cm, the ratio is 1:10. The amplitude of penetration response is much lower than the geometric response, as shown in Fig. 4.18. However, the amount of penetrated photons is still high because they are spread around all the area of the entire camera area. It has been verified by Frey, et. al. that when the an ^{131}I point source is at 10 cm from the HEGP collimator, the ratio of penetrated photons to geometric photons is about 0.7:1 [87], and Autret, et. al. has used Monte Carlo simulation to show that the ratio is about 1:2 when the source is at 20 cm from the collimator [88]. It is noted that these ratios are both higher than the corresponding value of our simulation likely because some penetrated photons are counted in the term $\left(l - \frac{2}{\mu}\right)$ of Eq. 4.6. When RT generated models are utilized, this will not be a problem. It is very difficult to determine the ratios of the amount of penetrated photons to geometric photons for different source-detector distances using experimental data. In our simulation, the ratio of total penetration photons to geometric photons is set as 3:5 when source-detector distances are over a range of [0, 100] cm at a step of 5 cm. The total number of geometric photons in the LUR_{CR} was simply summed together for distances in the range of [0,100] cm, as is the number of penetrated photons. The number of penetrated photons was scaled to match the ratio of 3:5.

Reconstruction: The OS-EM method was again used for both SP compensated and uncompensated image reconstruction. MP-CFD was utilized in the forward projection to simulate the SPECT acquisition. In SP compensated reconstruction, the convolution kernels used in MP-CFD were derived from the GR+SP models in the ray-tracing look-up table, but only GR models were included in the back projection. In uncompensated reconstruction, only GR models were applied. In both reconstructions, photon attenuation and scatter were included (they are negligible when the cylinder is filled with air). 5 iterations with 4 projections/subset were performed to generate the reconstructed image. The total activity still started with 1 MBq and was updated at every sub-iteration.

Result: Fig. 5.4(b) presents the central slices of the GR-only compensated reconstructed images for case i), and Fig. 5.4(c) shows the results for GR+SP compensation. The resultant spheres in both cases look similar, as each shows very obvious Gibbs ring pattern, which is discussed in Appendix A. Fig. 5.4(d) shows the line profile of Fig. 5.4(b) and Fig. 5.4(c). It is seen that the reconstruction result of the uncompensated reconstruction (GR only) is very close to the SP compensated (GR+SP) result.

Table 5.1: Summary of simulation results for 4 hot spheres containing ^{131}I in air for both SP compensated and uncompensated reconstruction methods.

	True Activity (MBq)	GR-SP(MBq)	Error-GR-SP (%)	GR(MBq)	Error-GR (%)
Sphere 1	2.40	2.26	5.63	2.26	5.79
Sphere 2	10.04	9.51	5.35	11.01	9.65
Sphere 3	27.67	27.81	0.50	33.53	21.16
Sphere 4	59.89	59.84	0.09	72.81	21.58
Total of Spheres	100	99.41	0.59	119.61	19.61
Volume Total	100	102.18	2.18	164.00	64.00

The estimated activities of these two methods are denoted in Table 5.1. The total activity of 102.18 MBq as estimated by GR+SP compensation is close to the actual value of 100 MBq, but the activity of 164.00 MBq estimated by GR-only compensation is much higher than the actual value. This overestimated activity fraction (64%) matches the ratio of penetrated to geometric photons (3:5).

It is seen that the spheres within the GR+SP compensated result contain most of the estimated activity. In contrast, the GR compensation result depicts slightly higher sphere activity estimation. The total overestimated activity is about 19% higher, however, most of the overestimated activity is estimated in the background. In the GR+SP compensated result, the more activity the spheres contain, the more accurate the activity estimation. Without SP compensation, the estimation of sphere 1 is close to the actual amount, but the errors of sphere 3 and sphere 4 are high, by about 20%. The activities within sphere 2, sphere 3 and sphere 4 are all overestimated because of the lack of SP compensation. The penetrated photons from the source contained in sphere 1, 3 and 4 may be detected in the same location as geometric photons from sphere 2. Without SP compensation, the penetrated photons are considered as photons originating from sphere 2, and the same reason for the overestimated activity in sphere 3 and sphere 4. The sphere 1 is underestimated, presumably due to low activity and small volume. In this simulation, the computation time for each iteration is about 2 hours on a single 2.4GHz Linux PC.

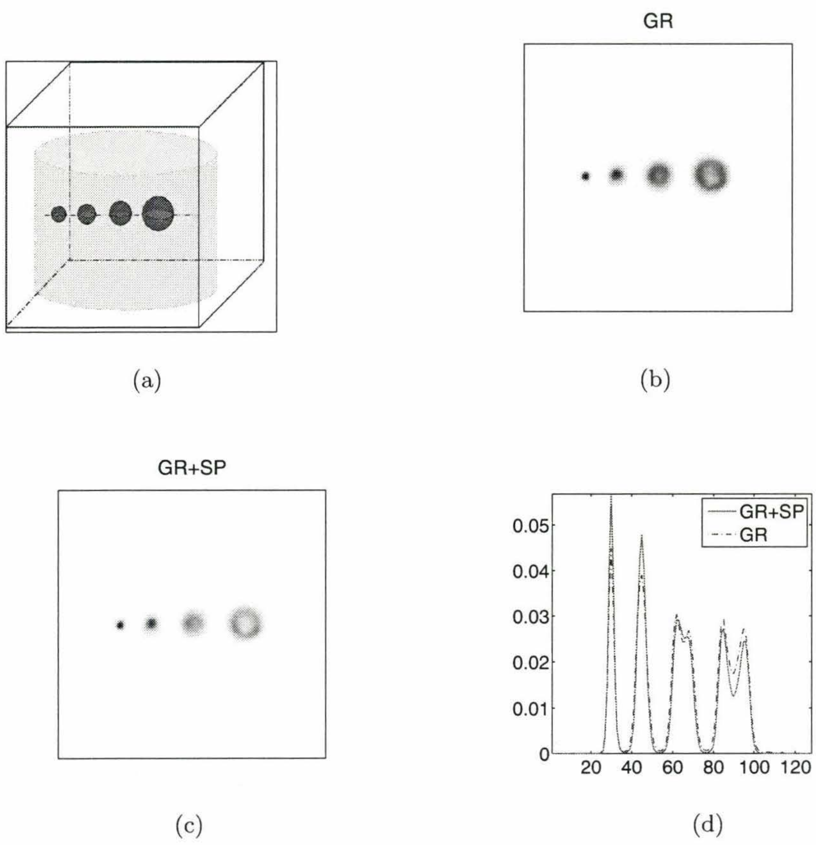

Figure 5.4: Reconstruction images of spheres placed in the air. (a) is the experimental set-up. (b) and (c) are the resultant central images of GR+SP compensation and GR compensation, respectively. The center line of both methods are shown on (d). x-axis denotes the pixel number, and y-axis is the relative activity.

Quantitative accuracy of the reconstructed spheres in air is mostly related to the accuracy of the underlying GR and SP models. When these spheres are placed in water, the estimation not only depends on the GR and SP models, but also on the accuracy of attenuation and scatter compensation. Table 5.2 and Table 5.3 illustrate the estimation result of spheres sitting in a water cylinder without or with background activity, respectively. Similar to the previous simulation, the radioactivity estimation for each sphere is close to the actual activity for GR+SP compensation. However, the estimated background activity estimation with GR-only compensation is much higher than that of GR+SP compensation. Most of the spheres are overestimated when SP compensation is not included, especially in the case when the background cylinder contains activity, as seen in Table 5.3.

Table 5.2: Summary of simulation results for 4 hot spheres containing ^{131}I in the no activity water cylinder for both SP compensated and uncompensated reconstruction methods.

	True Activity (MBq)	GR-SP(MBq)	Error-GR-SP (%)	GR(MBq)	Error-GR (%)
Sphere 1	2.40	2.25	6.07	2.22	7.31
Sphere 2	10.04	9.16	8.77	9.92	1.26
Sphere 3	27.67	27.82	0.55	28.89	4.40
Sphere 4	59.89	59.67	0.36	62.54	4.43
Total of Spheres	100	98.91	1.09	103.57	3.57
Volume Total	100	99.53	0.47	150.05	50.06

Table 5.3: Summary of simulation results for 4 hot spheres containing ^{131}I in the 100 MBq activity water cylinder for both SP compensated and uncompensated reconstruction methods.

	True Activity (MBq)	GR-SP (MBq)	Error-GR-SP (%)	GR(MBq)	Error-GR (%)
Sphere 1	2.40	2.71	12.81	2.97	23.74
Sphere 2	10.04	10.01	0.28	12.02	19.69
Sphere 3	27.67	26.86	2.92	34.13	23.35
Sphere 4	59.89	59.58	0.51	72.16	20.49
Total of Spheres	100	99.17	0.83	121.28	21.28
Volume Total	200	198.96	0.52	317.80	58.90

It can be seen from these three simulations that most of the overestimated activity appears in the background but not within the spheres themselves in the absence of SP compensation. This is because the traveling path of the penetrated photons are always different than the geometric photons. When GR-only models are utilized, only the geometric photons are considered to be emitted from the actual source, and the penetrated photons are considered to be emitted from the background. In theory, the activity estimation of the background is overestimated because of the uncompensated penetrated photons, and the estimation of the four spheres should be underestimated because of the lack of penetrated photons. However, the penetrated photons from one sphere will be recorded by the projection location corresponding to other spheres and result in the overestimation of activity in these spheres. In these two simulation, the computation time is about 4 hours/iteration on a single 2.4GHz Linux PC. The time is longer than the previous study because of the calculation of attenuation and scatter.

5.2.3 Realistic Phantom Simulation

Simulation: In order to evaluate the accuracy of the proposed MC-based reconstruction technique under more realistic situations, a $64 \times 64 \times 64$ voxel NCAT phantom with pixel size of 0.884 cm has been used. This phantom contains representative heart, liver, lung and kidney, with realistic soft tissue attenuation. 100 MBq of ^{131}I was simulated in the phantom. The activity of each phantom organ can be seen in Table 5.4.

60 projections were simulated over 360° by MP-CFD using a HEGP collimator with 15s/projection. Photon attenuation, scatter, GR and SP were all included in the simulated projections.

Reconstruction: For evaluation of the performance of physical correction methods, the OS-EM algorithm has been utilized to reconstruct the projection images using three different compensation models:

1) with all the compensation factors (GR+SP, scatter and attenuation);

2) with collimator response compensation but without attenuation and scatter compensation (GR+SP);

3) with all the compensation factors except SP modeling (GR, scatter and attenuation).

HEGP collimator is used in the MP-CFD to simulate the collimator response. In Method 1 and Method 3, the NCAT attenuation map is applied, and in Method 2, no attenuation map is used.

Results: Table 5.4 depicts the quantitatively reconstructed radioactivity estimation using the three methods. It can be seen that the total activity estimation using Method 1 is close to the actual value, Method 2 is underestimated, and Method 3 is overestimated.

Table 5.4 also shows activity estimation for four organs: heart, liver, lung and kidney. Method 1 shows a good agreement with true activities for all organs and background. The activity generated by Method 2 appears to be 10% underestimated. The activities for all the organs estimated by Method 3, without SP compensation, are all overestimated.

The overall accuracy of this realistic NCAT phantom study is somewhat lower than the previous sphere study. The biggest difference between this study and the previous hot sphere study is the complexity of the attenuation map. The non-uniform attenuation map of the NCAT phantom appears to make the Monte Carlo based estimation slightly less accurate than simple uniform maps. This maybe due to the error in MP-CFD method itself.

Fig. 5.5 shows different slices of the reconstructed NCAT phantom corresponding to the cross sections denoted in Fig. 5.5(a). The difference between these three methods is not very significant. It is seen that the result of Method 3 is closer to the real image than Method 1. This may because the background activity in Method 1 is underestimated, which makes it less obvious than the overestimated background in Method 3. Due to the complicated simulation of NCAT phantom, one iteration

Table 5.4: The reconstruction result of NCAT phantom with different compensation models. Method 1 is the reconstruction including all the compensation models, Method 2 does not include attenuation/scattering, and Method 3 does not include septal penetration. The bottom row is the activity estimation of body total.

Organ	True Activity (MBq)	Method 1		Method 2		Method 3	
		Activity (MBq)	Error(%)	Activity (MBq)	Error (%)	Activity (MBq)	Error(%)
heart	12.37	11.48	7.19	9.80	20.76	14.86	20.11
liver	51.98	52.76	1.50	43.65	16.01	63.00	21.21
lung	11.30	12.75	12.83	11.10	1.75	17.60	55.73
kidney	14.85	13.07	12.00	10.83	27.02	16.72	12.60
Phantom total	100.00	103.97	3.97	88.26	11.74	156.69	56.69

takes about 10 hours on a single 2.4GHz Linux PC.

5.3 Conclusion

In this chapter, OS-EM incorporating a Monte Carlo based forward projector has been used to reconstruct SPECT projection images. Compensation for image degradation factors are included in the reconstruction to improve the quality of the reconstructed result using accelerated MC simulation.

The accuracy of image reconstruction for different compensation methods is studied, and their effect on activity quantitation is evaluated. Attenuation and scattering tends to reduce the estimated activity of the reconstructed object. The effect of septal penetration compensation is very significant for high energy radioisotopes such as ^{131}I. Even though the high energy collimator is used to reduce this effect, quantitation errors are still high due to penetration when not compensated. The NCAT phantom has been used to further evaluate the compensation effect using accelerated MC. It can be seen that the activity estimation for uniform objects is more accurate than non-uniform objects. In next chapter, accelerated Monte Carlo based OS-EM reconstruction will be applied to simultaneously acquired dual-isotope projection images and estimate the activities for the two radioisotopes.

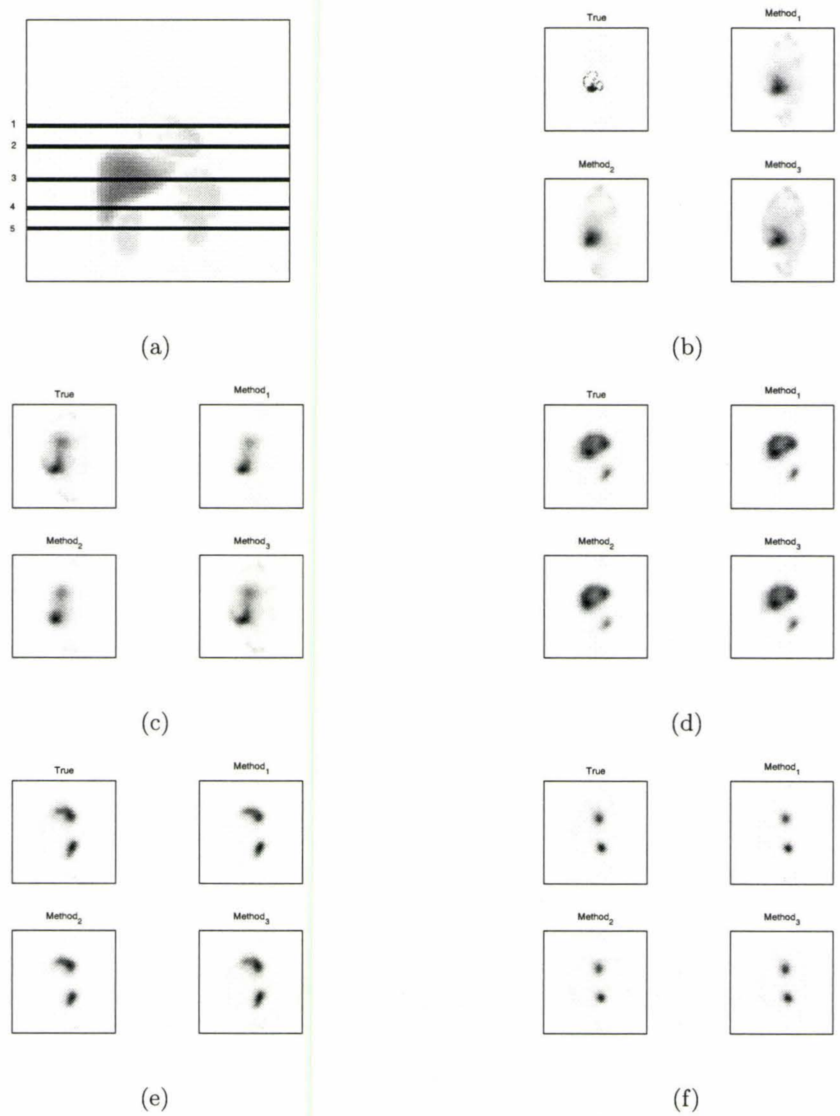

Figure 5.5: Quantitative estimation result of NCAT phantom. (a) shows the anterior view of the phantom and the interested organs. Lines 1-5 correspond to the tomography slice views of (b)-(f).

Chapter 6

Dual Isotope Reconstruction

6.1 Introduction

Some nuclear medicine procedures may require the patient to undergo multiple exams using different radionuclides with different emission energies. When the different radionuclides are scanned separately, patient movement during the scanning will result in misregistration of the reconstruction images. Dual-isotope imaging may be performed simultaneously however in order to obtain perfect spatial registration. Another benefit of the simultaneous multi-isotope imaging is a reduction in scanning time, which improves patient comfort and convenience. In simultaneous imaging, the projection views are acquired under the identical conditions of patient position, using the same camera orbit.

In a dual-isotope SPECT study, two radio-pharmaceuticals are each labeled with a different isotope, and can be applied to some clinical applications such as myocardial imaging and brain imaging [42]. Two possible dual isotope applications are $^{99m}Tc/^{201}Tl$ and $^{99m}Tc/^{123}I$ emission scintigraphy in myocardial imaging and preoperative parathyroid tumor scanning [89–93].

If both images in a dual-isotope scan are obtained simultaneously after the injection, the projection images may be contaminated, as a result of the contribution of scattered photons from the other isotope. The primary limitation of simultaneous dual isotope acquisition is the crosstalk of the photons from a higher energy of one radionuclide to the other lower energy window, as seen in Fig. 6.1. The crosstalk contamination is more serious when the two energy photo-peak windows are closer in energy, as seen in Fig. 6.1(b) [42].

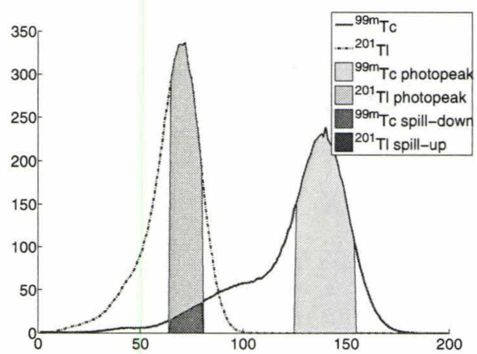

(a)

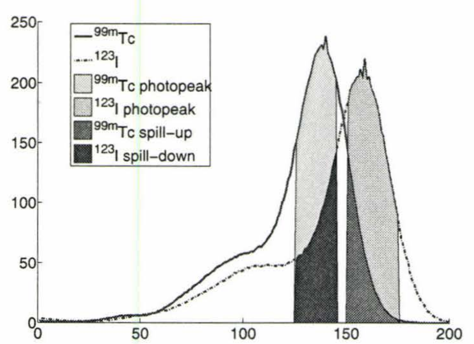

(b)

Figure 6.1: The spectra used in the dual isotope reconstruction code evaluation. (a) shows the spectra for $^{99m}Tc/^{201}Tl$. The high energies (135 + 165 keV) for ^{201}Tl are not included in the simulation. Therefore, the projection images generated by ^{99m}Tc would not be affected by ^{201}Tl. However, because of the photon down-scatter and the produced X-rays when high energy ^{99m}Tc photons interact with the collimators, ^{201}Tl produced images are affected by ^{99m}Tc. (b) shows the spectra for $^{99m}Tc/^{123}I$. The high energy emission (248 to 784 keV) for ^{123}I is not include, but the cross-talk photon number is significant for both.

Several methods have been applied to reduce the effect of cross-talk. A common method of cross-talk correction is using the ratio of the number of photons collected within each of the two energy windows [94–97]. The crosstalk fraction is calculated from the experimental energy spectrum or MC simulation prior to the correction. The correction is performed by excluding the cross-talk component in one energy window from the other one. However, this method is limited by estimation accuracy of the cross-talk photon fraction.

In the work of de Jong et. al [98], the photon behavior is modeled by Monte Carlo based simulation. A down-scatter point spread function is generated by rotation-based MC simulation and included in the reconstruction. Moore et. al [99], has incorporated de Jong's model to decouple the projection image from the crosstalk photons. Ouyang et. al [100] has developed a joint iterative reconstruction method to compensate for the cross-talk photons. However, the estimation of scatter photon models was independent of Monte Carlo simulation. In this work, we have combined our accelerated MC-CFD method with the joint iterative reconstruction method to compensate for the cross-talk photons.

6.2 Dual Isotope Reconstruction Method

We have developed a method using accelerated MC based OS-EM technique to reconstruct dual-isotope projection images, accounting for the spillover from one energy to another.

In a dual isotope acquisition, two sets of projection images corresponding to the two isotope's photopeak windows are :

$$\begin{cases} A_x f_x + A_x f_y = p_x \\ A_y f_y + A_y f_x = p_y \end{cases} \tag{6.1}$$

The subscripts x and y denote that the projections are based upon the photopeak energy windows of the two isotopes. A_x and A_y are the projection matrices in the two corresponding photopeak energy windows, f denotes the radiotracer distribution for each isotope while p represents the projection for each isotope.

From Eq. 6.1, it is seen that the photons emitted from one photopeak window can not only be detected in its own photopeak window, but also in the photopeak window of the other isotope. These cross-talk photons reduce the quality of the projection images. Based upon Eq. 2.14, the updating function of dual-isotope reconstruction can be written as:

$$\begin{cases} f_j^{x,new} = \frac{f_j^{x,old}}{\sum_i A_{x,ij}} \sum_i A_{x,ij} \frac{p_{x,i}}{\sum_k A_{x,ik}\left(f_k^{x,old} + f_k^{y,old}\right)} \\ f_j^{y,new} = \frac{f_j^{y,old}}{\sum_i A_{y,ij}} \sum_i A_{y,ij} \frac{p_{y,i}}{\sum_k A_{y,ik}\left(f_k^{y,old} + f_k^{x,old}\right)} \end{cases} \tag{6.2}$$

The flow chart of dual-isotope reconstruction method can be seen in Fig. 6.2. The reconstruction steps of dual-isotope reconstruction are:

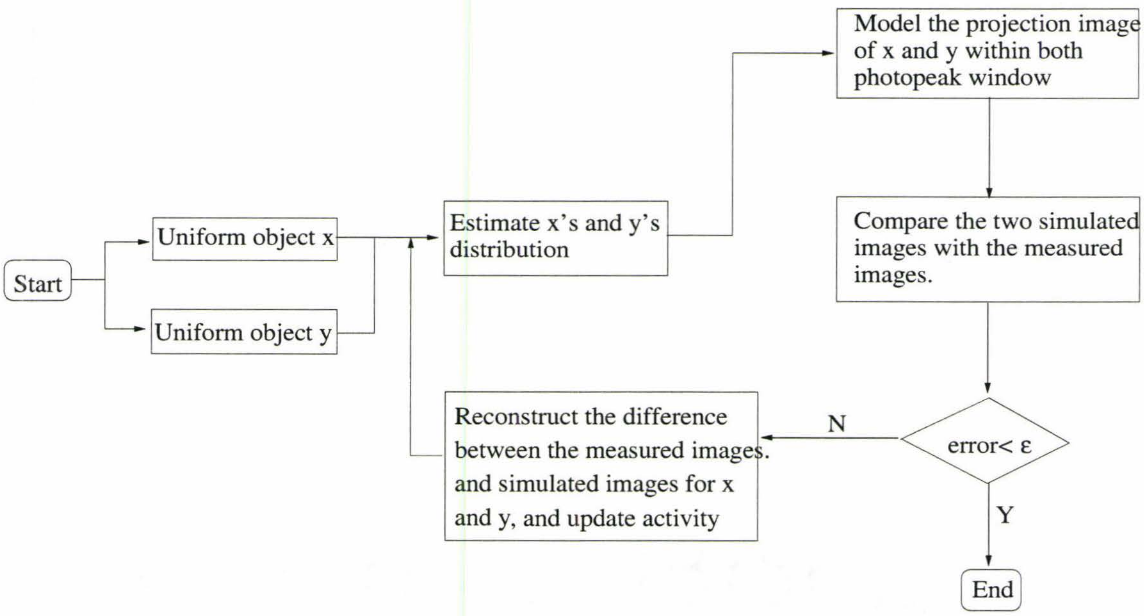

Figure 6.2: The flow chart of dual isotope reconstruction.

1) Start with two uniform objects denoting the reconstructed images of isotope x and isotope y. The initial activity of these two isotopes are both set as 1 MBq.

2) In each sub-iteration of OS-EM, MP-CFD is used to simulate the projection images of isotope x and y within the two photopeak energy windows. Attenuation,

scatter, and collimator response appropriate for each nuclide are all included. A total of four groups of projection images are obtained. They are related to: i) photons emitted from isotope x and detected in energy window x, ii) photons emitted from isotope y and detected in energy window x, iii) photons emitted from isotope x and detected in energy window y, and iv) photons emitted from isotope y and detected in energy window y. The simulated projection images obtained in window x and window y are summed together, respectively. The simulated projections are compared with the actual projection images, and the difference ratio of these two projections are back-projected respectively.

3) The total photon number of the two groups of simulated projection images are counted. The ratios of the simulated photon counts are compared with the actual photon counts.

4) The two objects are updated by multiplying with the two ratio back-projected images, and their activities are updated by multiplying with the photon count ratios.

5) The simulated projection images using MP-CFD is compared with the actual projections and the average error the each pixel value is taken. When the error is less than the constant threshold ϵ or the maximum iteration number is reached, the iteration is stopped, otherwise, go back to step 2).

6.3 Evaluation

6.3.1 Energy Spectrum, Simulation Method and Reconstruction

In the dual isotope reconstruction evaluation, two groups of radionuclides have been evaluated: i) $^{99m}Tc/^{201}Tl$ with the principle photopeak energies of 140 keV and 73 keV, and ii) $^{99m}Tc/^{123}I$ with the primary energies of 140 keV and 159 keV. The parameters of the simulation can be seen in Table 6.1.

Fig. 6.1 shows the spectra of these two groups of radionuclides when a 100 MBq point source is placed in the center of a water cylinder with a diameter of 38 cm and

Table 6.1: The simulation parameters used in the dual-isotope simulation. Energy is the primary energy of the isotope. Win_{up} and Win_{low} are the upper and lower energy limits in the simulation, respectively. $R_{c:p}$ represents the ratio of the number of crosstalk photons from one energy isotope to the other (e.g., $R_{Tc:Tl}$ represents the number of crosstalk photons from ^{99m}Tc in the ^{201}Tl energy window).

	Simulation 1		Simulation 2	
isotope	^{99m}Tc	^{201}Tl	^{99m}Tc	^{123}I
Energy (keV)	140	73	140	159
Win_{Lower}(keV)	126	68	126	151
Win_{Upper}(keV)	154	84	147	175
$R_{c:p}$	0:1	0.25:1	0.4:1	0.27:1

height of 56 cm when acquired with NaI(Tl) scintillators (~9-11% FWHM @ 140 keV energy resolution). The overlap of the spectra is not only from primary photons, but also from scattered photons. In Fig. 6.1(a), simultaneous imaging of $^{99m}Tc/^{201}Tl$ may result in the ^{99m}Tc photopeak data being contaminated by ^{201}Tl photons with energies of 135.3keV and 167.5keV [101]. However, this effect is very small due to the low emission rate of 135.3keV and 167.5keV photons from ^{201}Tl and relatively high amount of ^{99m}Tc compared to ^{201}Tl. On the contrary, ^{99m}Tc down-scatter photons, the fluorescence x-rays and scatters caused by photons interacting with the collimator greatly affect ^{201}Tl data acquired over the 68-84 keV ^{201}Tl acquisition window. Compared with Fig. 6.1(a), the proportion of cross-talk photons in the spectra for ^{99m}Tc and ^{123}I is high, as seen in Fig. 6.1(b). The primary energies of ^{99m}Tc and ^{123}I are very close, and hence, it is difficult to distinguish whether a photon event is emitted from ^{99m}Tc or from ^{123}I using NaI.

In the following simulation, the application of $^{99m}Tc/^{201}Tl$ is performed first followed by $^{99m}Tc/^{123}I$. Because of the different photon energies of ^{201}Tl and ^{99m}Tc, the attenuation maps for the two isotopes are different. The SPECT acquisition is performed using the MP-CFD code, simulating a LEHR collimator. The energy windows selected for ^{99m}Tc and ^{201}Tl are a) 126-154 keV and b) 68-84 keV. Very few ^{201}Tl photons are detected in window a), but the ratio of ^{99m}Tc photons to ^{201}Tl photon in window b) is about 0.25:1. For $^{99m}Tc/^{123}I$ simulation, the selected energy windows for ^{99m}Tc and ^{123}I are a) 126-147 keV and b)151-175 keV. The two energy windows are both asymmetric in order that the photopeak windows of ^{99m}Tc and ^{123}I do not overlap. From Fig. 6.1(b) the ratio of spilled-down ^{123}I photons to ^{99m}Tc in the ^{99m}Tc window is about 0.4:1, and the spilled-up ^{99m}Tc : ^{123}I in ^{123}I energy window is about 0.27:1.

In the following simulation, the object is set as $128 \times 128 \times 128$ voxels with the voxel size = 0.442 cm. The projection images were obtained over 360° at 15 seconds per projection using MP-CFD simulation. In image acquisition, four different projection sets are generated by the simulated photons: i) emitted from isotope 1 and also detected in the primary energy window of isotope 1; ii) emitted from isotope 2 but detected in the primary energy window of isotope 1; iii) emitted from isotope 1 but detected in the primary energy window of isotope 2; iv) emitted from isotope 2 and also detected in the primary energy window of isotope 2. Each projection set contains 120 projection images of size 128×128 pixels. Thus, a total of 480 projections are generated. The projection images of type ii) are summed with the appropriate projection of type i). The resultant images are used as the measured projections generated in the photopeak window of isotope 1, and the images of type iii) and iv) are added together to be the measured projections within the photopeak window of isotope 2.

Eq. 6.2 is used to reconstruct the objects corresponding to the 3D distribution of isotope x and y. 120 projections for each isotope are divided into 30 subsets, with 4 projections within each subset. 5 OS-EM iterations are used to reconstruct the resultant object. All the image degradation factors (GR, attenuation and scatter) are compensated except SP (because of the low energy of the emitted photons) by employing MP-CFD in the forward projection. To evaluate the result of photon cross-talk compensation, the conventional reconstruction method for single isotope imaging is performed on projection images of isotope x and y separately. Therefore, in the following discussion, the reconstruction result with crosstalk compensation is generated by dual-isotope reconstruction, and the result without crosstalk compensation is generated by single-isotope reconstruction. The estimated activities of these two reconstruction methods are recorded and compared to each other.

6.3.2 The Simulation of ^{99m}Tc and ^{201}Tl

Sphere Simulation

Simulation: The first simulation of ^{99m}Tc and ^{201}Tl uses three spheres in a cylinder filled with non-radioactive water, as seen in Fig. 6.3. The parameters of each individual region can be seen in the figure. In clinical practice, the activity of injected ^{99m}Tc would normally be higher than that of ^{201}Tl, therefore, in this simulation, a total of 300 MBq of ^{99m}Tc and 100 MBq of ^{201}Tl were simulated in the three spheres. The activity concentration ratios for ^{99m}Tc and ^{201}Tl of these three spheres were 10:1, 5:2 and 2:1, respectively. The amounts of ^{99m}Tc in these three spheres were 55.55, 116.29, and 128.17 MBq, with the ^{201}Tl amounts of 4.78, 40.05, and 55.17 MBq. 120 projections were generated by MP-CFD for each isotope and energy window, and the corresponding projections were summed together to be the measured dual isotope projections.

Result: Table 6.2 shows the reconstruction results for both single-isotope and dual-isotope reconstruction. The total activity estimation for dual isotope reconstruction is accurate, however, the result of single isotope reconstruction is overestimated. The activity ratio of ^{99m}Tc to ^{201}Tl is 3:1, and it can be seen in Table 6.1 that the amount of spill-down ^{99m}Tc photons is about 25% of the number of ^{201}Tl photons collected in ^{201}Tl energy window. In general, the total overestimated activity of ^{201}Tl is around 64%, which is close to $3 \times 25\%$ (activity ratio $\times$ the fraction of ^{99m}Tc spill-down photons in the ^{201}Tl photopeak energy window).

Examining the errors of the single-isotope reconstruction method, it can be seen that the crosstalk photons emitted from ^{99m}Tc to ^{201}Tl projection images cause an overestimation of ^{201}Tl radioactivity for both the total phantom and regionally.

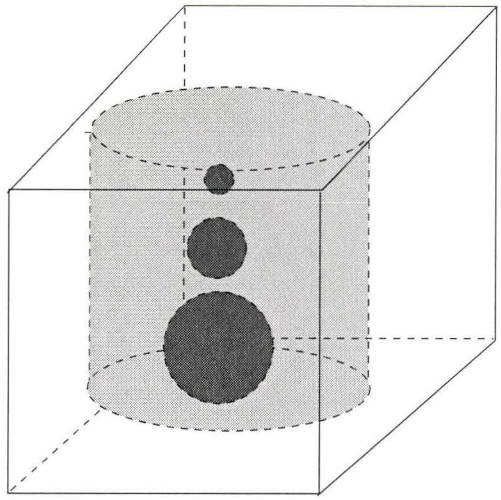

Figure 6.3: The simulated sphere object for $^{99m}Tc/^{201}Tl$ dual isotope imaging evaluation. The diameters of these three spheres are 6cm, 8cm, and 10cm respectively. The height and diameter of water cylinder are both 56cm.

The estimated activities for these three independent spheres are all higher than the actual value. The errors of estimated ^{201}Tl activity within sphere 2 and sphere 3 are close to 60%, but the error of sphere 1 is much higher (200%). This overestimation is due to the cross-talk photons from ^{99m}Tc. Without compensation, the crosstalk photons from ^{99m}Tc, but detected in ^{201}Tl energy window, are recorded as being emitted from ^{201}Tl, yielding an overestimation of the amount of ^{201}Tl. More detail of this will be discussed in the ^{99m}Tc and ^{123}I simulation. The error in ^{99m}Tc activity estimation is much less when using the single-isotope reconstruction method, further confirming that there is very little spill-over from ^{201}Tl to ^{99m}Tc energy window.

In contrast to single-isotope reconstruction, the simultaneous dual-isotope reconstruction presents more accurate estimation results. This improvement can be observed in activity estimations for both the total phantom and the three independent spheres. Dual-isotope crosstalk correction greatly improves the results of ^{201}Tl images, but only slightly changes the accuracy of ^{99m}Tc images, as a result of the minimal spill-over of ^{201}Tl to ^{99m}Tc.

Fig. 6.4 shows the central slices of both ^{99m}Tc and ^{201}Tl reconstructed images us-

Table 6.2: The radionuclide activity estimation with/without crosstalk compensation compared with the true activity value for sphere sources using ^{99m}Tc and ^{201}Tl.

Source	Region	True activity (MBq)	Single-isotope reconstruction (MBq)	Error(%)	Dual-isotope reconstruction (MBq)	Error(%)
^{99m}Tc	Sphere1	55.55	55.95	0.72	55.01	0.96
	Sphere2	116.29	115.42	0.75	114.75	1.32
	Sphere3	128.17	125.54	2.05	124.96	2.50
	Total	300.00	296.91	1.03	294.73	1.76
^{201}Tl	Sphere1	4.78	15.02	214.01	5.00	3.86
	Sphere2	40.05	63.49	58.53	40.20	0.38
	Sphere3	55.17	85.82	55.56	55.09	0.14
	Total	100.00	164.32	64.32	100.26	0.26

ing these two methods. The single-isotope reconstructed ^{99m}Tc images in Fig. 6.4(b) and dual-isotope reconstructed ^{99m}Tc image in Fig. 6.4(c) appear similar because of the negligible cross-talk fraction of ^{201}Tl photon into 140 keV window. They both show high similarity to the true image. The ^{201}Tl image using the single isotope reconstruction in Fig. 6.4(e) shows blurring around the three spheres. An improvement can be seen in the dual-isotope reconstructed images in Fig. 6.4(f), which looks very similar to the true image in Fig. 6.4(d).

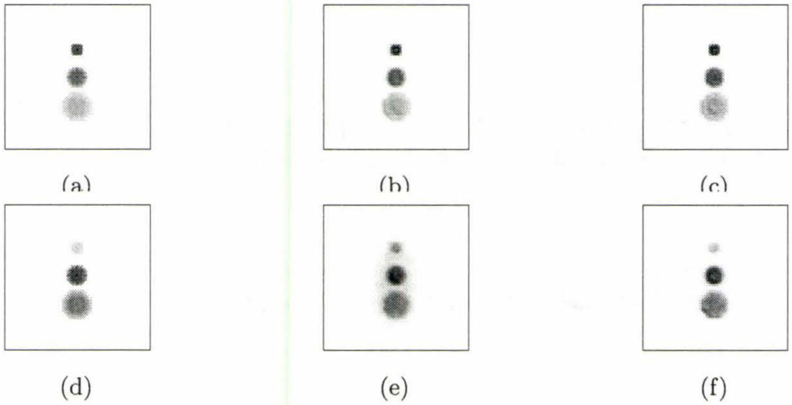

Figure 6.4: The central slices of the true object and reconstructed images. Top row: ^{99m}Tc images, and bottom row: ^{201}Tl images. The left images are the true object images. The middle column is for single-isotope reconstruction images and right column is for dual-isotope images.

Myocardial Defect Phantom Simulation

Simulation: The second simulation is based upon a myocardial defect phantom which is generated analytically. In the detection of coronary artery disease, dual-isotope myocardial SPECT with simultaneous acquisition of ^{201}Tl and ^{99m}Tc may be used to assess myocardial perfusion and metabolism. ^{201}Tl is used to depict myocardial perfusion defect, while ^{99m}Tc may be labeled with a glucose-like substance to depict glucose metabolism. A heart phantom with two blockage regions has been generated analytically, as shown in Fig. 6.5. The annulus in Fig. 6.5(a) represents a short axis view of the phantom, and Fig. 6.5(b) is a long axis view, which looks like a hollow cylinder with a half hollow sphere. The inner and outer diameters of the sphere are 6.5 cm and 13 cm, respectively, and the height of the cylinder is 11 cm. Two facing defects are simulated, with one of 45°, and the other one of 90°. The lengths of these two defect regions are both 5.5 cm. The phantom was then placed inside a 28-cm-high and 28-cm-diameter cylinder filled with non-radioactive water. The concentration ratios of 45° defect and 90° defect to healthy region for ^{99m}Tc were 0.5:1 and 0.25:1, and the ratios for ^{201}Tl are the same. Note the size of 90° defect was twice of the 45° defect, which indicates the total activity amount of the 90° defect is equal to that of 45° defect. Similar to the previous simulation, a total of 300 MBq ^{99m}Tc and 100 MBq ^{201}Tl was simulated in the phantom. The amount of ^{99m}Tc for healthy tissue, 90° defect, 45° defect were 282.13 MBq, 8.94 MBq, and 8.94 MBq, repectively, while the amounts of ^{201}Tl were of 94 MBq, 2.98 MBq, and 2.98 MBq, respectively. A LEHR collimator is used in the simulation. Again 120 projection images were modeled by MP-CFD including all the degradation factors with the exception of septal penetration. The simultaneous dual isotope measured projections are acquired by combining the photopeak projections and the corresponding cross-talk projections.

Reconstruction: The same as the previous sphere simulation, single-isotope and dual-isotope reconstruction are performed to compare the effect of cross-talk

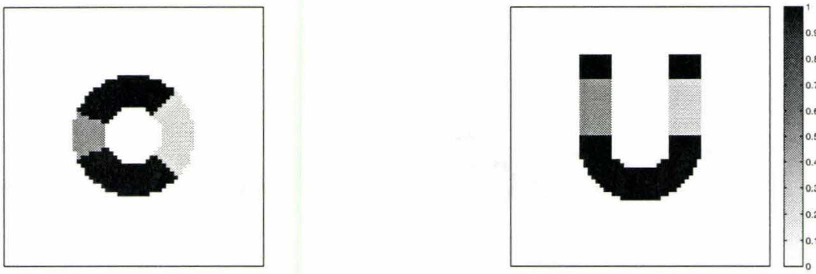

(a) (b)

Figure 6.5: The real cardiac defect configuration for both ^{99m}Tc and ^{201}Tl, as they have the same concentration. (a) shows the short axis view and (b) is the longitude view.

photons. The compensation of image degradation factors are all included.

Result: The results using dual isotope and single isotope reconstruction techniques are listed in Table 6.3. ^{99m}Tc images are still only slightly affected by ^{201}Tl spill-over photons, but the influence is significant in single isotope reconstructions of ^{201}Tl images. The activities estimated by the dual-isotope compensated reconstruction greatly reduces the errors, which are about 10%. Note the absolute errors are small. Therefore, it appears that simultaneous dual-isotope reconstruction is better able to accurately estimate the radioactivity compared to single-isotope reconstruction.

The representative short-axis and long-axis images of reconstructed ^{99m}Tc and ^{201}Tl uptakes are shown in Fig. 6.6 and Fig. 6.7. The healthy and infarcted areas of single-isotope or dual-isotope ^{99m}Tc imaging are highly similar to the true images. However, very obvious blurring is seen on the single-isotope reconstructed ^{201}Tl images, with the estimated activity at a level 100% higher than the true activity. Without cross-talk correction, the gray level of the 45° defect appears similar to the 90° defect, although the concentration of the 45° defect should be twice that of the 90° defect. The compensation of ^{99m}Tc spill-down photons effectively removes the blurring and differentiates the severity level of these two defects. However, it can

Table 6.3: The radionuclide activity estimation with/without crosstalk compensation compared with the true activity value using heart phantom models when ^{99m}Tc and ^{201}Tl are used for scanning.

Source	Region	True activity (MBq)	Single-isotope reconstruction (MBq)	Error(%)	Dual-isotope reconstruction (MBq)	Error(%)
^{99m}Tc	defect 45°	8.94	7.97	10.78	8.05	9.97
	defect 90°	8.94	8.00	10.54	8.21	8.16
	normal region	282.13	253.21	10.25	254.76	9.70
	phantom total	300.00	300.03	0.01	299.18	0.28
^{99m}Tl	defect 45°	2.98	6.93	132.63	3.00	0.69
	defect 90°	2.98	5.60	87.81	2.64	11.38
	normal region	94.05	138.99	47.80	89.20	5.15
	phantom total	100.00	205.68	105.68	101.43	1.43

be seen that there is still some artifact in the background using dual-isotope reconstruction. This may be because of insufficient number of iterations or inaccurate attenuation, scatter, collimator response compensation.

The previous analysis shows that simultaneous dual-isotope reconstruction of simultaneous ^{99m}Tc and ^{201}Tl imaging is able to separate ^{99m}Tc and ^{201}Tl images with excellent resolution when these two isotopes circulate within the same regions.

6.3.3 The Simulation of ^{99m}Tc and ^{123}I

The following simulations are based upon ^{99m}Tc and ^{123}I, but the region of uptake of these two isotopes are independent. That is, an active area contains either ^{99m}Tc or ^{123}I, but cannot have both. The measured projections are acquired in the same way of the simulation of ^{99m}Tc and ^{201}Tl. The reconstruction method is also the same except 10 rather than 5 iterations are performed on the projection images.

Sphere Simulation

Simulation: The first model of ^{99m}Tc and ^{123}I uses a three-sphere phantom

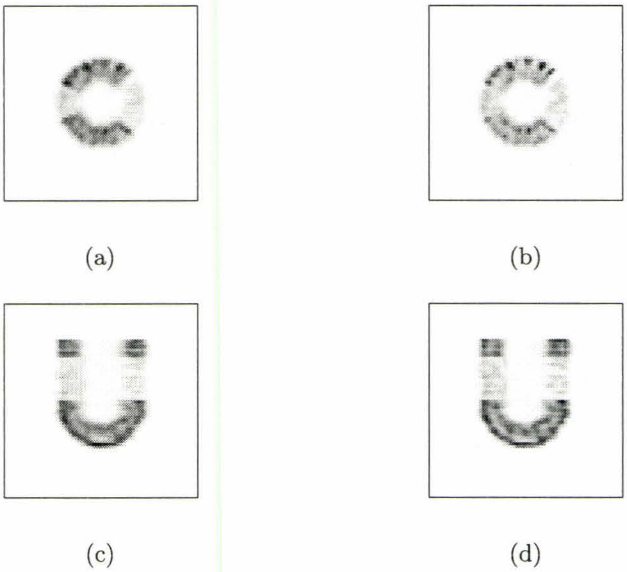

(a) (b) (c) (d)

Figure 6.6: The short and long axis views of ^{99m}Tc reconstructed images. Left column gives the result of single-isotope reconstruction result, and right column shows the dual-isotope reconstruction results. The result of single-isotope and dual-isotope reconstruction results show very high similarity. There are some dots in (b), which maybe because of limit number of iterations. Therefore, the iteration number for the following simulation is increased to 10.

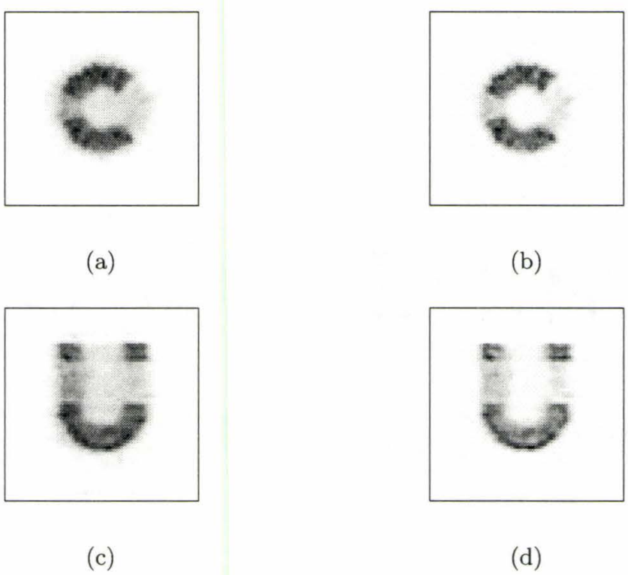

(a) (b) (c) (d)

Figure 6.7: The short and long axis views of ^{201}Tl reconstructed images. Left column gives the result of single-isotope reconstruction result, and right column shows the dual-isotope reconstruction results. The result of dual-isotope reconstruction shows less artifact than single-isotope reconstruction result.

similar but not the same as previous one. A 56 cm height and 56 cm diameter cylinder filled with nonradioactive water was used as the attenuation medium. The diameter of these three spheres were 6 cm, 8 cm, and 10 cm respectively. The centers of these three spheres are all located along the central slice of the cylinder, but they were placed apart from each other, as seen in Fig. 6.8. Therefore, there was no overlap between these three spheres. Sphere 1 and sphere 3 were filled with ^{99m}Tc, but sphere 2 was filled with ^{123}I. The total amount of ^{99m}Tc and ^{123}I were both 100 MBq. The amount of activity in each sphere was shown in Table 6.4. The projection acquisition method and reconstruction methods were the same as previous simulation.

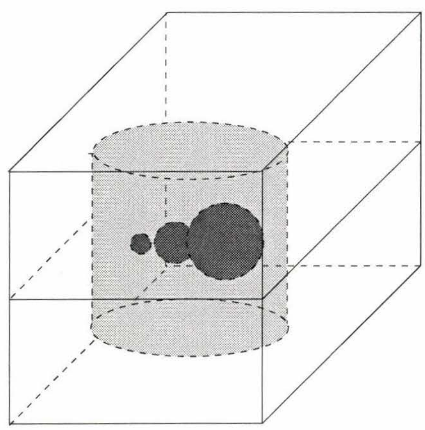

Figure 6.8: The simulated sphere object for $^{99m}Tc/^{123}I$ dual isotope imaging evaluation. The diameters of these three spheres are 6cm, 8cm, and 10cm respectively. The height and diameter of water cylinder are both 56cm.

Result: The estimated activity values of the three spheres are presented in Table 6.4 for both ^{99m}Tc and ^{123}I even though some of them do not contain radioisotope. The total overestimated activity is about 43% for ^{99m}Tc and 28% for ^{123}I , which is close to the fractions (40% and 27%) corresponding to the amount of cross-talk photons in the detected photopeak energy window.

It is apparent that the activity estimation for ^{99m}Tc-containing spheres 1 and 3, and ^{123}I in sphere 2 is accurate regardless of whether cross-talk compensation

Table 6.4: The radionuclide activity estimation for sphere source with/without crosstalk compensation compared with the true activity value using ^{99m}Tc and ^{123}I.

Source	Region	True activity (MBq)	Single-isotope reconstruction (MBq)	Error(%)	Dual-isotope reconstruction (MBq)	Error(%)
^{99m}Tc	Sphere1	24.23	25.03	3.33	24.97	3.08
	Sphere2	0	41.64	-	0	-
	Sphere3	75.77	76.73	1.26	76.03	0.34
	Total	100.00	143.65	43.65	101.32	1.32
^{123}I	Sphere1	0	7.36	-	0	-
	Sphere2	100.00	99.00	1.00	98.21	1.79
	Sphere3	0.00	22.25	-	0.00	-
	Total	100.00	128.86	28.86	98.53	1.47

is included or not. This indicates that the cross-talk photons in one region do not appear to significantly contaminate the estimation of other regions. However, the estimated activities of ^{99m}Tc in sphere 2 and ^{123}I in sphere 1 and 3 using single-isotope reconstruction are very high. The overestimated ^{99m}Tc activity for sphere 2 is about 41 MBq, which is close to 40% (the cross-talk fraction of ^{123}I in ^{99m}Tc photopeak window) of 100 MBq (the activity of ^{123}I within sphere 2), and the overestimated ^{123}I activities in sphere 1 and sphere 3 (7.36 MBq and 22.25 MBq) are also close to the corresponding ^{99m}Tc activity (24.23 MBq and 75.55 MBq) times the fraction of ^{99m}Tc cross-talk photons within ^{123}I photopeak window (27%). Combined with the accurate activity estimation of ^{99m}Tc in sphere 1 and sphere 3, ^{123}I activity in sphere 2 using single-isotope reconstruction, it can be seen that the spill-over photons only affect the activity estimation in the regions that contain their radionuclide source. The overestimated activity of a certain region depends on the fraction of cross-talk photons in this region. This is not very obvious in the ^{99m}Tc and ^{201}Tl simulation because the two radionuclides are distributed in the same regions. In the ^{99m}Tc and ^{201}Tl, it is not easy to see the relationship between the overestimated activity and the fraction of cross-talk photons. However, the same conclusion can be obtained with detail calculation.

It is apparent that the compensation of dual-isotope cross-talk photons yields more accurate results, as most of the activities are correctly estimated in the three spheres. Moreover, most of the activities are estimated in the three spheres, and little is contained within the background for both single-isotope and dual-isotope reconstruction result. This also indicates the accuracy of the attenuation, scatter and collimator response compensation.

Fig. 6.9 shows the anterior views of the reconstruction results compared with the true activity images. The second sphere can be seen in Fig. 6.9(b), which is the single-isotope method reconstructed ^{99m}Tc images. As expected, the overestimation in sphere 2 is readily removed using the dual-isotope method, as shown in Fig. 6.9(c), and very similar to the real image, as shown in Fig. 6.9(a). The same as ^{99m}Tc results, the single-isotope reconstruction resultant images of ^{123}I also contain overestimated activities within sphere 1 and sphere 3 in single-isotope reconstructed images, whereas dual-isotope crosstalk compensation is able to effectively correct the effect of cross-talk photons.

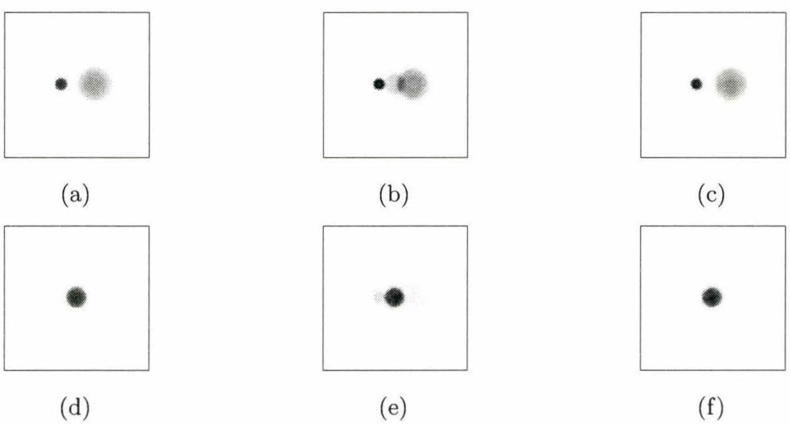

Figure 6.9: The anterior views of the true sphere phantom using ^{99m}Tc and ^{123}I. First row shows the images of ^{99m}Tc, and second row shows the images of ^{123}I. The left column are the true activity images, middle are the single-isotope reconstruction images, and right are the dual-isotope reconstruction images.

Digital Mouse Phantom Simulation

Simulation: The second simulation uses the Digital Mouse Whole Body Phantom (MOBY). Fig. 6.10 shows the region used in the MOBY simulation. 10 MBq of ^{123}I was simulated in the thyroid. In order to localize thyroid, 100 MBq ^{99m}Tc was simulated in the surrounding skeleton. LEHR collimator was used in this simulation. Again, the acquisition and reconstruction methods were the same as the previous study.

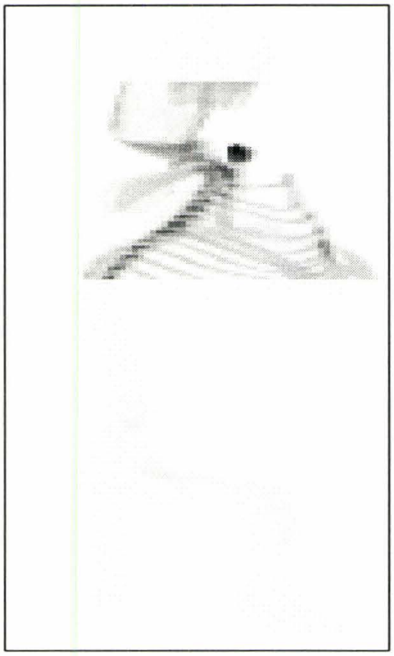

Figure 6.10: Region of interest (ROI) in MOBY phantom simulation. ROI is denoted in the darker region.

Result: The estimated results are shown in Table 6.5. For the estimation of ^{99m}Tc activities in the bone and thyroid, the single-isotope reconstruction estimated ^{99m}Tc activity in the whole mouse body is about 15% higher than the real value, with 4.7 MBq activity overestimated in the thyroid. This value is close to 40% of the amount of ^{123}I (10 MBq), which further confirms that the amount of overestimated activity depends on the fraction of cross-talk photons. The error in ^{99m}Tc quantitation in the bone is about 7%, which is close to the result for dual-isotope reconstruction. This indicates that the error of activity estimation for nonuniform object is due to attenuation and scatter compensation. The estimated result for ^{99m}Tc in the thyroid using the dual-isotope reconstruction method is 0, which agrees with the actual result. The total error of dual-isotope reconstruction is only 2%. Together with the error in the bone, it can be seen that there is some activity estimated in the background.

The estimation of ^{123}I activity is similar to ^{99m}Tc. The overestimated activity of ^{123}I using the single-isotope reconstruction method in the bone is 25 MBq, which is about 27% of the simulated 100 MBq ^{99m}Tc . The single-isotope reconstructed ^{123}I activity in the thyroid is also overestimated, as the error is over 30% of the true value. Although the overestimated activity due to cross-talk photons usually appears in the regions containing the source, the thyroid is still contaminated because it is close to the bone. The same as ^{99m}Tc activity estimation, the estimation using dual-isotope reconstruction is more accurate, and the overestimated activity in the background is much less because of the small volume and low amount of activity in the thyroid.

Table 6.5: The radionuclide activity estimation for MOBY phantom with/without crosstalk compensation compared with the true activity value using ^{99m}Tc and ^{123}I.

Source	Region	True activity (MBq)	Single-isotope reconstruction (MBq)	Error(%)	Dual-isotope reconstruction (MBq)	Error(%)
^{99m}Tc	Bone	100.00	92.09	7.91	93.56	6.44
	Thyroid	0	4.68	-	0.00	-
	Total	100.00	115.13	15.13	102.70	2.70
^{123}I	Bone	0	25.74	-	0	-
	Thyroid	10.00	13.27	32.67	9.62	3.76
	Total	10.00	41.53	315.31	9.97	0.32

Fig. 6.11 shows the results with single isotope and dual isotope reconstruction. In the presence of cross-talk photons (single isotope reconstruction), Fig. 6.11(a) and Fig. 6.11(c) exhibit the shapes of both skeleton and thyroid. It is not easy

to differentiate thyroid and skeleton. However, with dual-isotope compensation, Fig. 6.11(b) and Fig. 6.11(d) show better results than Fig. 6.11(a) and Fig. 6.11(c).

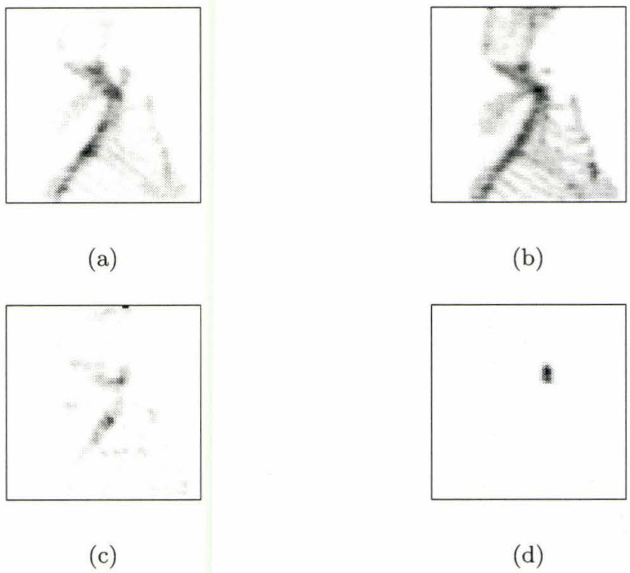

Figure 6.11: The anterior views of the reconstructed ^{99m}Tc (first row) and ^{123}I (second row) images. Left collum are single-isotope reconstruction results, and right are dual-isotope reconstruction results.

Myocardial Phantom Simulation

Simulation: The final simulation again uses the heart phantom, as applied in ^{99m}Tc and ^{201}Tl evaluation previously. Different than the previous modeling, only the 90° defect was simulated. The healthy region was filled with 100 MBq of ^{99m}Tc labeled with Sestamibi to study the myocardial perfusion, as the defect region with 100 MBq of ^{123}I labeled with fatty acids to study fatty acid metabolism. The extent of ^{123}I defect was greater than that of ^{99m}Tc defects. Therefore, ^{99m}Tc images were acquired to depict perfusion (ie. blood flow). ^{123}I images were used to present the metabolism of fatty acid. In the event of a perfusion defect (ie, poor blood flow), it is important to determine the viability of the heart. A viable myocardium implies that the heart is still metabolizing fatty acids even though perfusion is impaired. Such tissue can be reperfused with surgery, while non-viable myocardium (ie, not metabolically active) cannot be repaired. The acquisition and reconstruction methods were still the same as the above simulation.

Result: Table 6.6 has listed the reconstruction results using the two reconstruction methods. Similar to the previous simulation, the overestimated activity using single-isotope reconstruction is related to the fraction of the cross-talk photons in the corresponding energy window, and dual-isotope reconstruction has the ability to accurately estimate the activity distribution.

Table 6.6: The radionuclide activity estimation for heart phantom with/without crosstalk compensation compared with the true activity value using ^{99m}Tc and ^{123}I.

Source	Region	True activity (MBq)	Single-isotope compensation (MBq)	Error(%)	Dual-isotope compensation (MBq)	Error(%)
^{99m}Tc	Normal Tissue	100.00	96.16	3.84	100.12	0.12
	Defect	0	38.63	-	0.00	-
	Total	100.00	139.25	39.25	100.12	0.12
^{123}I	Normal Tissue	0	25.45	-	1.52	-
	Defect	100.00	93.83	6.17	95.20	4.80
	Total	100.00	122.78	22.78	99.99	0.01

Fig. 6.12 and Fig. 6.13 demonstrate the short-axis and long-axis view of the heart phantom simulation. The incorrectly estimated activity in the defect region of ^{99m}Tc images may be interpreted as healthy or low level blockage, and the incorrectly estimated activity in the healthy region of ^{123}I images may be interpreted as infarction over all the heart.

6.4 Conclusion

Cross-talk photons might result in very severe problems such as overestimated activity and wrong determination of the infarcted region. The conventional single-isotope reconstruction method is unable to correct the cross-talk contamination,

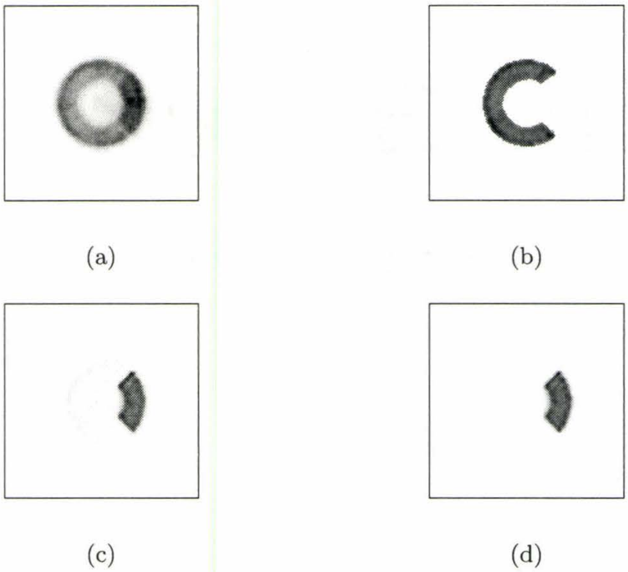

Figure 6.12: The short axis views of ^{99m}Tc (first row) and ^{123}i (second row) images. The images without cross-talk compensation (left column) demonstrate very obvious overestimated activity in wrong regions. Dual-isotope compensation results (right column) show similar profiles to the true images.

thereby resulting in an overestimated activity with the amount close to the product of the cross-talk photon fraction and the true activity of the other isotope. In this chapter, we have introduced the dual isotope compensation method using OS-EM reconstruction. Simultaneous imaging with ^{99m}Tc and ^{201}Tl, and ^{99m}Tc and ^{123}I are simulated for different cases of dual isotope imaging. It has been shown that dual isotope compensation results in very accurate results, and the overestimated activity using single-isotope reconstruction depends on the fraction of crosstalk photons.

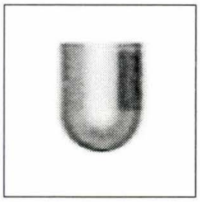

(a)

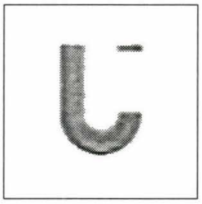

(b)

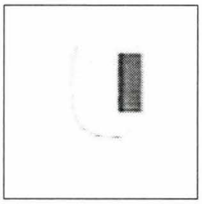

(c)

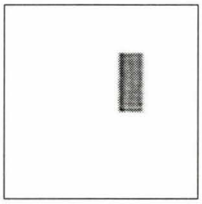

(d)

Figure 6.13: The long axis views of ^{99m}Tc (first row) and ^{123}i (second row) images. Left column are single-isotope reconstructed images, and right column are dual-isotope reconstructed images.

Chapter 7

Conclusion and Future Work

This chapter briefly reviews the previous work and discusses possible future work using accelerated Monte Carlo based quantitative reconstruction.

7.1 General Comments

In this work, the accelerated Monte Carlo code has been incorporated into a maximum likelihood expectation maximization (ML-EM) iterative reconstruction to accurately recover the radionuclide activity distribution within the patient. In order to increase the speed of reconstruction, ordered-subset expectation maximization (OS-EM) method is used instead of ML-EM reconstruction.

The primary advantage of Monte Carlo is that it is very accurate in simulating the photon transport at the expense of exceedingly long computation time. Three variance reduction techniques have been developed to accelerate Monte Carlo simulation. Convolution-based forced detection (CFD) forces the photons to travel along the axis perpendicular to the detector by convolving the photon history weight with spatial resolution models. Multiple projection sampling (MP-CFD) technique is based upon CFD method, but projects the photons to multiple detectors simultaneously instead of one single detector. The septal penetration models are also included in CFD using ray tracing generated models. The accuracy and speed of these methods have been evaluated. Accelerated MC simulation is applied in the reconstruction to accurately compensate for image degradation factors such as photon attenuation, scatter and collimator response. The other advantage of MC is it is able to estimate the activity related to the actual projection images.

In the reconstruction simulation, the total amount of radioactivity is estimated in each sub-iteration of OS-EM reconstruction based upon MC simulation. Several phantoms have been utilized to evaluate the compensation effect of different degradation factors.

In order to study two biophysical characteristics for certain organs, dual-isotope imaging has been introduced. Simultaneous dual-isotope imaging can avoid misregistration due to patient movement. However, simultaneous imaging results in crosstalk photons from one isotope to the other. The conventional reconstruction method is not able to remove the effect of cross-talk photons. One dual-isotope reconstruction method has developed and the accuracy has been evaluated.

7.2 Future Work

The future work can be divided into four categories: i) the evaluation of current work, ii)faster Monte Carlo simulation, iii) more accurate photon modeling, iv) SPECT image reconstruction.

7.2.1 The Evaluation of Current Work

In our previous work, most of the evaluation work is based upon simple experimental data or digital phantom simulation. In the experiments, only uniform attenuation maps were utilized. In the future work, some experiments using non-uniform attenuation maps should be performed to evaluate the accuracy of both variance reduction techniques and reconstruction.

7.2.2 Monte Carlo Acceleration

The current reconstruction code still takes a few hours to complete 5 OS-EM iterations. This is still too slow for clinical use. Therefore, more variance reduction techniques are expected to be developed. One example is multiple photons to be simulated simultaneously instead of one single photon for each photon simulation. This can be achieved by parallel processing or through advanced hardware implementations such as graphic processors. De Vries, et. al, has implemented Monte Carlo simulation with an array processor [102]. The future work can be performing our variance reduction techniques on the multiple processor based upon their method.

7.2.3 Photon Event Modeling

The reconstruction results for the current method is relatively accurate, however, some photon interactions such as Rayleigh scattering or photon scatter in the collimator is neglected. It has been mentioned in Chapter 2 that when photon energy is higher than 200 keV, the neglect will result in about a 7% error. Therefore, more accurate modeling is required for Rayleigh scattering. There are several other references referred to collimator penetration and scattering [103–106], collimator response including collimator scatter should be modeled.

7.2.4 SPECT Image Reconstruction

In radiotherapy applications in Nuclear Medicine, it is very important to calculate the absorbed doses to the organs in the body. These can be determined from the cumulative radioactivity in each organ. The cummulative activity A_c, is calculated by integrating the activity over time for any particular source organ:

$$A_c = \int A(t)dt \tag{7.1}$$

where, $A(t)$ is the function of activity.

The absorbed dose to a target organ, D_t, is calculated from:

$$D_t = \sum_s A_c(s)S(t,s)dt \tag{7.2}$$

where D_t is the absorbed dose of the target organ, $A_c(s)$ is the activity of the source organ, $S(t,s)$ is the mean absorbed dose factor of the source organ to target organ.

In the current study, the radioactivity distribution is assumed to remain constant during the scanning. That is, the biological washout time of the radiopharmaceutical is much longer than its physical half life $T_{\frac{1}{2}}$. In the simplest case, the time activity curve (TAC) of the radionuclide can be written as an exponential decrease over time:

$$A(t) = A_0 e^{-\lambda t} \tag{7.3}$$

where λ is the biological washout constant (min^{-1}). Fig. 7.1(a) shows the time activity curve including only radionuclide physical decay. It is assumed that the biological half-life $T_{\frac{1}{2}}$ of the radiopharmaceutical is much longer than the physical half-life of the radionuclide. Therefore, the scan time for the object corresponding to each circle can be neglected because of the long biological decay time. The quantitative activity estimated in the static reconstruction is related to the circles on the curves. It is easy to derive the value of A_0 and λ using the quantitative activity, $A(t)$, for a particular time.

However, the physiological characteristics of organs such as perfusion, metabolism, or washout cause a change in radionuclide distribution. In reality, the biological half-life $T_{\frac{1}{2}}$ of the radiopharmaceutical may match the physical half-life of the radionuclide, which makes the combined activity curve look like Fig. 7.1(b). The activity curve is not an exponential curve any longer. Moreover, it takes a period of time to uptake the radiopharmaceutical due to the functions of different organs, as the activity curve shown in the solid line in Fig. 7.1(c). However, when the dynamic in-

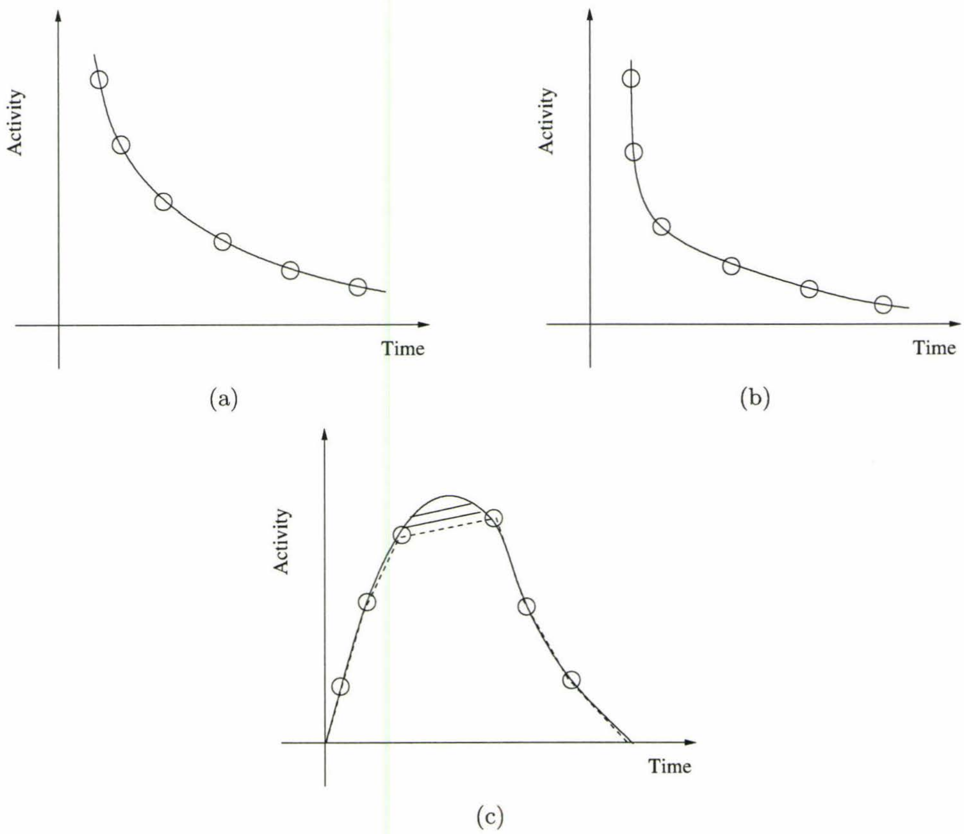

Figure 7.1: Three types of time activity curves: physical radioactivity decay (a), physical + biological decay for the activity of the radiopharmaceutical (b), the activity curve in (c) shows the activity of radiopharmaceutical under physical and biological decay after organ uptake. The circles denote the activities detected at the corresponding scan times. Solid curve denotes the real activity curve and dash line is the estimated activity curve.

formation of the radiopharmaceutical is lacking, static reconstruction technique may result in the inconsistent activities (circles) based upon the scan time. These values may underestimate initial high dose. Therefore, dynamic imaging is important as it fills in missing information during rapid changes in radiotracer distribution.

Dynamic studies of varying radioactivity are required to evaluate the effect of different radionuclides. The objective of dynamic SPECT imaging is to investigate the dynamic behavior of organs and determine the changes in biodistribution in order to calculate cumulative organ doses. Dynamic imaging can be applied in a wide variety of clinical circumstances, such as using ^{99m}Tc-labeled teboroxime to measure the perfusion in myocardial tissue, ^{123}I-labeled iodophenylpentadecanoic acid ($^{123}IPPA$) to measure the fatty acid metabolism [107], and ^{131}I-labeled hippuran in dynamic renal function study [108] [109].

Future work will focus on determining the total cumulative organ dose using the accurate quantitative reconstruction method proposed in this work. This approach will be applied to multi-isotope radionuclide therapy.

Appendices

Appendix A

Geometric Response Compensation and Gibbs Ring Artifact

A.1 Introduction

Geometric response (GR) is the primary factor influencing detector spatial resolution. It is impossible to perform MC simulations without a collimator, therefore, geometric response is always included once MC is performed. In this thesis, analytical projection is used in geometric response compensation.

As a spatially variant function denoted in Eq. 4.5 and Eq. 4.6, geometric response is proportional to the collimator hole size, source-detector distance, and inversely proportional to collimator length. The amount of response (as measured by FWHM) is shown in Eq. 4.6.

Among the three types of collimators (low energy, medium energy and high energy collimators), high energy collimators have largest geometric response for the same source-detector distance because of its largest collimator hole size. In order to evaluate the effect of geometric response compensation, a simulation was performed using ^{131}I and HEGP collimator. Detector intrinsic resolution has been added to all the simulations by default, and is invariant for a given photon energy for each system.

A.2 Compensation Method

In the geometric response compensation, analytical forward projection and back-projection as shown in Fig. 5.1 are utilized. In the forward projection, several rays are emitted from one voxel to the projection images with the cross-section of these rays for a certain source-detector distance related to the corresponding spatial resolution. The value of the voxel is convolved with the model of spatial resolution and recorded on the projection images. In the back-projection, the rays are also traced from the projection bins to the reconstructed object. The value on each projection bin is convolved with different models of spatial resolution for differing detector-object distanced and recorded on the object.

In the OS-EM reconstruction, forward and back-projections are repeated until the end of the iteration. The values on the projection images are based upon the voxel value in the object but not the activity of the object. Therefore, it is impossible to estimate the activity of the object using this analytical method and only the relative activity distribution can be observed.

A.3 Evaluation

Simulation: A 21 cm diameter and 38 cm high uniform cylinder filled with ^{131}I is used in the evaluation when HEGP is employed. The cylinder phantom is set as a $128 \times 128 \times 128$ matrix size with the voxel size $= 0.442$ cm. The voxel value of the cylinder is set as 1. No attenuation map is used in order to minimize the influence of attenuation and scatter. 120-128 $\times$ 128 projections are simulated by analytical forward projection as the projection lines following the pattern of spatial resolution functions in Eq. 4.5 for different source-detector distances.

Reconstruction: OS-EM reconstruction is used to recover the activity distribution. The 120 projections are divided into 30 subsets with 4 angles/subset. Two reconstructions, with and without GR compensation, are performed. In the GR compensation reconstruction, the correction is performed as in Fig. 5.1 using several divergence/convergence rays in both forward and back projection steps. A number of lines are emitted from a point either in forward projection or back-projection. The cross-sections of these lines are 2D Gaussian models representing the source-detector resolution. In the no compensation reconstruction, the projection lines in Fig. 5.1 are parallel to each other and are perpendicular to the collimator.

Result: Fig. A.1 depicts central slices of the reconstructed images together with the central line profiles of these slices. As shown in Fig. A.1(b) and Fig. A.1(c), the resultant images of these two methods look similar except for the obvious ringing artifact in the GR compensated result. The estimated average voxel values are both close to the true value. It can be seen in Fig. A.1(d) that the edge of the compensated result is more obvious than the uncompensated result, but ripples in the compensated result are also more significant. This ripple is called Gibbs ring artifact, which is caused by spatial resolution compensation when the sharpness of an edge is recovered.

This Gibbs ring artifact is due to geometric response compensation. As mentioned in Chapter 3, the geometric response can be written by a 2D Gaussian function. Therefore, when a collimator is used, the photon weight is convolved with a Gaussian function (Fig. A.2(a)), which is related to the truncated low spatial frequency region (grey area) in Fig. A.2(b). That is, the sampling only takes the effective data information in the low spatial frequency portion of the image and the high frequency information is not sampled during the projection. This missed information results in truncation in spatial frequency-space and Gibbs ring artifact in spatial domain. This is similar to truncation artifact in MRI images. In order

(a)

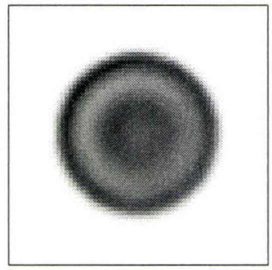

(b)

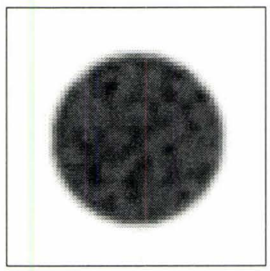

(c)

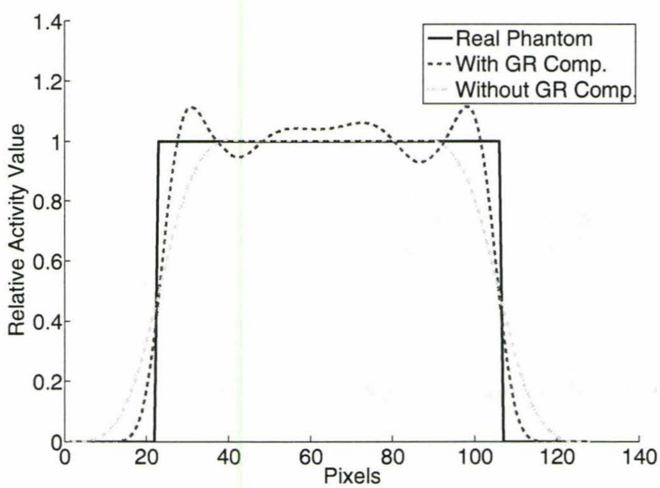

(d)

Figure A.1: The real phantom (a) compares with the geometric response compensation result (b) and the uncompensated result (c). The images shown here are corresponding to the center slices of the reconstructed objects. (d) gives the plots of the center line in (a), (b) and (c). The geometric response compensation causes Gibbs ring artifact.

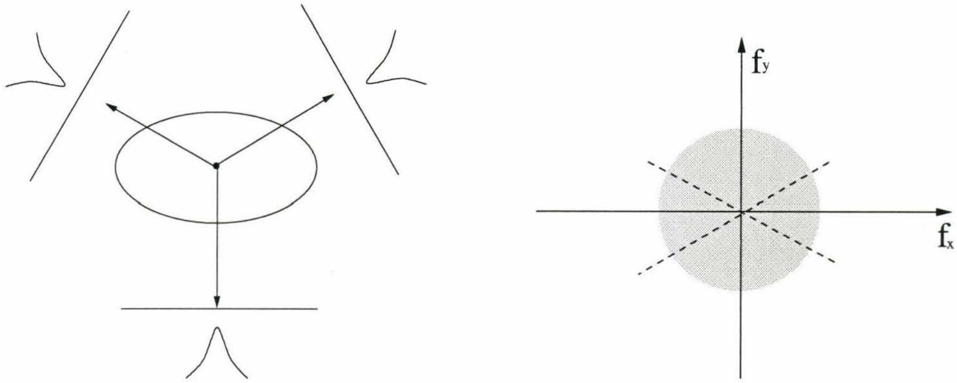

(a) (b)

Figure A.2: The spatial sampling of the detectors around the object (a). The frequency description of this sample due to 2D Fourier Theorem.

to reduce Gibbs ring artifact, the object information on all the frequency domain should be sampled, which means the Gaussian function in the spatial domain should be narrow, ie., δ function. It requires the collimator hole to be very small, but this is impossible in reality.

A.4 Factors Affecting Gibbs Ring Artifact

Gibbs ring artifact is a severe problem in SPECT image reconstruction. Which factors will affect Gibbs ring artifact in geometric response compensation? Different sampling frequencies and collimators have been used to investigate the factors that influence Gibbs ring artifact. Two 2D circle in the sizes of 64×64 and a 512×512 with pixel sizes of 0.884 cm and 0.1105 cm are studied using either HEGP collimator/^{131}I or LEHR collimator/^{99m}Tc . The diameter of the circle is 38 cm. The same as previous simulations, the phantom was placed in air. 120 projections are taken by the analytical forward projector over 360°. OS-EM is utilized to reconstruct the images with GR compensation. 30 subsets are taken with 4 angles/subset. A total of 5 iterations are performed.

Fig. A.3 shows the central lines of reconstructed results for four cases: a) 0.884 cm/pixel and HEGP collimator, b) 0.884 cm/pixel and LEHR collimator, c) 0.1105 cm/pixel and HEGP collimator, d) 0.1105 cm/pixel and LEHR collimator. The acquisition method and reconstruction method are the same as the previous study.

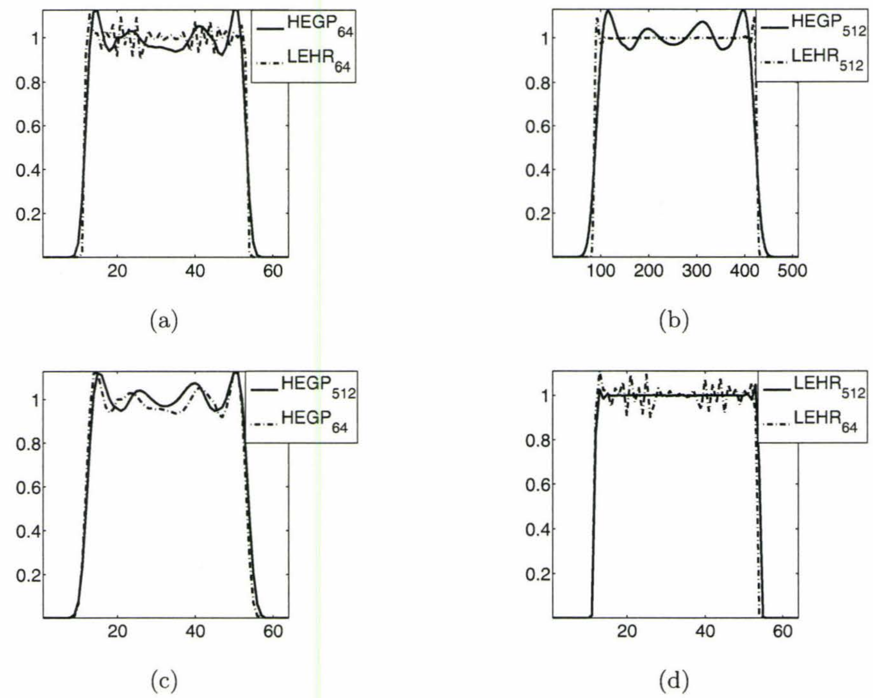

Figure A.3: Gibbs ring artifact on the geometric response compensation results. The subscripts in the legend denotes the matrix size of the object. (a) shows the center line profiles of 64 $\times$ 64 object using HEGP and LEHR collimators, and (b) shows the results of 512 $\times$ 512 objects using the two collimators. (c) compares the artifact of the different pixel size when LEHR collimator is used. The center profiles of 64×64 and 512×512 reconstructed image are plotted. (d) also evaluate the effect of different pixel size but using HEGP collimator.

Fig. A.3(a) and Fig. A.3(b) compares the compensation results using different collimators for the same pixel size. It can be seen that the Gibbs ring artifact is more apparent using a HEGP collimator than LEHR collimator for the same pixel size, confirming our presumption regarding spatial frequency sampling.

Fig. A.3(c) and Fig. A.3(d) compares the compensation results of different pixel sizes using the same collimator. The central profile of the reconstructed images in an array of 512×512 is sampled every 8 pixels to match the line profile of 64×64 object. Reconstructed results for different pixel sizes using HEGP collimator are similar, as ring artifacts being very apparent, however, the reconstructed results using LEHR collimator in Fig. A.3(c) are affected by pixel size. When the pixel size is small, its artifact is insignificant. On the contrary, the artifact is very obvious when pixel size is large. This is because of Nyquist theorem, the sampling frequency should be at least twice of the object's maximum frequency. When LEHR collimator is utilized, the geometric response is small, and the corresponding frequency is high. This high frequency requires high sampling frequency (twice of the geometric frequency). Therefore, when the object's sampling frequency is low (0.884cm/pixel), an artifact can be seen in the reconstructed image. In the two plots of Fig. A.3(c) and Fig. A.3(d), the artifacts are all significant except that the simulation of 512×512 object using LEHR collimator with pixel size of 0.1105cm shows little Gibbs ring artifact. The artifact at the edge of 512×512 reconstructed object using LEHR collimator simulation is about the size of 1 voxel.

Therefore, it can be said that:

1) High sampling frequency of the object is required, especially when high resolution collimator is used.

2) Gibbs ring artifact is not influenced by the sampling frequency, but is affected by the resolution of collimator.

Appendix B

Matlab Codes In This Thesis

B.1 Collimator Generation

```
function [collim_odd, collim_even]= collim(pixels,pixelsize,
    sidelength,septhick)
% [collim_odd, collim_even] = collim(pixels,pixelsize,
    sidelength,septhick);
%[collim_odd, collim_even] = collim(256,0.1,0.8,0.8);
% This code is to generate a hexagonal collimator with size
    of pixels. The pixel size
% is equal to pixelsize, sidelength is the length of the
    hexagon side. septhick is
% the thickness of septa

if(nargin <4)
    error('Please input enough parameter');
end

if(mod(pixels,2) == 0)
    mtxsize = pixels+1;
else
    mtxsize = pixels;
end

collim_odd = zeros(mtxsize,mtxsize);
collim_even = zeros(mtxsize-1,mtxsize-1);

matrix_length = mtxsize * pixelsize;
halflength = matrix_length/2;

% The height and length of a hexagon
step_x = sidelength * 3 + septhick/sqrt(3)*4;
```

```
step_y = step_x*sqrt(3)/3;

halfstep_x = step_x/2;
halfstep_y = step_y/2;

% find the center of each hexagon
x_start = 0 ;
y_start = 0 ;

bool = 1;
count = 1;
x_1(count) = x_start;
x_curr = x_start;
x_2(count) = x_1(count) + halfstep_x;
x_2(count+1) = x_1(count) - halfstep_x;


% start with the center of the collimator, define the
    location of all the hexagon
% when a pixel is within a hexagon, the value is set as 1,
    otherwise, it is 0.
while(bool)
    count = count + 1;
     x_curr = x_curr + step_x;
     x_1(count) = x_curr;
     x_2(count+1) = x_1(count) + halfstep_x;

     count = count+1;
     x_1(count) = -x_curr;
     x_2(count+1) = x_1(count) - halfstep_x;
     if(x_curr<halflength-step_x*2 )
         bool = 1;
     else
         bool = 0;
     end
end
num_x = count;

bool = 1;
count = 1;
y_1(count) = y_start;
y_curr = y_start;
y_2(count) = y_1(count) + halfstep_y;
y_2(count+1) = y_1(count) - halfstep_y;
```

```
while(bool)
    count = count + 1;
     y_curr = y_curr + step_y;
     y_1(count) = y_curr;
     y_2(count +1) = y_1(count) + halfstep_y;

     count = count+1;
     y_1(count) = -y_curr;
     y_2(count +1) =y_1(count) - halfstep_y;
     if( y_curr<halflength-step_y*2 )
         bool = 1;
     else
         bool = 0;
     end
end
num_y = count;


hexlength = floor(sidelength/pixelsize*2.5);
if(hexlength>pixels)
    hexlength = pixels;
end
if(mod(hexlength,2) == 0)
    hexlength = hexlength +1;
end
halfhexleng = (hexlength-1)/2;
hex = hexagon(hexlength, pixelsize, sidelength);
data_1 = zeros(mtxsize, mtxsize);
data_2 = zeros(mtxsize, mtxsize);
cenX = (mtxsize+1)/2;
cenY = (mtxsize+1)/2;

for i = 1:num_x
    for j = 1:num_y
        x = floor(x_1(i)/pixelsize)+cenX;
        y = floor(y_1(j)/pixelsize)+cenY;
        if(-halfhexleng+y > 0 & halfhexleng+y<mtxsize & -
           halfhexleng+x > 0 & halfhexleng+x<mtxsize)
            data_1(-halfhexleng+y:halfhexleng+y, -
               halfhexleng+x:halfhexleng+x) = data_1(-
               halfhexleng+y:halfhexleng+y, -halfhexleng+x:
               halfhexleng+x)+hex;
        end

        x = floor(x_2(i)/pixelsize)+cenX;
```

```
        y = floor(y_2(j)/pixelsize)+cenY;
        if(-halfhexleng+y > 0 & halfhexleng+y<mtxsize & -
            halfhexleng+x > 0 & halfhexleng+x<mtxsize)
            data_2(-halfhexleng+y:halfhexleng+y, -
                halfhexleng+x:halfhexleng+x) = data_2(-
                halfhexleng+y:halfhexleng+y, -halfhexleng+x:
                halfhexleng+x)+hex;
        end
    end
end

collim_odd = data_1+data_2;
%colormap(flipud(gray(256)))
colormap(gray(256))
imagesc(collim_odd);axis square;
```

B.2 Septal Thickness Calculation

```
function data = raysept(sour_cen,angle_info,colli_info,
   store_info,filename)
%data =
%raysept([sour_x,sour_y],[angle,angleN],[colli_side_leng,
   colli_sep_thick],[store_radius,store_radius_N,
   bool_filename,bool_newfile],filename)
% data = raysept
   ([0.1,0.1],[30,1000],[0.167,0.02],[0.442*128/sqrt(2)
   ,1000,1,1],'temp.dat');

%This code is to genetrate a pathlength lookup table

angle = angle_info(1);
angle_N = angle_info(2);
colli_side_leng = colli_info(1);
colli_sep_thick = colli_info(2);
store_radius = store_info(1);
store_radius_N = store_info(2);
bool_filename = store_info(3);
bool_newfile = store_info(4);

if(~bool_filename)
    filename = sprintf('ray_angle%d_angleN%d_radius%
       d_radiusN%d',angle,angle_N,floor(store_radius),
       store_radius_N);
end

if(bool_newfile)
    fid = fopen(filename,'w');
    fclose(fid);
end


angle_step = angle/angle_N;
store_step = store_radius/store_radius_N;

% to define the height and length of a hexagon
step_y = colli_side_leng * sqrt(3) + colli_sep_thick;
step_x = step_y*sqrt(3);

height = colli_side_leng * sqrt(3)/2;
```

```
halfstep_x = step_x/2;
halfstep_y = step_y/2;

tracing_step = store_step;
tracing_N = store_radius_N;

% cen_N is the number of the hexagons around the center
    hexagon
cen_N = 19;
for i = 1:1:angle_N
    angle_cur = (i-1)*angle_step/180*pi;
    cen_x = 0;
    cen_y = 0;
    count_index = 0;
    for m = -2:2
        for n = -4:4
            sum_index = abs(m) + abs(n);
            if(sum_index == 2 | sum_index == 4 | sum_index
                == 0 )
                 count_index = count_index+1;
                 cen_x_curr(count_index) = cen_x + m*
                    halfstep_x;
                 cen_y_curr(count_index) = cen_y + n*
                    halfstep_y;
            end
        end
    end

    xaxis = sour_cen(1) - cen_x;
    yaxis = sour_cen(2) - cen_y;

    % to determine whether a pixel is inside or outside the
        first hexagon
    bool_in = (yaxis>-height) & (yaxis<height) & ((yaxis -
       sqrt(3)*xaxis -height*2)<0) & ((yaxis -sqrt(3)*xaxis
       +height*2)>0) ...
            & ((yaxis +sqrt(3)*xaxis -height*2)<0) & ((
               yaxis +sqrt(3)*xaxis +height*2)>0);
    bool_out = ~bool_in;

    if(bool_in)
        count_in = 1;
        count_out =0;
        x_in(count_in,1) = 0;
        y_in(count_in,1) = 0;
```

```
else
    count_in = 1;
    % the location of the last hexagon that a ray has
       been traced to.
    x_in(count_in,1) = sour_cen(1);
    x_in(count_in,2) = sour_cen(1);
    y_in(count_in,1) = sour_cen(2);
    y_in(count_in,2) = sour_cen(2);
    count_out = 1;
    x_out(count_out,1) = sour_cen(1);
    y_out(count_out,1) = sour_cen(2);

    count_out = 1;
end
slope = tan(angle_cur);

% check the rest pixels
radius_leng = [0:tracing_step:store_radius]';
x = radius_leng*cos(angle_cur) + sour_cen(1);
y = radius_leng*sin(angle_cur) + sour_cen(2);
data = zeros(tracing_N,1);
sep_temp = 0;
for j = 2:tracing_N +1

    bool = 0;
    for k = 1:cen_N
        xaxis = x(j)-cen_x_curr(k);
        yaxis = y(j)-cen_y_curr(k);
            % whether a pixel is within these 19
               hexagons
        bool_cen(k) = (yaxis>-height) & (yaxis<height) &
            ((yaxis -sqrt(3)*xaxis -height*2)<0) & ((
           yaxis -sqrt(3)*xaxis +height*2)>0) ...
        &  ((yaxis +sqrt(3)*xaxis -height*2)<0) & ((
           yaxis +sqrt(3)*xaxis +height*2)>0);
        bool = bool|bool_cen(k);
    end

    if(bool_in & bool)
            % rays move in the hole
        data(j) = sep_temp;
        continue;
    elseif(bool_in & (~bool))
            % if a pixel is moved from a hole to septa,
               the 19 hexagons should be defined
```

```
            bool_in = 0;
            data(j) = sep_temp;
            x_in(count_in,2) = x(j-1);
            y_in(count_in,2) = y(j-1);
            count_out = count_out+1;
            x_out(count_out,1) = x(j);
            y_out(count_out,1) = y(j);

            count_index = 0;
            for m = -2:2
                for n = -4:4
                    sum_index = abs(m) + abs(n);
                    if(sum_index == 2 | sum_index == 4 |
                       sum_index == 0)
                        count_index = count_index+1;
                        cen_x_curr(count_index) = cen_x + m*
                            halfstep_x;
                        cen_y_curr(count_index) = cen_y + n*
                            halfstep_y;
                    end
                end
            end


        elseif((~bool_in) & (~bool))
                % rays move in the septa
            data(j) = sqrt( (x(j)-x_in(count_in,2))^2 + (y(j
                )-y_in(count_in,2))^2 ) + sep_temp;
            continue;
        elseif((~bool_in) & (bool))
                % rays move from septa to a hole, the
                    central hole and side holes should be
                    redefined.
            bool_in = 1;
            x_out(count_out,2) = x(j-1);
            y_out(count_out,2) = y(j-1);

            count_in = count_in+1;
            x_in(count_in,1) = x(j);
            y_in(count_in,1) = y(j);
            sep_temp = data(j-1);
            data(j) = sep_temp;
            for k = 1:cen_N
                if(bool_cen(k))
                    cen_x = cen_x_curr(k);
```

```
                        cen_y = cen_y_curr(k);
                    end

                end
            end
        end
        if(bool_in)
            x_in(count_in,2) = x(j);
            y_in(count_in,2) = y(j);
        else
            x_out(count_out,2) = x(j);
            y_out(count_out,2) = y(j);
        end

        %plot(data);hold on;drawnow;

        if(max(data(:))>1000)
            error('terrible!');
        end
        data2 = data(2:tracing_N+1,1);
%       plot(data);hold on;
%       drawnow;
        fid = fopen(filename,'a');
        fwrite(fid,data2,'single');
        fclose(fid);
        clear x_in;
        clear y_in;
        clear x_out;
        clear y_out;
        clear data2;

end
```

B.3 Septal Penetration Modeling

```
function projdata = seppene(proj_info , colli_info , sour_info ,
    filename , store_coef , bool_thick)
%projdata =
%seppene([pixels , pixelsize],[colli_side_len , colli_leng ,
    colli_sep_thick ,miu, colli_rot_angle],[sou_dis , max_angle],
    filename ,[angle_N , angle_N_step , ray_pixel_N ,
    ray_pixel_N_step , ray_total_leng], bool_thick)
%projdata_all = seppene([128,0.442],[0.4/sqrt(3)
    ,6.6,0.18,3.12,15],[zz,30],'
    ray_angle360_angleN10000_radius80_radiusN20000
    ',[10000,10,20000,10,80],1);
pixels = proj_info(1);
pixelsize = proj_info(2);
colli_side_leng = colli_info(1,1);
colli_leng = colli_info(2);
colli_sep_thick = colli_info(3);
miu = colli_info(4);
colli_rot_angle = colli_info(5)/180*pi;
sour_dis = sour_info(1,1);
max_angle = sour_info(2);

angle_N = store_coef(1);
angle_N_step = store_coef(2);
ray_pixel_N = store_coef(3);
ray_pixel_N_step = store_coef(4);
ray_total_leng = store_coef(5);

if(mod(pixels,2) == 0)
    mtxsize = pixels+1;
else
    mtxsize = pixels;
end
cen_x = (mtxsize+1)/2;
cen_y = (mtxsize+1)/2;

matrix_length = mtxsize * pixelsize;
projdata = zeros(mtxsize, mtxsize);
projdata_count = zeros(mtxsize, mtxsize);
halflength = matrix_length/2;

step_x = colli_side_leng * 3  + colli_sep_thick/sqrt(3)*4;
step_y = step_x * sqrt(3)/3;
```

```
halfstep_x = step_x/2;
halfstep_y = step_y/2;
halfpixelsize = pixelsize/2;

%[x,y,num_x,num_y] = collihexcenter(step_x,step_y,
    matrix_length);
ray_angle_step = 2*pi/angle_N;
ray_pixel_step = ray_total_leng/ray_pixel_N;

sour_front_dis = sour_dis;
sour_back_dis = sour_dis+colli_leng;
data_ray_sept = zeros(ray_pixel_N,1);
angle_theta_N = 12;
fid = fopen(filename,'r');

% read 2D septal thickness of the ray projections.
for i = 1:angle_N_step:angle_N
    fseek(fid, (i-1)*4*ray_pixel_N,-1);
    data_ray_sept = fread(fid,ray_pixel_N,'single');
    theta = ray_angle_step * (i-1);
    angle_theta = angleconvert(theta,colli_rot_angle);
% calculate angle theta
    for j = 1:ray_pixel_N_step:ray_pixel_N
            dis_back = ray_pixel_step*j;
            dis_front = dis_back*sour_front_dis/
               sour_back_dis;
            point_front = floor(dis_front/ray_pixel_step);
            projangle = atan(dis_back/sour_back_dis);

            if(point_front == 0)
                thick = data_ray_sept(j);
            else
               thick = data_ray_sept(j) - data_ray_sept(
                  point_front);
            end
%              if(thick~=0 & bool_thick == 1) % collimator
    response
%                 continue;
%              end
            if(thick == 0 & bool_thick==2) % septal
               penetration
                continue;
            end
%              k_thick(j) = thick;
```

```
            dis3D = thick/sin(projangle);
% recover the 3D septal thickness that a ray travel through
            for m = 1:angle_theta_N;
                x = dis_front*cos(angle_theta(m));
                y = dis_front*sin(angle_theta(m));
                point_x_proj = floor(x/pixelsize) + cen_x;
                point_y_proj = floor(y/pixelsize) + cen_y;
                if(point_x_proj>0 & point_x_proj<=mtxsize &
                   point_y_proj>0 & point_y_proj<=mtxsize )
                    projdata(point_y_proj,point_x_proj) =
                       exp(-miu*dis3D)+ projdata(
                       point_y_proj,point_x_proj);
                    projdata_count(point_y_proj,point_x_proj
                       ) = projdata_count(point_y_proj,
                       point_x_proj) +1;
                end


            end
        end
end
fclose(fid);
clear data_ray_sept
projdata = projdata./(projdata_count+eps);
```

B.4 Monte Carlo based Forward Projection

```
function outSino = forward_static_MC(obj, attFile, isotope, smc
    , ppct, forwProjN, SA, nn, amount, projTime, bool)
global totalA projN startA heads pixels slice ps

souFile = strcat(smc, '.smi');
denFile = strcat(smc, '.dmi');
smcFile = strcat(smc, '.smc');
MC_resFile = 'mc_res';
MC_resRead = strcat(MC_resFile, '.dat');

attData = readimages(attFile, 'l', 'uint32', 0, [pixels, pixels,
    slice]);
writeimages(attData, denFile, 'l', 'uint32');
clear attData;

outSino = zeros(slice, pixels, forwProjN*heads);

% rotate angle step
angleP = totalA/forwProjN;
angleH = totalA/heads;
if(bool)
    index = find(obj(:)>0);
    data = obj(index);
    min_data = min(data);
    max_data = max(data);
    obj = (obj-min_data)/(max_data-min_data)*50;
end

writeimages(obj, souFile, 'l', 'uint32');
clear obj

% run Monte Carlo to get projection image
for i = 1:forwProjN
    for j = 1:heads
        angle = angleP*(i-1) + (j-1)*angleH + SA;
        run = sprintf('!/home/shannon/sim0901/%s/%s_%s_%s/px
            :%f/nn:%d/41:%d/29:1/25:%f', isotope, ppct, smcFile,
            MC_resFile, ps, nn, angle, 1);
        eval(run);
        temp = readimages(MC_resRead, 'l', 'single', 0, [pixels,
            slice]);
        outSino(:,:, i+(j-1)*forwProjN) = temp'*projTime*
            amount;
```

```
    end
end
```

B.5 Back-projection

```
function obj = backproj_static(inSino,cummFile,SA,GR)

global totalA projN startA heads pixels slice ps

N = size(inSino,3);
backProjN = N/heads;
proj_step = projN/backProjN;

angleP = totalA/projN;
angle_backP = totalA/backProjN;
angleH = totalA/heads;

pixels_num = pixels*pixels*slice;
index = (SA-startA)/angleP;
p_index = pixels_num*heads*index*4;

obj = zeros(pixels,pixels,slice);


for i = 1:backProjN
    for j = 1:heads
        angle = angle_backP*(i-1) + angleH*(j-1) + SA;
        p =p_index+pixels_num*heads*proj_step*(i-1)*4+
            pixels_num*(j-1)*4;
        att= readimages(cummFile,'l','single',p,[pixels,
            pixels,slice]);
%           att = exp(-att*ps);

        data = zeros(pixels,pixels,slice);
        rotData = zeros(pixels,pixels,slice);
        % trace rays back to the object, following the
            pattern of geomtric response
        for m = 1:pixels
            temp_conv = conv2(inSino(:,:,i+(j-1)*backProjN),
                GR(:,:,m));
            [col,row] = size(temp_conv);
            cenx = floor(col/2);
            ceny = floor(row/2);
            if(mod(slice,2) == 0)
                temp = temp_conv(cenx-slice/2+1:cenx+slice
                    /2,ceny-pixels/2+1:ceny+pixels/2);
            else
                temp = temp_conv(cenx-(slice-1)/2+1:cenx+(
```

```
                    slice+1)/2,ceny-pixels/2+1:ceny+pixels/2)
                    ;
                end
                data(:,m,:) = permute(temp,[2,3,1]);
                data(:,m,:) = data(:,m,:).*att(:,m,:);
            end
            for k = 1:slice
                rotData(:,:,k) = rotate2D(data(:,:,k),angle);
            end
            obj = obj + rotData;
        end
    end
```

B.6 Single-isotope Reconstruction

```
function [obj,amount,amount_end] = osem_MC(init_obj,
    init_amount,isotope,simind_type,inSino,attFile,cummFile,
    smc,GR,group_osem,nn,projTime,iters)

global totalA projN startA heads pixels slice ps

subset = projN/group_osem;
angleP = totalA/projN;
angleH = totalA/heads;
pixels_num = pixels*pixels*slice;

ROI = cylinder3D([pixels,slice],[1,slice],pixels/2-2);
obj = init_obj;
clear init_obj
amount = init_amount;

sino = inSino;


temp = zeros(slice,pixels,group_osem*heads) + 1;

bk = zeros(pixels,pixels,slice,subset);
%calculate the denominator term in the OS-EM updating
    function
for i = 1:subset;
    SA = angleP*(i-1)+startA;
    bk(:,:,:,i) = backproj_static(temp,cummFile,SA,GR);
end
writeimages(bk,'single_bk.dat','l','single');


file_bk = sprintf('%s_bk.dat',isotope);
bool = 0;
for i = 1:iters
    for j = 1:subset
        p = pixels*pixels*slice*4*(j-1);
        bk = readimages(file_bk,'l','single',p,[pixels,
            pixels,slice]);
        SA = angleP*(j-1)+startA;
        ppct = simind_type;
        %forward projection
        fobj = forward_static_MC(obj,attFile,isotope,smc,
            ppct,group_osem,SA,nn,amount,projTime,bool);
```

```
        if(bool==0)
            bool = 1;
        end
        factor_est = sum(sum(sum(sino(:,:,j:subset:end))))/
           sum(sum(sum(fobj)));

        %update activity
        amount = amount*factor_est;
        fobj = fobj*factor_est;

        %take ratios of projection image
        ratio = ((sino(:,:,j:subset:end)))./(fobj+eps);
        ratio(find(fobj(:)<0.1))=0;

        %backproject the ratio
        temp_backproj = backproj_static(ratio,cummFile,SA,GR
           );

        %update the object
        obj = (temp_backproj)./(bk+eps).*obj.*ROI;
        save temp_obj obj amount
        amount_end(i,j) = amount;
    end
end
```

B.7 Dual-isotope Reconstruction

```
function [object1,activity1,object2,activity2] =
   OSEM_MC_dual_Isotope(object1,activity1,proj1,object2,
   activity2,proj2,isotope1,isotope2,attFile1,attFile2,
   cummFile1,cummFile2,GR,iters,spe);
global pixels slice ps projN group totalA startA heads
   projTime ROI gr_len fileload

inSino1 = proj1;
inSino2 = proj2;

angleS = totalA/group;
angleH = totalA/heads;
angleP = totalA/projN;

subset = projN/group;
pixels_num = pixels*pixels*slice;

%calculate the denominator term for both isotopes
roi_img = ROI;
BP_unitSino_denoFile = strcat(fileload,'
   temp_BP_unitSino_deno.dat');
BP_unitout_denoFile = strcat(fileload,'temp_BP_unitout_deno.
   dat');
temp = zeros(slice,pixels,group*heads) + 1;
writeimages(temp,BP_unitSino_denoFile,'l','single');
bk1 = zeros(pixels,pixels,slice,subset);
for i = 1:subset;
    SA = angleP*(i-1)+startA;
    bk1(:,:,:,i) = backproj_static(temp,cummFile1,SA,GR);
end
writeimages(bk1,'dual_bk1_heart_tc_i123.dat','l','single');
clear bk1

bk2 = zeros(pixels,pixels,slice,subset);
for i = 1:subset;
    SA = angleP*(i-1)+startA;
    bk2(:,:,:,i) = backproj_static(temp,cummFile2,SA,GR);
end
writeimages(bk2,'dual_bk2_heart_tc_i123.dat','l','single');
clear bk2

FP_out_staticFile = strcat(fileload,'temp_FP_out_static.dat'
   );
```

```
ratio_staticFile = strcat(fileload ,'temp_ratio_static.dat');
BP_out_staticFile = strcat(fileload ,'temp_BP_out_static.dat'
    );
file1 = sprintf('%s_bk.dat',isotope1);
file2 = sprintf('%s_bk.dat',isotope2);

for i = 1:iters
    for j = 1:subset
        nn = 1;
        if(i==1&&j==1)
            bool_data = 0;
        else
            bool_data = 1;
        end
        SA = angleP*(j-1)+startA;

        p = pixels*pixels*slice*4*(j-1);
        bk1 = readimages(file1 ,'l','single',p,[pixels,pixels
            ,slice]);
        bk2 = readimages(file2 ,'l','single',p,[pixels,pixels
            ,slice]);

        if(strcmp(isotope1 ,'tc99m'))
            smc = sprintf('%s%d','tc99m_',pixels);
        elseif(strcmp(isotope1 ,'tl201'))
            smc = sprintf('%s%d','tl201_',pixels);
        elseif(strcmp(isotope1 ,'i123'))
            smc = sprintf('%s%d','i123_',pixels);
        end
        ppct = sprintf('simind_cfd_%d_%d',spe(1),spe(2));

        %foward project the four image sets
        fobj_1_pp = forward_static_MC(object1,attFile1,
            isotope1,smc,ppct,group,SA,nn,activity1,projTime,
            bool_data);

        ppct = sprintf('simind_cfd_%d_%d',spe(3),spe(4));
        fobj_1_ct = forward_static_MC(object1,attFile1,
            isotope1,smc,ppct,group,SA,nn,activity1,projTime,
            bool_data);


        if(strcmp(isotope2 ,'tc99m'))
            smc = sprintf('%s%d','tc99m_',pixels);
        elseif(strcmp(isotope2 ,'tl201'))
```

```
        smc = sprintf('%s%d','tl201_',pixels);
    elseif(strcmp(isotope2,'i123'))
        smc = sprintf('%s%d','i123_',pixels);
    end

    ppct = sprintf('simind_cfd_%d_%d',spe(3),spe(4));

    fobj_2_pp =  forward_static_MC(object2,attFile2,
        isotope2,smc,ppct,group,SA,nn,activity2,projTime,
        bool_data);

    ppct = sprintf('simind_cfd_%d_%d',spe(1),spe(2));
    fobj_2_ct = forward_static_MC(object2,attFile2,
        isotope2,smc,ppct,group,SA,nn,activity2,projTime,
        bool_data);

    %combine the appropriate images together
    fobj_1 = fobj_1_pp+fobj_2_ct;
    fobj_2 = fobj_1_ct +fobj_2_pp;

    %take ratio
   if(max(fobj_1(:))>100)
        ratio_1 = (inSino1(:,:,j:subset:end)+1)./(fobj_1
            +eps+1);
    elseif(max(fobj_1(:))>10)
        ratio_1 = (inSino1(:,:,j:subset:end)+0.1)./(
            fobj_1+eps+0.1);
    else
        ratio_1 = (inSino1(:,:,j:subset:end)+0.01)./(
            fobj_1+eps+0.01);
   end

    %update the activity
    act_1_est = sum(sum(sum(inSino1(:,:,j:subset:end))))
        /sum(fobj_1(:));
    f_1 = sum(fobj_1_pp(:))/( sum(fobj_1_pp(:)) + sum(
        fobj_2_ct(:)));
    activity1 = activity1*act_1_est ;

    writeimages(ratio_1,ratio_staticFile,'l','single');

    %back-project the ratio
    temp_BP = backproj_static(ratio_1,cummFile1,SA,GR);

    object1 = object1/sum(object1(:))*activity1;
```

```
        object1 = temp_BP./(bk1+bk2+eps).*object1*2;
        object1(find(object1(:)==NaN)) = 0;

        if(max(fobj_2(:))>100)
            ratio_2 = (inSino2(:,:,j:subset:end)+1)./(fobj_2
               +eps+1);
        elseif(max(fobj_2(:))>10)
            ratio_2 = (inSino2(:,:,j:subset:end)+0.1)./(
               fobj_2+eps+0.1);
        else
            ratio_2 = (inSino2(:,:,j:subset:end)+0.01)./(
               fobj_2+eps+0.01);
        end

        act_2_est = sum(sum(sum(inSino2(:,:,j:subset:end))))
           /sum(fobj_2(:));
        f_2 = sum(fobj_2_pp(:))/( sum(fobj_1_ct(:)) + sum(
           fobj_2_pp(:)));
        activity2 = activity2*act_2_est ;
        writeimages(ratio_2,ratio_staticFile,'l','single');

        temp_BP = backproj_static(ratio_2,cummFile2,SA,GR);

        object2 = object2/sum(object2(:))*activity2;
        object2 = temp_BP./(bk1+bk2+eps).*object2*2;
        object2(find(object2(:)==NaN)) = 0;
    save res_dual object1 activity1 object2 activity2

  end
end
```

References

[1] R. D. Badawi. Nuclear Medicine. *Physics Education*, 36:452–459, 2001.

[2] S. R. Cherry, J. A. Sorenson, and M. E. Phelps. *Physics in Nuclear Medicine.* Elsevier Science, California, third edition, 2003.

[3] T. H. Farncombe. *Functional Dynamic SPECT Imaging using a Single Slow Camera Rotation.* Ph.D. Thesis, 2000.

[4] J. Harbert. *Textbook of Nuclear Medicine Volume II: Clinical Application.* Lea and Febiger, Washington, D.C., 1984.

[5] R. L. V. Heertum and R. S. Tikofsky. *Functional Cerebral SPECT and PET Imaging.* Lippincott Williams and Wilkins, New York, 1995.

[6] M. F. D. Carli and M. J. Lipton. *Cardiac PET and PET/CT Imaging.* Springer Science, New York, USA, 2007.

[7] Y. Gur, T. Farncombe, P. Pretorius, H. Gifford, M. Narayanan, E. Frey, D. Gagnon, and M. King. Comparison of Scatter Compensation Strategies for Myocardial Perfusion Imaging using Tc-99m Labeled Sestamibi. *IEEE Trans Nucl Sci*, 49:2309–2314, 2002.

[8] A. F. Robertson, P. J. Roach, M. A. Shields, and D. L. Bailey. Tc-99m sestamibi myocardial perfusion imaging after undisclosed i-131 therapy. *J Nucl Cardiol*, 13(5):722–724, 2006.

[9] P. P. Steele, D. L. Kirsch, and J. E. Koss. Comparison of simultaneous dual-isotope multipinhole spect with rotational spect in a group of patients with coronary artery disease. *J Nucl Med*, 49(7):1080–1089, 2008.

[10] M. Nakamura, K. Takeda, T. Ichihara, N. Motomura, H. Shimizu, Y. Saito, Y. Nomura, N. Isaka, T. Konishi, and T. Nakano. Feasibility of Simultaneous Stress 99mTc-Sestamibi/Rest 201Tl Dual-Isotope Myocardial Perfusion SPECT in the Detection of Coronary Artery Disease. *J Nucl Med*, 40:895–903, 1999.

[11] M. P. Larock, S.H.Braat, H. Sochor, M. Masiey, and P. Rigo. *New Developments in Myocardial Imaging Technetium Sestamibi.* Martin Dunitz, London NW, 1993.

[12] K. Baete, J. Nuyts, W. Van Paesschen, P. Suetens, and P. Dupont. Anatomical-based FDG-PET Reconstruction for the Detection of Hypo-Metabolic Regions in Epilepsy. *IEEE Trans Med Imaging*, 23:510–519, 2004.

[13] S. L. Jae, S. L. Dong, K. Seok-Ki, L. Sang-Kun, C. June-Key, and C. L. Myung. Localization of Epileptogenic Zones in F-18 FDG Brain PET of Patients with Temporal Lobe Epilepsy using Artificial Neural Network. *IEEE Trans Med Imaging*, 19:347–355, 2000.

[14] D. A. Lipson and E. J. R. van Beek. *Functional Lung Imaging.* Taylor and Francis, Albuquerque, NM, 2005.

[15] K. J. Pandya, J. R. Brahmer, and M. Hidalgo. *Lung Cancer: Translational and Emerging Therapies.* Informa Healthcare, New York, 2007.

[16] J. Harbert. *Textbook of Nuclear Medicine Volume I: Basic Science.* Lea and Febiger, Washington, D.C., 1984.

[17] J. Frank. Itroduction to Imaging Bone and Joint. *StudentBMJ*, 12:101–105, 2004.

[18] S. Shamim, R. Kumar, G. Bandopadhyaya, J. Shukla, D. Halanaik, T. Mohapatra, M. Chawla, A. Malhotra, and C. Bal. Role of Tc99m-MDP Bone Scan in Prognostication of Radiosynovectomy. *J Nucl Med*, 48:287p, 2007.

[19] S. Challa and J. H. Miller. Extraskeletal Uptake of Technetium-99m-MDP in Sites of Heparin Administration. *J Nucl Med*, 39:893–895, 1998.

[20] P. J. Pellere, V. B. Ho, and M. J. Kransdorf. Extraosseous Tc-99m MDP Uptake: a Pathophysiologic Approach. *Radiographics*, 13:715–734, 1993.

[21] W. R. Cattell, J. A. W. Webb, and A. J. W. Hilson. *Clinical Renal Imaging*. John Wiley and Sons, New York, 1989.

[22] T. Farncombe, A. Celler, D. Noll, J. Maeght, and R. Harrop. An Evaluation of Dynamic SPECT Imaging Methods. *IEEE Nuclear Science Symposium*, 3:1959–1963, 1998.

[23] F. A. Mettler. *Radionuclide Imaging of the GI Tract*. Churchchill Livingstone, New York, 1986.

[24] G. Muehllehner and J. Dudek. Influence of Hole Shape on Collimator Performance. *Phys Med Biol*, 12:242–250, 1976.

[25] D. J. de Vries and S. C. Moore. Comparieson of Hexagonal-Hole and Square-Hole Collimation by Monte Carlo Simulation. *IEEE Nuclear Science Symposium Conference Record*, 3:22/52–22/56, 2000.

[26] C. E. Metz, F. B. Atkins, and R. N. Beck. The Geometric Transfer Function Component for Scintillation Camera Collimators with Straight Parallel holes. *Phys Med Biol*, 25:1059–1070, 1980.

[27] R. N. Beck and L. D. Redtung. Collimator Design using Ray-tracing Techniques. *IEEE Trans Nucl Sci*, NS-32(1):257–272, 1985.

[28] F. W. III. Scintillators. In M. N. Wernick and J. N. Aarsvold, editors, *Emission Tomography-The Fundamentals of PET and SPECT*, pages 229–233. Elsevier, Nashville, Tennesee, 2004.

[29] S. R. Deans. *The Radon Transform and Some of Its Application.* Jone Wiley and Sons, New York, 1983.

[30] L. A. Shepp and Y. Vardi. Maximumm Likelihood Estimation for Emission Tomography. *IEEE Trans Med Imaging*, 1:113–121, 1982.

[31] H. M. Hudson and R. S. Larkin. Accelerated Image Reconstruction using Ordered Subsets of Projection Data. *IEEE Trans Med Imaging*, 13:601–609, 1994.

[32] D. S. Lalush and B. M. W. Tsui. Performance of Ordered-Subset Reconstruction Algorithms Under Conditions of Extreme Attenuation and Truncation in Myocardial SPECT. *J Nucl Med*, 41:737–744, 2000.

[33] L. T. Chang. A Method for Attenuation Correction in Radionuclide Computed Tomography. *IEEE Trans Nucl Sci*, 25:638–642, 1978.

[34] K. Murase, H. Itoh, and H. Mogami. A Comparative Study of Attenuation Correction Algorithms in Single Photon Emission Computed Tomography (SPECT). *J Nucl Med*, 13:55–62, 1987.

[35] M. Ljungberg and S. E. Strand. Attenuation Correction in SPECT based on Transmission Studies and Monte Carlo Simulations of Build-up Functions. *J Nucl Med*, 31:493–500, 1990.

[36] M. A. King, B. M. Tsui, T. S. Pan, S. J. Glick, and E. J. Soares. Attenuation compensation for cardiac single-photon emission computed tomographic imag-

ing: Part 2. attenuation compensation algorithms. *J Nucl Cardiol*, 3(1):55–64, 1996.

[37] M. Ljungber, M. A. King, G. J. Hademenos, and S. E. Strand. Comparison of Four Scatter Correction Methods Using Monte Carlo Simulated Source Distributions. *J Nucl Med*, 35:143–151, 1994.

[38] M. A. King, G. J. Hademenos, and S. J. Glick. A Dual-photopeak Window Method for Scatter Correction. *J Nucl Med*, 33(4):605–612, 1993.

[39] G. J. Hademenos, M. Ljungberg, M. A. King, and S. J. Glick. A Monte-Carlo Investigation of the Dual Photopeak Window Scatter Correction Method [SPECT]. *IEEE Trans Nucl Sci*, 40(2):179–185, 1993.

[40] M. Y. Paek, J. S. Lee, D. S. Lee, J. K. Chung, and M. C. Lee. Crosstalk and Scatter Correction in Simultaneous Dual Isotope SPECT Imaging using Four Energy Windows Method. *IEEE Nuclear Science Symposium Record*, 2:13/153–13/156, 2000.

[41] T. Ichihara, K. Ogawa, N. Motomura, A. Kubo, and S. Hashimoto. Compton Scatter Compensation using the Triple-Energy Window Method for Single-and Dual-isotope SPECT. *J Nucl Med*, 34:2216–2221, 1993.

[42] R. G. Wells, A. Celler, and R. Harrop. Analytical Calculations of Cross-Talk for Dual-Isotope SPECT Projections. *IEEE Trans Nucl Sci*, 47:1202–1209, 2000.

[43] R. J. Jaszczak, K. L. Greer, C. E. Floyd, C. C. Harris, and R. E. Coleman. Improved SPECT Quantification Using Compensation for Scattered Photons. *J Nucl Med*, 25:893–900, 1984.

[44] K. Ogawa, Y. Harata, T. Ichihara, A. Kubo, and S. Hashimoto. A Practical

Method for Position Dependent Compton-scatter Correction in Single Photon Emission CT. *IEEE Trans Nucl Sci*, 10(3):408–412, 1991.

[45] F. J. Beekman, H. W. A. M. de Jong, and E. Slijpen. Efficient SPECT Scatter Calculation in Non-uniform Media using Correlated Monte Carlo Simulation. *Phys Med Biol*, 44:183–192, 1999.

[46] M. King, P. W. Doherty, and R. B. Schwinger. Fast Count-Dependent Digital Filtering of Nuclear Medicine Images: Concise Communication. *J Nucl Med*, 24:1039–1045, 1983.

[47] M. King, P. W. Doherty, and R. B. Schwinger. A Wiener Filter for Nuclear Medicine Images. *Med Phys*, 10:876–880, 1983.

[48] M. King, R. B. Schwinger, and P. W. Doherty. Two-Dimensional Filtering of SPECT Images using the Metz and Wiener Filters. *J Nucl Med*, 25:1234–1240, 1984.

[49] C. R. Appledorn. An Analytical Solution to the Nonstationary Reconstruction Problem in Single Photon Emission Computed Tomography. *Prog Clin Biol Res*, 363:67–79, 1991.

[50] E. J. Soares, C. L. Byrne, and S. J. Glick. Implementation and Evluation of an Analytical Solution to the Photon Attenuation and Nonstationary Resolution Reconstruction Problem in SPECT. *IEEE Trans Nucl Sci*, 40:1231–1237, 1993.

[51] W. H. Press, S. A. Teukolsky, W. T. Vetterling, and B. P. Flannery. *Numerical Recipes in Fortran 77*. Syndicate of the University of Camberidge, 1992.

[52] M. Ljungberg, S. Strand, and M. King. *Monte Carlo Calculations in Nuclear Medicine*. Institute of Physics Publishing, London, 1998.

[53] M. J. Berger and J. H. Hubbell. XCOM: Photon Cross Sections on a Personal Computer. *NBSIR 87-3597, National Bureau of Standards*, 1987.

[54] C. Levin. Basic Physics of Radionuclide Imaging. In M.N.Wernick and J.N.Aarsvold, editors, *Emission Tomography-The Fundamentals of PET and SPECT*, pages 153–168. Elsevier, Nashville, Tennesee, 2004.

[55] S. Weinberg. *The Quantum Theory of Fields.* Camberidge University, Cambridge, United Kingdom, 1995.

[56] J. H. Hubbell, J. Veigle, E. Briggs, R. Brown, D. Cramer, and R. Howerton. Atomic form factors, incoherent scattering functions, and photon scattering cross sections. *J Phys Chem Ref Data*, 4:471–616, 1975.

[57] M. Ljungberg, A. Larsson, and L. Johansson. A New Collimator Simulation in SIMIND Based on the Delta-Scattering Technique. *IEEE Trans Nucl Sci*, 52(5):1370–1375, 2005.

[58] G. E. P. Box and S. H. Muller. A Note on the Generation of Random Normal Deviates. *Ann Math Stat*, 29:610–611, 1958.

[59] M. Ljungberg. Simulation Techniques and Phantoms. In M.N.Wernick and J.N.Aarsvold, editors, *Emission Tomography-The Fundamentals of PET and SPECT*, pages 551–563. Elsevier, Nashville, Tennesee, 2004.

[60] I. G. Zubal and C. R. Harrell. Voxel based Monte Carlo Calculations of Nuclear Medicine Images and Applied Variance Reduction Techniques. *Image Vis Comput*, 10:342–348, 1993.

[61] I. G. Zubal and C. R. Harrell. Computerized Three-dimensional Segmented Human Anatomy. *Med Phys*, 21:299–302, 1994.

[62] W. P. Segars, D. S. Lalush, and B. M. W. Tsui. Modeling Respiratory Me-

chanics in the MCAT and Spline-based MCAT Phantoms. *IEEE Trans Nucl Sci*, 48:89–97, 2001.

[63] W. P. Segars. *Development of a New Dynamic NURBS-based Cardiac-Torso (NCAT) Phantom*. Ph.D. dissertation, University of Northh Carolina at Chapel Hill, 2001.

[64] W. P. Segars, B. M. W. Tsui, E. C. Frey, G. A. Johnson, and S. S. Berr. Development of a 4d Digital Mouse Phantom for Molecular Imaging Research. *Mol Imaging Biol*, 6:149–159, 2004.

[65] B. M. W. Tsui, J. A. Terry, and G. T. Gullberg. Evaluation of Cardiac Cone-beam Single Photon Emission Computed Tomography using Observer Performance Experiments an Receiver Operating Characteristic Analyss. *Investigative Radiology*, 28:1101–1112, 1993.

[66] W. S. Snyder, H. L. Fisher, M. R. Ford, and G. G. Warner. Estimates of Absorbed Fractions for Monoenergetic Photon Sources Uniformely Distributed in Various Organs of A Heterogeneous Phantom: MIRD Pamphlet. *J Nucl Med*, 10:7–52, 1969.

[67] P. H. Pretorius, W. Xia, M. A. King, B. M. W. Tsui, T. S. Pan, and B. J. Villegas. Determination of Left and Right Ventricular Volume and Ejection Fraction using a Mathematical Cardiac Torso Phantom for Gated Blood Pool SPECT. *J Nucl Med*, 38:1528–1535, 1997.

[68] D. S. Lalush and B. M. W. Tsui. Block-iterative Techniques for Fast 4d Reconstruction using a Priori Motion Models in Gated Cardiac SPECT. *Phys Med Biol*, 43:875–887, 1998.

[69] N. J. Carron. *An Introduction to the Passage of Energetic Particles Through Matter*. Taylor and Francis Group, New York, 2007.

[70] J. J. DeMarco, R. E. Wallace, and K. Boedeker. An Analysis of MCNP Cross-Sections and Tally Methods for Low-Energy Photon Emitters. *Phys Med Biol*, 47:1321–1332, 2002.

[71] H. Zaidi, C. Labbe, and C. Morel. Improvement of the Performance and Accuracy of PET Monte Carlo Simulations. *Proceedings of SPIE, the International Society for Optical Engineering*, 3659(2):582–593, 1999.

[72] M. Ljungberg and S. Strand. A Monte Carlo Program for the Simulation of Scintillation Camera Characteristics. *Comput Methods Programs Biomed*, 29:257–272, 1989.

[73] T. H. Farncombe, S. Liu, M. A. King, A. B. Brill, and M. G. Stabin. Accelerated SPECT Monte Carlo Simulation using Convolution-based Forced Detection. *2006 Society of Nuclear Medicine Annual Conference*, 2006.

[74] H. W. A. M. de Jong, E. T. P. Slijpen, and F. J. Beekman. Acceleration of Monte Carlo SPECT Simulation using Convolution-based Forced Detection. *IEEE Trans Nucl Sci*, 48:58–64, 2001.

[75] M. A. King, S. J. Glick, P. H. Pretorius, R. G. Wells, H. C. Gifford, M. V. Narayanan, and T. H. Farncombe. Attenuation, Scatter,and Spatial Resolution Compensation in SPECT. In M. N. Wernick and J. N. Aarsvold, editors, *Emission Tomography-The Fundamentals of PET and SPECT*, pages 473–498. Elsevier, Nashville, Tennesee, 2004.

[76] L. Bouwens, R. V. de Walle, J. Nuyts, M. Koole, Y. D'Asseler, S. Vandenberghe, I. Lemahieu, and R. A. Dierckx. Image-correction Techniques in SPECT. *Comput Med Imaging Graph*, 25:117–226, 2001.

[77] J. W. Beck, R. J. Jaszczak, R. E. Coleman, C. F. Sterner, and P. Nolte. Analysis of SPECT including Scatter and Attenuation using Sophisticated Monte Carlo Modeling Methods. *IEEE Trans Nucl Sci*, 29:506–511, 1982.

[78] S. Liu, M. A. King, A. B. Brill, M. G. Stabin, and T. H. Farncombe. Accelerated SPECT Monte Carlo Simulation Using Multiple Projection Sampling and Convolution-based Forced Detection. *IEEE Trans Nucl Sci*, 55:560–567, 2008.

[79] H. W. A. M. de Jong and F. J. Beekman. Rapid SPECT Simulation of Downscatter in Non-uniform Media. *phys. Med. Biol.*, 46:621–635, 2001.

[80] G. Muehllehner and H. Luig. Septal Penetration in Scintillation Camera Collimators. *Phys Med Biol*, 18(6):855–862, 1973.

[81] Y. Du, E. C. Frey, W. T. Wang, C. Tocharoenchai, W. H. Baird, and B. M. W. Tsui. Combination of MCNP and SimSET for Monte Carlo Simulation of SPECT With Medium- and High-Energy Photons. *IEEE Trans Nucl Sci*, 49:668–674, 2002.

[82] X. Song, W. P. Segars, Y. Du, B. M. W. Tsui, and E. C. Frey. Fast Modelling of the Collimator-Detector Response in Monte Carlo Simulation of SPECT Imaging using the Angular Response Function. *Phys Med Biol*, 50:1791–1804, 2005.

[83] S. Staelens, T. de Wit, and F. Beekman. Fast Hybrid SPECT Simulation including Efficient Septal Penetration Modelling (SP-PSF). *Phys Med Biol*, 52:3027–3043, 2007.

[84] D. P. Lewis, B. M. W. Tsui, C. Tocharoenchai, and E. C. Frey. Characterization of Medium and High Energy Collimators using Ray-tracing and Monte Carlo Methods. *Proceedings of 1998 IEEE Nuclear Science Symposium and Medical Imaging Conference*, 3:2026–2030, 1998.

[85] D. L. Gunter. Collimator Design for Nuclear Medicine. In M.N.Wernick and J.N.Aarsvold, editors, *Emission Tomography-The Fundamentals of PET and SPECT*, pages 153–168. Elsevier, Nashville, Tennesee, 2004.

[86] R. Brooks and G. D. Chiro. Principles of Computer Assisted Tomography (CAT) in Radiographic and Radioisotopic Imaging. *Phys Med Biol*, 21:689–732, 1976.

[87] E. C. Frey and B. M. W. Tsui. Collimator-Detector Response Compensation in SPECT. In H. Zaidi, editor, *Quantitative Analysis in Nuclear Medicine Imaging*, pages 141–166. Springer, Geneva,Swizerland, 2006.

[88] D. Autret, A. Bitar, L. Ferrer, A. Lisbona, and M. Bardies. Monte Carlo Modeling of Gamma Cameras for I-131 Imaging in Targeted Radiotherapy. *Cancer Biotherapy and Radiopharmaceuticals*, 20:77–84, 2005.

[89] D. R. Neumann. Simultaneous Dual-Isotope SPECT Imaging for the Detection and Characterization of Parathyroid Patholog. *J Nucl Med*, 33:131–134, 1992.

[90] D. Sandrock, M. J. Merino, J. A. Norton, and R. D. Neumann. Parathyroid Imaging by Tc-Tl Scintigraphy. *J Nucl Med*, 16:607–613, 1990.

[91] G. G. Winzelberg and J. D. Hydovitz. Radionuclide Imaging of Parathyroid Tumors: Historical Perspectives and Newer Techniques. *Seminar in Nuclear Medicine*, 15:161–169, 1985.

[92] J. Schofer, R. P. Spielmann, T. Brmel, W. Bleifeld, and D. G. Mathey. Thallium-201/technetium-99m pyrophosphate overlap in patients with acute myocardial infarction after thrombolysis: prediction of depressed wall motion despite thallium uptake. *Am Heart J*, 112(2):291–295, 1986.

[93] X. Song, E. C. Frey, W. T. Wang, Y. Du, and B. M. W. Tsui. Validation and Evaluation of Model-based Crosstalk Compensation Method in Simultaneous 99m-tc Stress and 201-tl rest Myocardial Perfusion SPECT. *IEEE Trans Nucl Sci*, 51:72–79, 2004.

[94] E. Frey, B. M. W. Tsui, and J. Perry. Simultaneous Acquisition of Emission and Transmission Data for Improved Thallium-201 Cardiac SPECT Imaging using a Technetium-99m Transmission Source. *J Nucl Med*, 33:2238–2245, 1992.

[95] J. Li, B. Tsui, A. Welch, E. Frey, and G. Gullberg. Energy Window Optimization in Simultaneous Technetium-99m TCT and Thallium-201 SPECT Data Acquisition. *IEEE Trans Nucl Sci*, 42:1207–1213, 1995.

[96] K. Knesaureck and J. Machac. Three-Window Transformation Cross-Talk Correction for Simultaneous Dual-Isotope Imaging. *J Nucl Med*, 38:1992–1998, 1997.

[97] G. J. Hademenos, H. Weinstein, B. McSherry, and J. A. Leppo. An Improved Method for Simultaneous Dual Isotope Tc-99m/Tl-201 Emission Scintigraphy. *IEEE Nuclear Science Symposium and Medical Imaging Conference*, 25:1083–1085, 1992.

[98] H. W. A. M. de Jong, W. T. Wang, E. C. Frey, M. A. Viergever, and F. J. Beekman. Efficient Simulation of SPECT Downscatter Including Photon Interactions with Crystal and Lead. *Med. Phys.*, 29:550–560, 2002.

[99] S. C. Moore, J. Ouyang, M. A. Park, and G. E. Fakhri. Monte Carlo-based Compensation for Patient Scatter, Detector Scatter, and Crosstalk Contamination in In-111 SPECT Imaging. *Nucl. Inst. and Meth.in Phys. Res. A.*, 569:472–476, 2006.

[100] J. Ouyang, G. E. Fakhri, and S. C. Moore. Fast Monte Carlo based Joint Iterative Reconstruction for Simultaneous Tc-99m and I-123 SPECT Imaging. *Med. Phys.*, 34:3263–3272, 2007.

[101] S. C. Moore, R. J. English, C. Syravanh, D. E. Tow, R. E. Zimmerman, K. H. Chan, and M. F. Kijewski. Simultaneous Tc-99m/Tl-201 Imaging using

Energy-based Estimation of the Spatial Distributions of Contaminant photons. *Nuclear Science Symposium and Medical Imaging Conference*, 4:1507–1511, 1994.

[102] D. J. De Vries, S. C. Moore, R. E. Zimmerman, S. P. Mueller, B. Friedland, and R. C. Lanza. Development and validation of a monte carlo simulation of photon transport in an anger camera. 9(4):430–438, 1990.

[103] S. C. Moore, K. Kouris, and I. Cullum. Collimator design for single photon emission tomography. *Eur J Nucl Med*, 19(2):138–150, 1992.

[104] H. Newiger and K. Jordan. Optimization of collimators for imaging positron emitters by a gamma camera. *Eur J Nucl Med*, 11(6-7):230–234, 1985.

[105] R. L. Mather. Gamma-Ray Collimator Penetration and Scattering Effects. *Jour. Appl. Phys.*, 28:1200–1207, 1957.

[106] M. J. Jahns. The influence of penetrating radiation on collimator performance. *Phys Med Biol*, 26(1):113–124, 1981.

[107] C. M. Kao, P. L. Riviere, and X. Pan. Basics of Imaging Theory and Statistics. In M. N. Wernick and J. N. Aarsvold, editors, *Nuclear Cardiology*, pages 103–126. Elsevier, Nashville, Tennesee, 2004.

[108] A. Aungurarat, T. Ngamprayad, S. Phumkem, and T. Tuntawiwattananont. Stability study and optimization conditions of tc-99m-l,l-ethylenedicysteine. *Thai Nuclear Medicine Newsletter*, 6:35–42, 2001.

[109] T. Farncombe, S. Blinder, A. Celler, D. Noll, J. Maeght, and R. Harrop. A dynamic expectation maximization algorithm for single camera rotation dynamic SPECT (dSPECT). *IEEE Nuclear Science Symposium Conference Record*, 2:15/31–15/35, 2000.